



Mathematisch-Naturwissenschaftliche Fakultät  
Ernst-Moritz-Arndt-Universität Greifswald

Diplomarbeit

# Surface Effects in Complex Plasmas

Lars Lewerentz  
Greifswald, den 19.08.2010

Gutachter:  
Prof. Dr. Ralf Schneider  
Prof. Dr. André Melzer



# Zusammenfassung

Diese Arbeit simuliert Staubteilchen in Plasmen, um die Teilchenaufladung und Strukturbildung zu analysieren. Von besonderem Interesse ist die mikroskopische Wechselwirkung des Staubs mit den Plasmateilchen. Zur Untersuchung von Staubstrukturen sphärischer und nicht-sphärischer Teilchen wurde eine Teilchen-Teilchen-Simulation entwickelt, welche mit sphärischen Teilchen, die Coulombkugeln formen, validiert werden konnte. Von den in der Simulation erreichten Gleichgewichtszuständen wurden die Teilchen zufällig ausgelenkt, um die potentielle Energieoberfläche zu bestimmen und danach solche mit minimaler Energie erneut mit der Teilchen-Simulation gestartet. Hierbei weisen die Simulationen nicht-sphärischer Teilchen, in Form von Hanteln, mehrere Minima in der potentiellen Energie auf, allerdings immer noch mit wesentlich einfacherer Struktur als in biologischen Systemen. Sphärische Teilchen zeigen nur ein einziges Minimum. Im Gegensatz zu den rein abstoßenden Kräften in dieser Arbeit weisen biologische Systeme meist auch anziehende Kräfte auf, wodurch sogar helikale Strukturen möglich sind, die hier aber nicht beobachtet wurden.

Als nächstes wurde die Aufladung der Staubteilchen in kapazitiv gekoppelten Radiofrequenzentladungen (CCRF) untersucht. Zur realistischen, selbst-konsistenten Beschreibung des Staubs mit dem Plasma wurde die Particle-in-Cell (PIC) Methode um eine Teilchen-Teilchen-Methode erweitert (Particle-Particle-Particle-Mesh-Modell ( $P^3M$ )), welche die exakte Berechnung der Nahfeldwechselwirkungen zwischen Staub und Plasma erlaubt, so dass die Aufladung eines nicht-emittierenden Staubkorns überprüft werden konnte. Die resultierende Ladungsmenge ist geringer als die Vorhersagen der Orbital Motion Limit (OML) Theorie, wobei zeitliche Fluktuationen und Aufladungszeit innerhalb der theoretischen Erwartungen liegen. Ein Modell zur Beschreibung der Sekundärelektronenemission wurde im  $P^3M$ -Modell implementiert. Es zeigte sich, dass mit zunehmender Emission der Teilchenfluss zum Staub sinkt, folglich verringert sich die mittlere Ladung.

Weiterhin konnte die volle Dynamik der Radiofrequenz (RF) einer CCRF-Entladung sowie die Aufladung des Staubs phasenaufgelöst beobachtet werden. Ionen sind aufgrund ihrer Masse zu träge, um den RF-modulierten elektrischen Feldern zu folgen, im Gegensatz zu den Elektronen. Die meiste Zeit eines RF-Zyklus werden sie von den elektrischen Feldern abgestoßen. Nur während eines kurzen Zeitintervalls der RF-Periode, wenn die Potentialbarriere gering ist, fluten sie die Plasmaschicht und gleichen die Ladungsflüsse zu den Wänden aus. Diese Modulation der Elektronenflüsse während des RF-Zyklus hat aber wenig Einfluss auf die Staubladung, welche konstant bleibt. Fluktuationen, aufgrund der diskreten Natur der Ladung, sind weitaus dominanter.

Die experimentelle Methode der phasenaufgelösten optischen Emissionsspektroskopie (PROES) wurde in der Simulation durch Einführung einer Diagnostikroutine zur Berechnung der phasenaufgelösten Linienanregung von Argon nachgebildet. Die räumlich-zeitliche Dynamik des Experiments konnte dabei reproduziert werden. Die auftretenden zeitlich-räumlichen Emissionstrukturen werden durch Elektronen, die in der expandierenden Plasmaschicht beschleunigen, verursacht. Experimente zeigten eine erhöhte Anregungsrate, wenn sich ein kleines Staubkorn im Plasma befand. Dieser Effekt höherer Ordnung konnte mit dem  $P^3M$ -Code bestätigt werden. Der räumliche und zeitliche Verlauf der Linienanregung mit und ohne Staub zeigt Unterschiede. Die Simulation deutet darauf hin, dass diese Unterschiede von hochenergetischen Elektronen stammen, welche vom Grundzustand statt von metastabilen Zwischenzuständen anregen. Eine mögliche Erklärung dieses Verhaltens liefert die sich ausbildende Potentialsenke in der Umgebung des Staubs. Das Staubpotential hält Elektronen zurück, während die Plasmaschicht sich ausdehnt. Elektronen werden dadurch bei höheren Spannungen beschleunigt, so dass sie höhere kinetische Energien erlangen. Ausgehend von metastabilen Zuständen scheint diese Variation in der Anregungsrate durch den Staub selbst unterdrückt zu werden.

Insgesamt zeigen die Resultate des  $P^3M$ -Code eine gute Übereinstimmung mit den experimentellen Daten. Die Simulation erlaubt ein besseres Verständnis der zugrundeliegenden physikalischen Vorgänge, die für Messmethoden unzugänglich sind.

# Contents

<b>1</b>	<b>Motivation</b>	<b>1</b>
<b>2</b>	<b>Structure formation of non-spherical dust particles</b>	<b>3</b>
2.1	Introduction to complex plasmas . . . . .	3
2.1.1	Plasma sheath formation . . . . .	4
2.1.2	Crystal formation . . . . .	6
2.2	Particle-particle model (PP) . . . . .	7
2.2.1	Simulation of spherical particles . . . . .	9
2.2.2	Simulation of non-spherical particles . . . . .	14
2.3	Synopsis . . . . .	20
<b>3</b>	<b>Charging of dust in rf plasmas</b>	<b>21</b>
3.1	Basic properties of CCRF plasmas . . . . .	21
3.1.1	Capacitively coupled radio frequency discharges (CCRF) . . . . .	23
3.1.2	PIC-MCC Modelling . . . . .	25
3.1.2.1	Super-particle approach . . . . .	25
3.1.2.2	PIC cycle . . . . .	25
3.1.2.3	Poisson solver . . . . .	28
3.1.2.4	Monte Carlo Collision (MCC) model . . . . .	29
3.1.3	Characteristics of the argon background plasma . . . . .	30
3.2	Charging processes and surface effects of dust in CCRF plasmas . . . . .	37
3.2.1	Orbital Motion Limit (OML) . . . . .	38
3.2.2	P <sup>3</sup> M MCC model . . . . .	41
3.2.3	Charging of dust particles . . . . .	42
3.2.4	Emission effects on the charging . . . . .	45
3.2.4.1	Secondary electron emission . . . . .	45
3.2.4.2	Photoemission . . . . .	46
3.2.4.3	Thermionic emission . . . . .	46
3.2.5	Simulation of secondary electron emission . . . . .	47
3.3	Synopsis . . . . .	50
<b>4</b>	<b>Phase-resolved analysis of dusty CCRF plasmas</b>	<b>51</b>
4.1	Phase-resolved characteristics of the CCRF plasma . . . . .	51

4.1.1	PROES . . . . .	57
4.1.2	Excitation rates . . . . .	58
4.1.3	Simulation of excitation in argon . . . . .	59
4.1.4	Comparison of measured and calculated excitation rates . . . . .	61
4.2	Time-resolved effects of dust particles in CCRF plasmas . . . . .	64
4.2.1	Fluctuations of the charge during the rf cycle . . . . .	65
4.2.2	Influence of the dust on the CCRF plasma . . . . .	66
4.3	Synopsis . . . . .	77
<b>5</b>	<b>Conclusions</b>	<b>79</b>
<b>A</b>	<b>Appendix</b>	<b>81</b>
A.1	Dimensionless variables . . . . .	81
A.2	Table of modelled collisions . . . . .	83

“...if we were to name the most powerful assumption of all, which leads one on and on in an attempt to understand life it is that all things are made of atoms, and that everything that living things do can be understood in terms of jiggings and wiggings of atoms.”

*Richard P. Feynman*



# 1 Motivation

Complex plasmas have become very important over the last years. It started with the study of "Dusty Plasmas in the Solar System" [1], when interest arose about dust particles in plasmas. Nebulae, planetary rings, the magnetosphere of planets and comet tails are just some natural occurrences of complex plasmas [2]. They also appear in laboratory plasmas for material processing [3–5].

Considerable interest emerged about dust in future magnetic confined fusion devices [6–9]. Dust produced by erosion of plasma facing components, such as the wall and divertor materials can diminish the discharge performance or even lead to discharge disruptions [10]. A decent understanding of the elementary dust interaction processes is important, not only to govern fusion experiments, but for all series of actions where plasma plays a major role.

Dust particles acquire a charge depending on the local plasma environment. This charge results from the balance of a variety of currents at the surface of dust such as absorption of electron and ion fluxes, secondary electron-, photo- and thermoionic emission. Especially, in astrophysical surroundings emission might become significant.

In order to understand these processes in detail this thesis deals with the simulation of dust particles in complex plasmas. Of particular interest will be the microscopic understanding of the interaction at the surface of dust with plasma particles, because this interplay leads to the charging of the particles on which dust transport processes rely.

A micrometre-sized particle in laboratory plasmas typically accumulates a net negative charge of the order of  $10^4$  elementary charges. In the sheath of plasmas electric fields exist, strong enough to equilibrate the gravitational forces exerting on the massive dust grains. Therefore, dust particles can levitate and interact with each other in the sheath of plasmas on earth.

Although dust particles are usually highly charged the ratio of charge to mass is smaller than for ions, yielding minor accelerations and much larger dynamical timescales. Therefore, particles can form strongly coupled states and solid-like structures, called Coulomb crystals. Structure formation might have an important influence on transport processes in plasmas.

Up to now, most of the research on the structure formation of dust particles in plasmas is based on spherical particles [11–15]. In the second chapter a particle-

particle simulation is presented to examine the influence of the particle shape on structure formation and on the potential energy of the ensemble. The method is validated with spherical particles. Subsequently, the method is adapted to non-spherical particles, in this case an ensemble of barbells. Using a Monte Carlo sampling the potential energy surfaces of systems of spherical and non-spherical particles are scanned and their results compared with each other.

In the third chapter we will elucidate the microscopic properties of the capacitively coupled radio frequency (CCRF) discharge and its interplay with the surface of the dust particle. The principle of Particle-in-Cell simulations and extensions, used for the description of dust in plasmas, will be discussed. The results of a self-consistent model of a CCRF discharge are presented. These models allow to microscopically resolve the charging of dust grains including their interaction with plasma particles and modification of the background CCRF plasma. Possible effects of emission at the dust surface on particle charging are considered. The influence of secondary electron emission is of particular interest and will be studied in detail.

The fourth chapter extends the microscopic analysis to dynamic effects and dust particle charging resolving full radio frequency (rf) dynamics. Firstly, the dynamics of the rf discharge are presented. From the velocity distribution the excitation of argon is calculated, which is compared with the results from the phase-resolved optical emission spectroscopy (PROES). Further, the effects of the rf on the charging fluxes towards the dust will be analysed. Next, the influence of the dust particle on the excitation is investigated. PROES measurements revealed an increase and a fine structure in the excitation, if a dust particle is immersed, compared to the plasma without dust. The simulation will provide further insight into the phenomena.

Finally, the results and findings of this work are summarized.

# 2 Structure formation of non-spherical dust particles in plasmas

Up to now, most of the research on the structure formation of dust particles in plasmas is based on spherical particles (see [11–15]). In this chapter the effects of non-spherical particles and their structure formation in rf plasmas will be studied. At first, a particle-particle simulation will be validated with spherical particles. Then, the method will be applied to barbell particles. Using Monte Carlo sampling the potential energy surfaces of such systems are characterized.

## 2.1 Introduction to complex plasmas

A complex plasma, also often referred as a dusty plasma, is a low temperature plasma, consisting of neutrals, ions, electrons and an additional micron-sized charged component, namely the dust particles.

These dust grains introduce new phenomena due to their large size, weight and charge. They are obedient to various forces, which are insignificant in "normal" plasma surroundings [2, 16, 17]. In low temperature laboratory plasmas the net charge of dust grains typically exhibits thousands to ten thousands of elementary charges  $e$ . However, the charge to mass ratio ( $\frac{Q}{M}$ ) is small compared with ions, limiting the mobility of the dust particles. For instance, singly charged argon ions have a ratio of  $e/u$ , where  $u$  is the atomic mass unit. For a micrometre-sized dust particle this ratio is about  $10^4 e/10^{12} u$ . The motion of the dust particles is further damped due to collisions of the dust with the residual gas atoms or molecules, leading to a neutral gas friction force. In experiments it is possible to observe the "jiggings and wiggings" of the particles with ordinary video techniques. Taking direct and Coulomb scattering of ions into account resulting in the so-called ion drag force, the dynamics of dust particles can be further modified [17]. Due to the high charge and inertia the Coulomb interaction of systems with many dust particles can lead to strongly coupled systems.

Most important, due to their large mass, the gravitation exerting on dust particles cannot be neglected in the plasma. In contrast to all other plasma species dust particles only exist in the sheath, where the gravitational force is compensated by the electrostatic force acting on the dust.

Sign and value of the dust charge are determined by a variety of different mechanisms. Ion and electron fluxes, secondary electron, photo- and thermionic emissions are the most important processes. In the absence of emission a dust grain adapts the charge according to the influx of electrons and ions.

### 2.1.1 Plasma sheath formation

Bounded plasmas develop a very specific characteristic transition zone from the plasma to the wall, the so-called sheath. Sheaths occur wherever plasma is in contact with a surface. The charging process of dust particles is a specific form of the sheath formation. In the most simple case of complete surface absorption and without additional surface emission, objects in a quasi-neutral plasma will acquire a negative net charge, because electrons have a much higher mobility than the heavier ions. Electrons immediately hit the surface of the object transferring their negative charge. As the object accumulates the negative charge, the electrostatic potential of the object drops with respect to surrounding plasma (see Fig. 3.1). As a consequence, electrons are repelled and ions are attracted until currents balance.

The unperturbed bulk plasma is quasi-neutral, i.e.

$$|n_e - n_i| \ll n_{e,i}, \quad (2.1.1)$$

where  $n_e$  and  $n_i$  are electron and ion density, respectively. The plasma bulk has no notable electric fields and a flat potential profile.

From the analysis of the plasma-wall interaction one can reason that a transition region must exist, known as the presheath, connecting plasma bulk and sheath. The derivation assumes cold ions. Their velocity towards the wall results from the acceleration within the sheath. Suppose the electrons have a Maxwellian distribution and the flow of the ions at the sheath edge is conserved. For the solution of the linearized Poisson equation to be monotonic, it is necessary for the ions to accelerate at sheath edge to sound velocity

$$c_s = \sqrt{\frac{k_B T_e}{m_i}}. \quad (2.1.2)$$

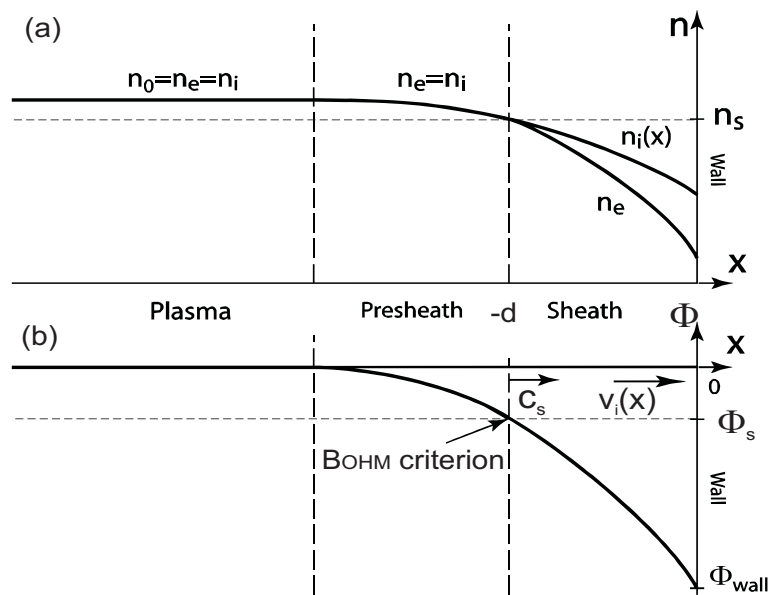


Figure 2.1: Schematic dependence of the densities (a) and the potential (b) in the plasma towards material walls

This so-called Bohm criterion [18] makes it possible for the potential and densities to match smoothly between plasma and sheath. Within the sheath, electrons are decelerated and repelled by the electric fields, whereas ions are further accelerated. Their kinetic energy can become higher than the binding energies of atoms in the surface. This process allows surface treatments like etching or thin film deposition.

The wall is usually assumed to be a sink for both electrons and ions. Electrons are captured at a conducting surface, whereas ions neutralize. However, their density profiles differ. Due to electrostatic repulsion only few electrons are able to overcome the sheath barrier, so that the electron density decreases (see Fig. 2.1). At the surface, electrons have a purely half-Maxwellian distribution with no electrons being reflected into the bulk. The density of the ions decreases as well, but this is due to continuity of the fluxes. Provided there are no sources in the sheath the ion density has to decrease, since the ions are accelerated to the wall. Generally, the drop in ion density is minor relative to the electrons. The sheath is the only plasma region where large-scale imbalances between electron density  $n_e$  and ion density  $n_i$  occur. The positive net charge  $n_i > n_e$  in front of the wall shields from the negative surface. Due to this, the plasma bulk obtains a positive plasma potential  $\Phi_p$  with respect to material walls. To achieve parity of the fluxes, at equilibrium the plasma shields itself from external sinks by the

potential drop. Since the drop in the potential towards the wall is considerable, electric fields exist in the sheath. Especially in rf discharges mean electric fields are large. They are strong enough to compensate the gravitational forces exerting on the dust grains allowing them to levitate force-free.

### 2.1.2 Crystal formation

When the ratio  $\Gamma$  between the Coulomb energy and the kinetic energy

$$\Gamma = \frac{Q^2}{4\pi\epsilon_0 b \cdot k_B T} \exp\left(-\frac{b}{\lambda_D}\right) \quad (2.1.3)$$

of a charged particle system in a plasma exceeds a critical value,  $\Gamma \gtrsim 170$ , particles self-arrange into configurations known as Coulomb or plasma crystals [19, 20]. This discovery led to an enormous interest in the investigation of strongly coupled dusty plasmas [2]. The inter-particle distance is approximated by the Wigner-Seitz radius  $b = (3/4\pi n)^{1/3}$ . Here  $Q$ ,  $T$  and  $n$  are the charge, temperature and density of the investigated particles.

The state of the Coulomb system is known to be weakly coupled if the coupling parameter  $\Gamma < 1$  is small. Because of their huge charge dust in plasmas is usually strongly coupled. If  $\Gamma$  exceeds certain critical values the composition of grains traverses a phase transition from a gaseous state into a fluid phase or into crystalline structures [11–13].

Experiments confirmed that dust particles trapped in the sheath of a plasma form crystal-like structures [21–25]. In low temperature laboratory plasmas the low dust temperature and the high particle charge result in coupling parameters of the order of a few thousand.

In [14, 15] the authors obtain in the experiment spherical three-dimensional plasma structures consisting of dust particles, so-called Coulomb balls. A variety of forces is used to confine the three-dimensional structure.

As a starting point this chapter will only consider the plasma background to guarantee the compensation of the gravitational force by the large electric field force on the dust in the sheath, resulting in a force-free levitation of the dust. In order to examine the formation and the structure of Coulomb balls the arrangement of such many-particle systems is then merely determined by their electrostatic interaction, namely by Coulomb forces. A harmonic potential  $\Phi_{ext}$  is superimposed to confine the particles similar to laboratory experiments for Coulomb balls.

Up to now nearly all experiments and theoretical investigations are based on a

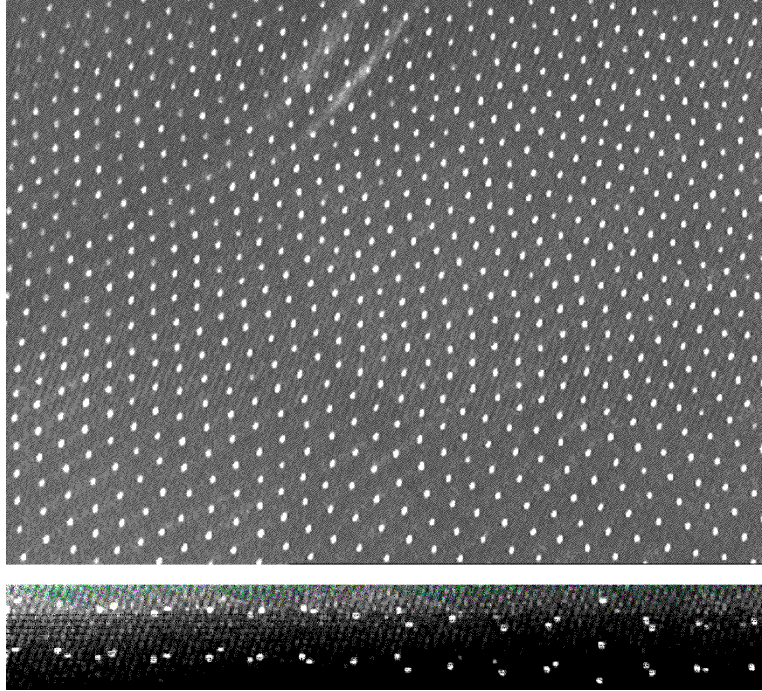


Figure 2.2: Top and side view of a plasma crystal. The upper picture reveals a hexagonal lattice structure of dust particles in a rf discharge. Thereunder the side view shows the vertical layered structure. Picture taken from [13].

spherical particle shape [14–16, 19, 21, 24, 26]. However, complex plasmas consisting of anisotropic particles exhibit a variety of states [27]. In biochemistry for instance, the interaction of non-spherical molecules with higher electrostatic moments have always been of major interest. Calculations of colloidal suspensions demonstrate the existence of helical structures with a high dimensional energy surface [28]. Therefore, this chapter discusses the effect of non-spherical dust particles on structure formation in systems consisting of dust particles. After simulating spherical or point-like particles the simulation is applied to barbell-shaped particles to investigate the change in the self-arrangement of non-spherical particles. The differences in the potential energy surface and in the particle arrangements will be discussed.

## 2.2 Particle-particle model (PP)

The obvious approach to calculate the dynamics of a system of  $N_p$  particles is to consider all interactions of single particles with every other particle (particle-

particle (PP) or molecular dynamics (MD) model). Subsequently, the force calculation time scales with  $\mathcal{O}(N_p^2)$ . This poses severe limits for the numerical application of such models and restricts the number of particles in a MD simulation.

In the following a system of particles interacting via electrostatic forces confined in a three-dimensional harmonic potential is studied. The simulation is applied to both spherical and non-spherical particles.

Spherical particles are to some extent a special case of barbell-shaped particles. It is assumed that two spherical particles correspond to one barbell with broken binding. The total number of charges is therefore the same, but the number of particles is doubled. The finite size of particles is neglected.

For the barbell simulation two point charges belonging to the same particle have a fixed distance  $a = 2h$ . Each barbell consists of two point-like charges of same sign and value. As initial condition for the MD simulation particles with random velocity are randomly distributed over the domain. In each time step the forces are calculated according to the Coulomb interaction between the particles and the external potential. These forces determine the motion of the centre of mass of the  $k^{\text{th}}$  barbell at position  $x_k$ , due to the force  $F_k$  and a rotation of each barbell around its centre.

A single charge  $\kappa_1$  interacts with all surrounding charges via electrostatic forces except the charge  $\kappa_2$  belonging to its own barbell  $k$ , which leads to

$$\underline{F}_{\kappa_1} = \frac{q^2}{4\pi\epsilon_0} \sum_{l \neq k} \left( \frac{r_{\lambda_1}}{|r_{\lambda_1}|^3} + \frac{r_{\lambda_2}}{|r_{\lambda_2}|^3} \right), \quad (2.2.1)$$

where  $\lambda_{1/2}$  denote the charges of the  $l^{\text{th}}$  barbell. The velocity and coordinates of the centre of mass change per time step according to Eulerian approximation  $\Delta \underline{v}_k = \underline{F}_k/m \cdot \Delta t = (\underline{F}_{\kappa_1} + \underline{F}_{\kappa_2} + \underline{F}_{ext})/m \cdot \Delta t$  and  $\Delta \underline{x}_k = \underline{v}_k \cdot dt$ , respectively. The torque on that barbell leads to an angular acceleration

$$\Delta \underline{\omega} = \underline{I}^{-1} \cdot \underline{L}_k = \underline{I}^{-1} \cdot (\underline{h}_{\kappa_1} \times \underline{F}_{\kappa_1} + \underline{h}_{\kappa_2} \times \underline{F}_{\kappa_2}) \Delta t \quad (2.2.2)$$

and therefore to a change in angular velocity. The inertia tensor  $I$  takes into account the shape of the particle and its mass distribution.

In order to achieve an equilibrium state, an artificial viscosity term is introduced to slow down particle motions until the kinetic energy approaches zero. After the transient phase of "simulated annealing", particles arrange into an equilibrium position. Subsequently, a Monte Carlo (MC) technique is used in order to

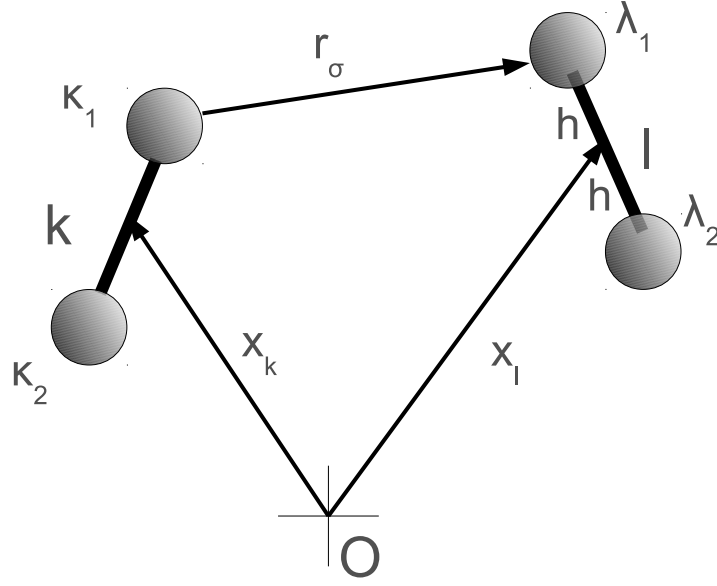


Figure 2.3: Coordinates used in the calculation for the description of the particle movement.  $r_\sigma$  reflects all possible interactions of the simulation between two particles ( $\sigma = \{(\kappa_1, \lambda_1), (\kappa_1, \lambda_2), (\kappa_2, \lambda_1), (\kappa_2, \lambda_2)\}$ ).

analyse the potential energy surface of the configuration close to the equilibrium established in the MD.

### 2.2.1 Simulation of spherical particles

As a first step, structure formation of spherical particles is studied to validate the simulation with a well-known system and to use this as reference for the studies of non-spherical particles. The simulations were carried out for different charges, external confinement potentials and various number of particles. The results of the MD simulation are in very good agreement with previous MD calculations and experiments [14, 15, 26]. In particular, results of a simulation with 100 charges are discussed in detail. After the MD relaxation the arrangement of spherical dust particles in Fig. 2.4 is structured. Details are shown in Fig. 2.5. Particles self-assemble into shell structures. In a solid state lattice the distances between the particles are fixed. Here, the structural order is analysed by the pair correlation function showing several peaks corresponding to nearest, second-nearest neighbours and so forth (c.f. Fig. 2.6). The pair correlation function

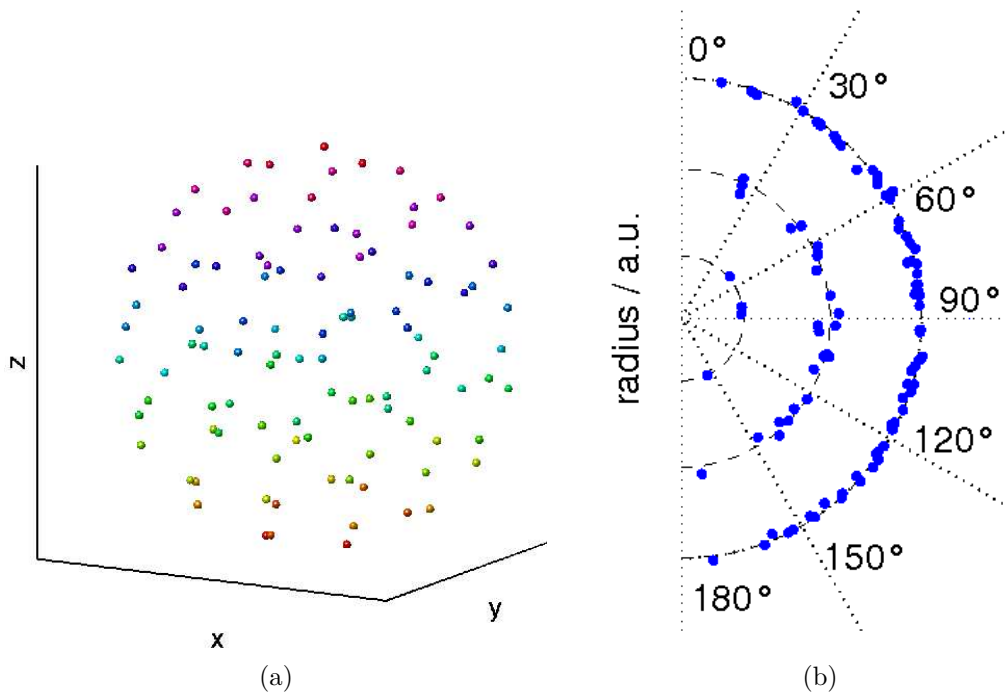


Figure 2.4: Equilibrium state of a MD simulation of 100 spherical particles. Particles arrange into structures called Coulomb balls (see (a)). In (b) the particles' radial projection is presented. The arrangement into shells is explicitly shown.

resembles the distribution of inter-particle distances. Due to the electric repulsion of the particles, a minimal distance exists between particles.

After the MD simulation equilibrated, the energy potential surface close to this configuration is scanned by a Monte Carlo (MC) dislocation of the particles' coordinates. Each particle is shifted by a random value in x-,y- and z-direction. These random numbers are uniformly distributed from -1 to 1. The strength of the variation is determined by a parametric amplification factor  $\Delta x$ , which is varied during the scan. New coordinates are then calculated by adding the product of amplification factor and random number to the old MD coordinates. For each such configuration the potential energy of the particles is calculated. The potential energy consists of the repulsion potential  $\Phi_r$  between the particles plus the superimposed external potential  $\Phi_{ext}$  according to the particles' position. This procedure is repeated for each  $\Delta x$  over a certain range. If the total energy of a MC configuration is smaller than the total energy of the MD simulation, a further MD calculation of this configuration is performed and the total

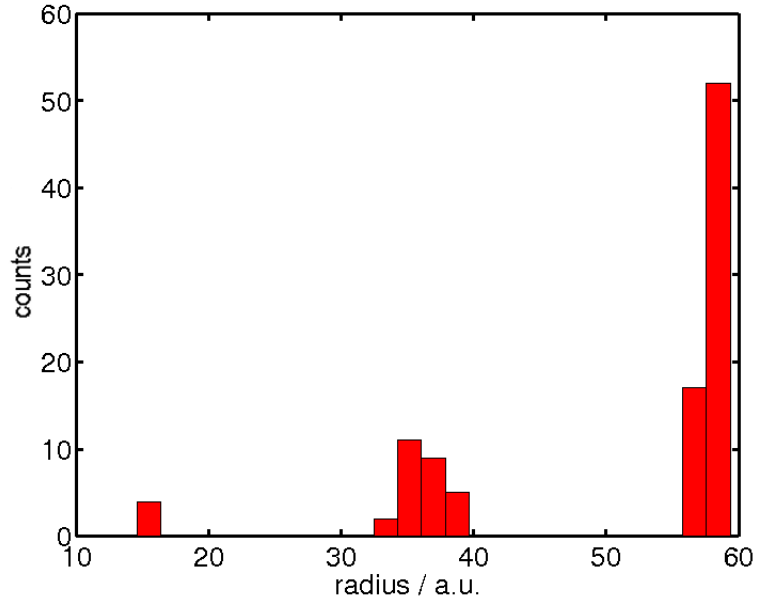


Figure 2.5: The distribution of radii for a cluster of 100 particles is restricted to certain values, i.e. particles assemble into three shells. The number of particles in the simulation from the inner to the outer shell is (4,27,69), which remarkably coincides with the result in [26], which yield (4,26,70).

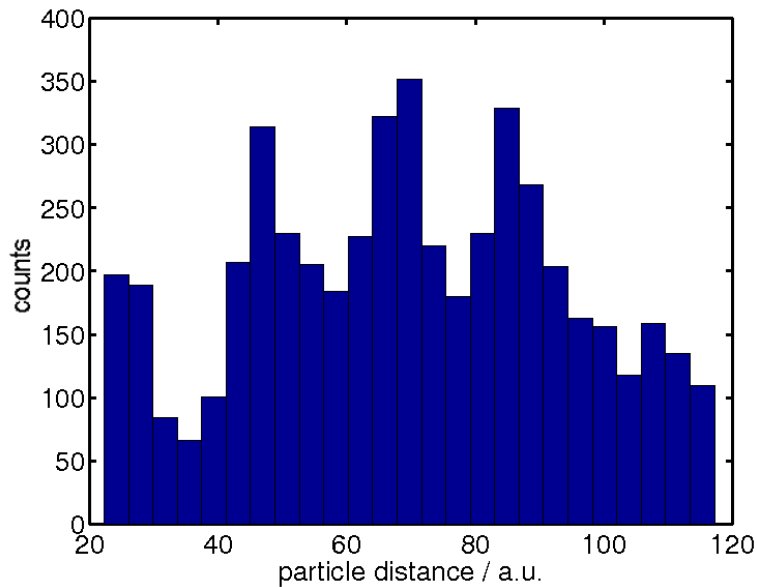


Figure 2.6: The pair correlation function of spherical particles shows several peaks indicating fixed distances of a particle to its neighbours.

energy is determined. The scan can be considered as consecutive heating and relaxation cycles to study the landscape of the potential energy surface near the MD configurations for spherical particles.

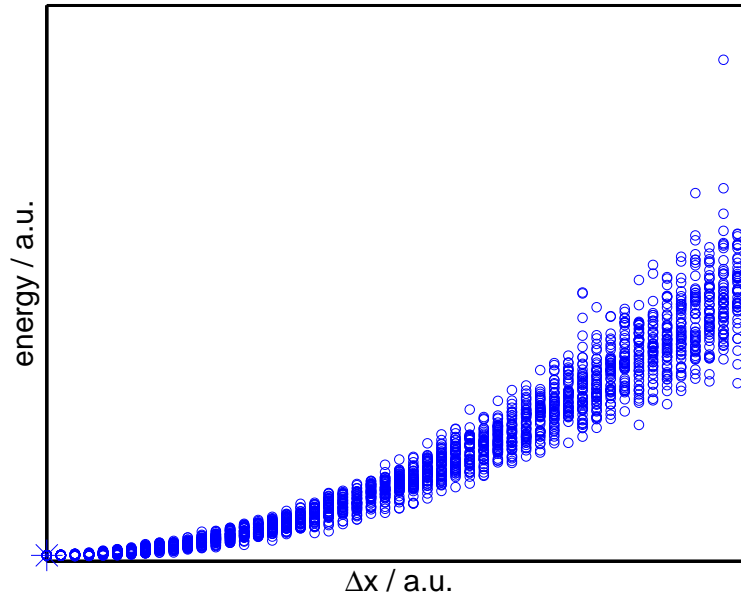


Figure 2.7: Result of the total energy of the MC scan.

The variance of the energy is typically proportional to the square root of the variation strength. The particle ensemble shows a parabolic growth of potential energy with variation strength like a single super-particle in a harmonic potential (see Fig. 2.7). A finer MC scan with smaller  $\Delta x$  of the potential energy surface and can be seen in figure 2.8.

Although the MC simulation found new minima besides the MD minimum, these configurations are not "true" minima. For each such configuration the subsequent MD run fell back to the configuration of the first MD calculation. Depending on the initial parameters the MD simulation seems to find a minimum of the potential energy surface.

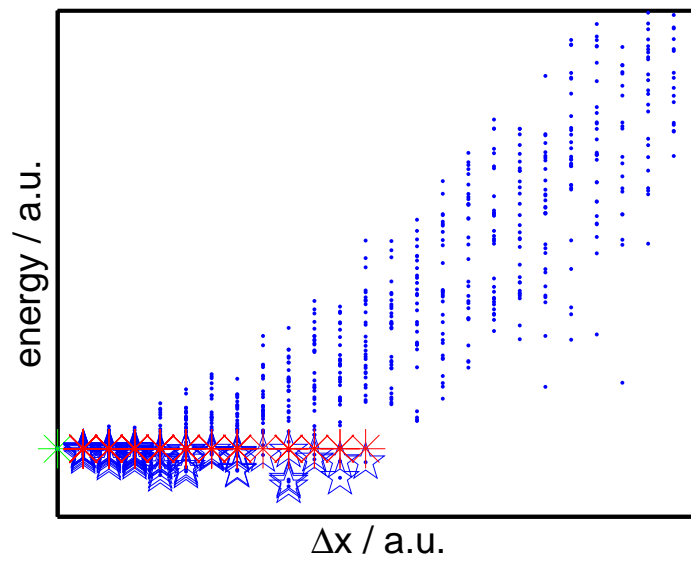


Figure 2.8: Each point indicates the total energy of a configuration. The results of the MD simulation are shown with crosses. At zero variation ( $\Delta x = 0$ ) a green cross shows the result of the initial MD simulation. All points in blue are the results of the MC scan. Indicated by stars are arrangements from the MC scan with lower total energy than the energy of MD run. Labelled with red crosses are the energies from the following MD calculations of these minimum configurations.

### 2.2.2 Simulation of non-spherical particles

In this section the structure formation of non-spherical dust particles will be discussed, using barbells instead of spherical particles (see Fig. 2.9). Such particles exhibit the necessary electric anisotropy and are easy to treat algorithmically. Therefore, this is a first approach to understand the influence of non-spherical dust particles on structure formation. The particle-particle model discussed before is used, only considering the interaction of barbells.

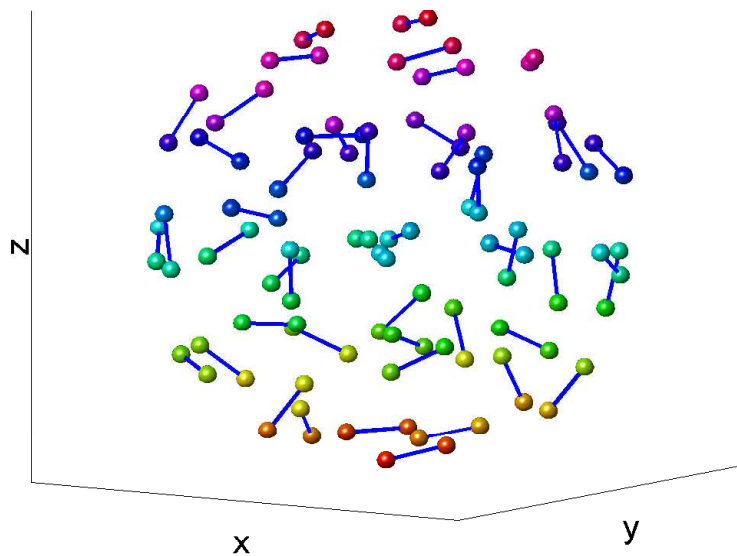


Figure 2.9: Final state of a MD simulation of 50 barbells.

The arrangement of barbells in the MD simulation is different to the one for spherical particles. Still, a shell structure is visible (see Fig. 2.10). Since the distance of the charges of a barbell is smaller than the mean inter-particle distance of spherical particles, the total occupied space by the barbells is less than for spherical particles, which can be seen in the pair correlation function (see Fig. 2.11).

The pair distribution function of every charge in the system (see Fig. 2.12) shows the same peak structure as the pair correlation of the barbells' centres of mass. Due to the aliasing effect of the short distance between the charges of a single barbell the pair correlation function for the charges is broadened.

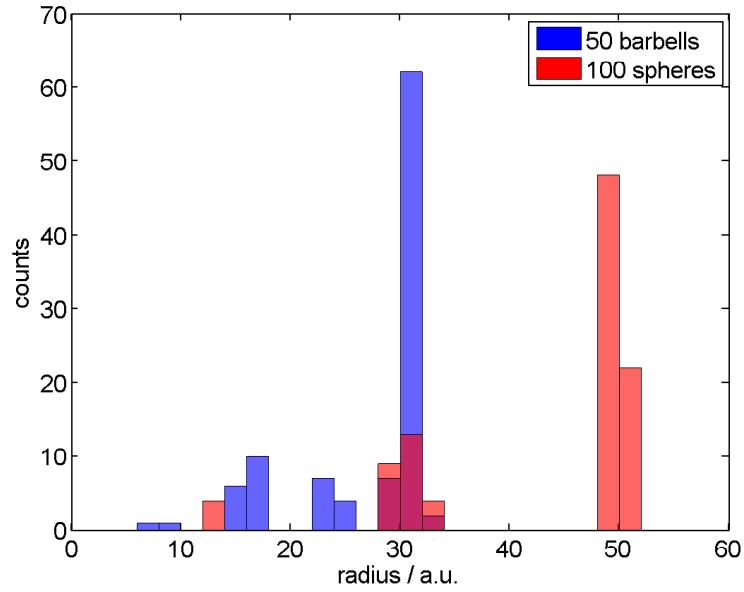


Figure 2.10: Comparison of the distribution of radii for 50 barbells and 100 spheres. The calculation was performed with the following parameters:  $q = 32$ ,  $a = 2h = 8$ .

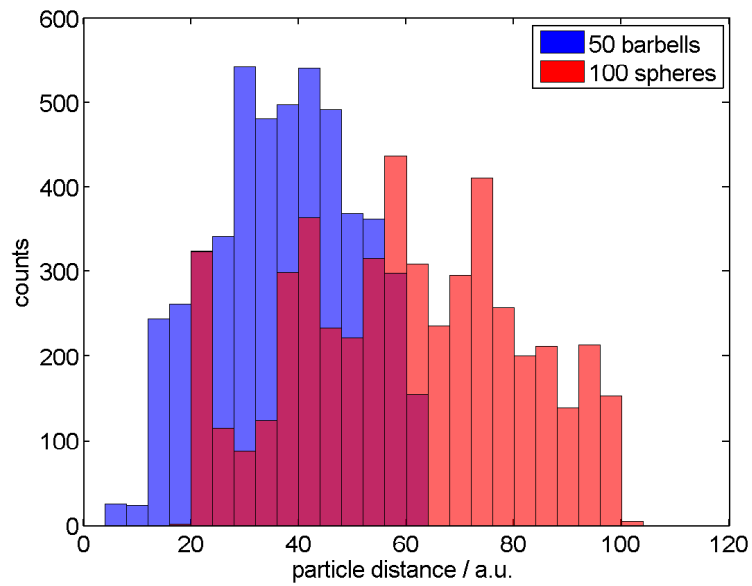


Figure 2.11: Comparison of the pair correlation function for 50 barbells and 100 spheres. The calculation was performed with the following parameters:  $q = 32$ ,  $a = 2h = 8$ . The pair correlation function of the barbells is smeared out due to the aliasing effect of the barbells.

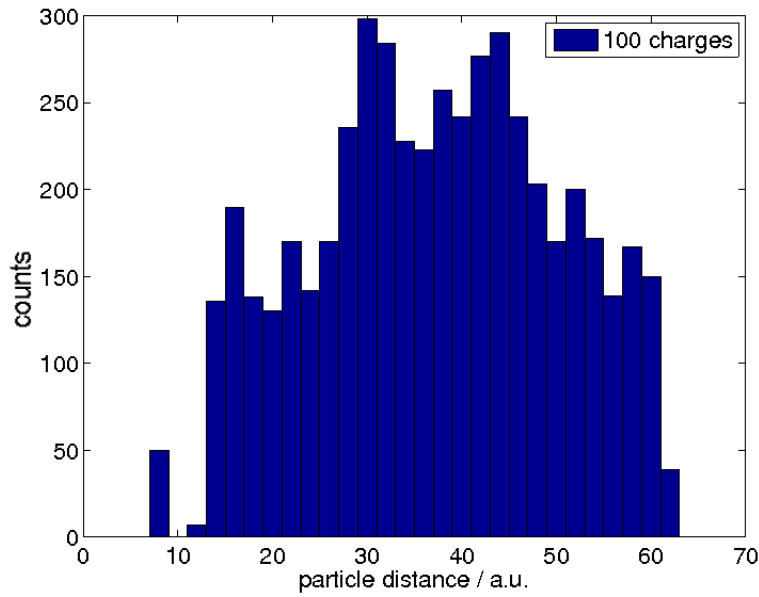


Figure 2.12: The pair correlation function of every charge in the system. The calculation was performed with the following parameters:  $q = 32$ ,  $a = 2h = 8$ . The peak for a particle distance of 8 exactly corresponds to the intra-particle distance of 50 barbells.

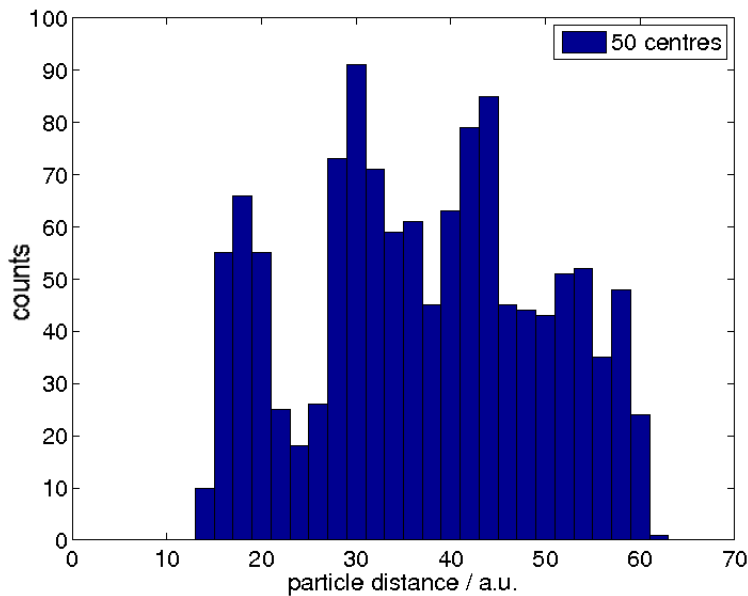


Figure 2.13: The pair correlation function of the barbells' centres of mass. The calculation was performed with the following parameters:  $q = 32$ ,  $a = 2h = 8$ .

Again, a Monte Carlo scan of the potential energy surface is performed. This time a uniformly distributed random rotation of the barbell around its centre of mass is applied in addition to a pure dislocation as in the case of spherical particles. The effect of the rotation can be seen as an initial broadening of the energy in the figures at zero variation ( $\Delta x = 0$ ). The barbells' ensemble also

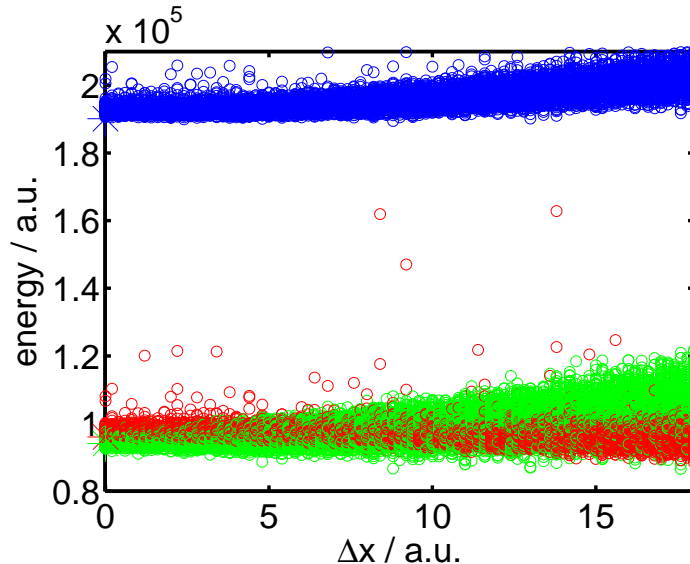


Figure 2.14: Result of the energy for a variation of the particle position. The repulsion energy and the external potential are indicated by red  $\circ$  and green  $\circ$  circles, respectively. The total energy is the sum of both and labelled with blue circles  $\circ$ . The result of the MD simulation is displayed by crosses at zero variation.

shows a quadratic growth of the external potential energy. This yields in a qualitative parabolic dependence of the total energy with the variation strength. The repulsion energy is scattered around an average (see Fig. 2.14).

Due to the anisotropic electric potential of each individual barbell the arrangement of particles is more complicated. After the Monte Carlo scan subsequent MD simulations of configurations with smaller total energy than the initial MD simulation tend to different arrangements (compare Fig. 2.15 with Fig. 2.16).

Thus, the potential energy surface is more complex. This is especially the case for large distances between the charges of a barbell. The different configurations have individual total energies (see Fig. 2.17). More than one minimum besides the initial MD minimum is observed. For the case considered here, two out of three MD simulations after the MC scan approach to the same initial MD configuration seen in figure 2.15. These whole arrangements only differ by a rotation, since

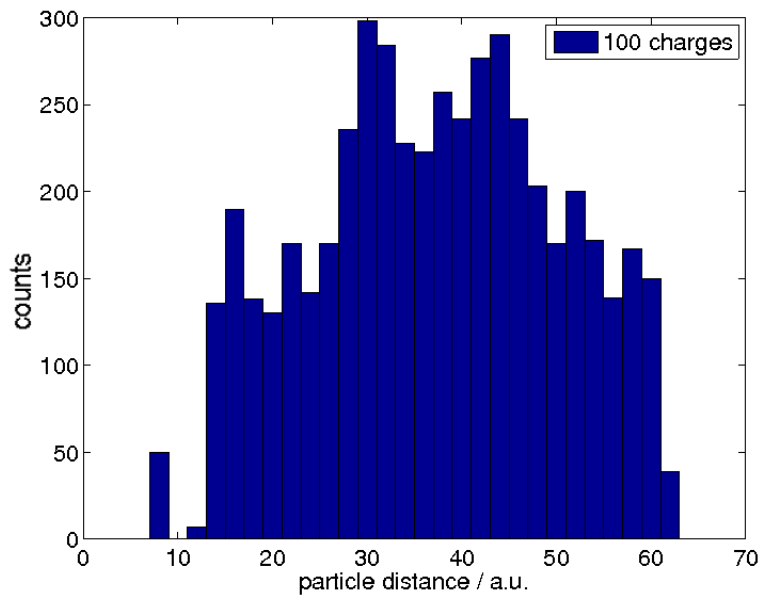


Figure 2.15: The pair correlation function of every charge in the system for the initial MD configuration.

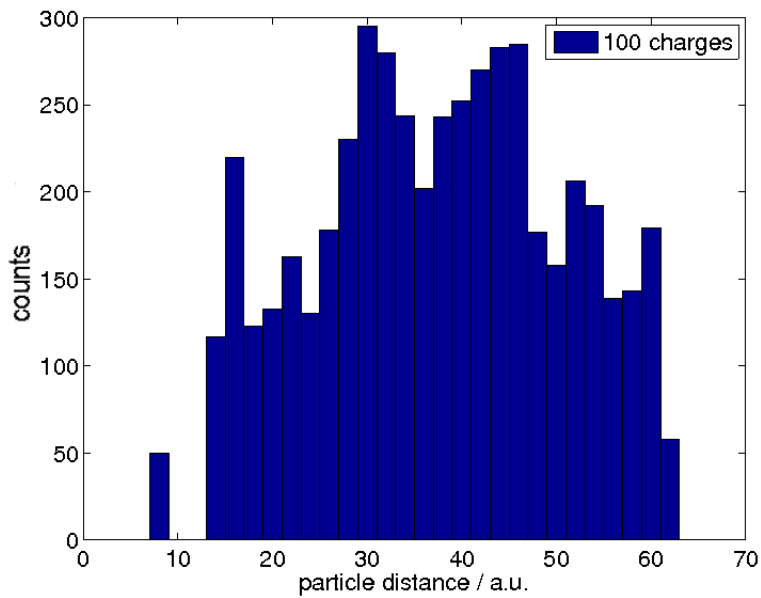


Figure 2.16: The pair correlation function of every charge in the system for the subsequent MD configuration with the higher total energy.

the pair correlation is rotational and translational invariant. However, the total energy is only rotational invariant. One system has an inclined total energy corresponding to the configuration shown in figure 2.16. Here, an additional minimum exists in contrast to the spherical case.

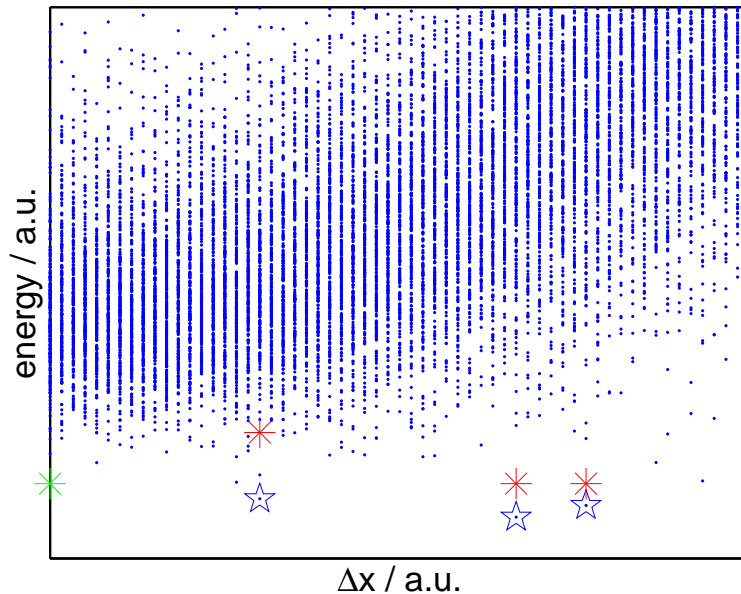


Figure 2.17: Each point indicates the total energy of a configuration. The results of the MD simulation are shown with crosses. At zero variation ( $\Delta x = 0$ ) a green cross shows the result of the initial MD simulation. All points in blue are the results of the MC scan. Indicated by stars are arrangements with lower total energy. From these minimum configurations the following MD calculations yield the energies labelled with red crosses. Notably, not all MD runs result in the same total energy.

Further minima in such energy spectra exist for a wide range of parameters ( $h, \Phi_{ext}$ ). This agrees with studies of non-spherical particles in colloidal suspensions.

Unlike the work of Fejer and Wales [28] has shown, it was not possible to observe helical strands in this system. However, in their work the force interacting between the particles is derived from a Lennard-Jones potential where in addition to repulsion attracting forces exist.

In order to confine the particles in a smaller volume, the external potential  $\Phi_{ext}$  has to be increased, which leads to a stronger influence of the external forces. This enhanced influence of external forces counteracts the anisotropic interaction of the barbells. Therefore, such systems show only small effects on structure formation of non-spherical particles compared to biological systems. In biological

systems the appearance of helical structures is attributed to the presence of additional attractive forces. For purely repulsive interaction no helical structures were observed.

## 2.3 Synopsis

In this chapter the structure formation of dust particles in a plasma was studied, including the influence of non-spherical particle shape. The effect of the plasma was only taken into account as a compensation of the gravitational force by electric forces in the sheath. This way dust particles levitate force-free. In order to study the formation of dust structures for spherical and non-spherical particles a particle-particle method was developed and validated with spherical particles forming Coulomb balls. Adding numerical viscosity equilibrium configurations have been obtained. To analyze the potential energy surface starting from these configurations random displacements of the particles were performed. From these random configurations the configurations with minimal energies were identified and restarted with the particle-particle model. With several stable configurations the potential energy surface is similar to the case of colloidal particles in suspensions forming helical arrangements. However, the potential energy has not shown such large numbers of minima in the potential energy surface. This is explained by the fact that in the systems studied in this work only repulsive forces between particles have been considered. However, biological systems are characterized by both attractive and repulsive forces allowing also helical structures, not observed for dust.

## 3 Charging of dust in rf plasmas

So far, we dealt with the formation of macroscopic dust structures. Now, the charging of particles will be resolved on a microscopic scale. At first, we will elucidate the microscopic properties of the capacitively coupled radio frequency (CCRF) discharge, which is the standard plasma environment for the investigation of dusty plasmas. For this purpose, the Particle-in-Cell (PIC) technique is introduced to model the rf plasma. Then, the role of dust particles in plasmas are considered. Several charging effects exist, which influence the charge and the potential of the dust. Here, the orbital motion limit (OML) theory of particle charging is presented. In order to simulate the close-range behaviour and the charging of dust particles an extension of the PIC, the particle-particle particle-mesh ( $P^3M$ ) model, is implemented. This model is a hybrid of a MD and PIC simulation, which enables to resolve the plasma particle motion in the vicinity of the dust necessary for the microscopic understanding of the charging. Finally, possible emission effects at the surface of dust particles are considered. In particular, the effect of secondary electron emission will be studied in detail.

This thesis extends the work of Matyash et al. [29–31] to study the dynamics of dust particles in rf plasmas taking into account close-range effects of a single dust grain.

### 3.1 Basic properties of CCRF plasmas

In electrostatics a single charge has a long-range Coulomb interaction potential

$$\Phi(r) = \frac{q}{4\pi\epsilon_0 r}, \quad (3.1.1)$$

which is inversely proportional to the distance  $r$ .

A plasma is generally charge-neutral, at least in the bulk. Otherwise charge separation would create strong electric fields. The fact, that only local charge

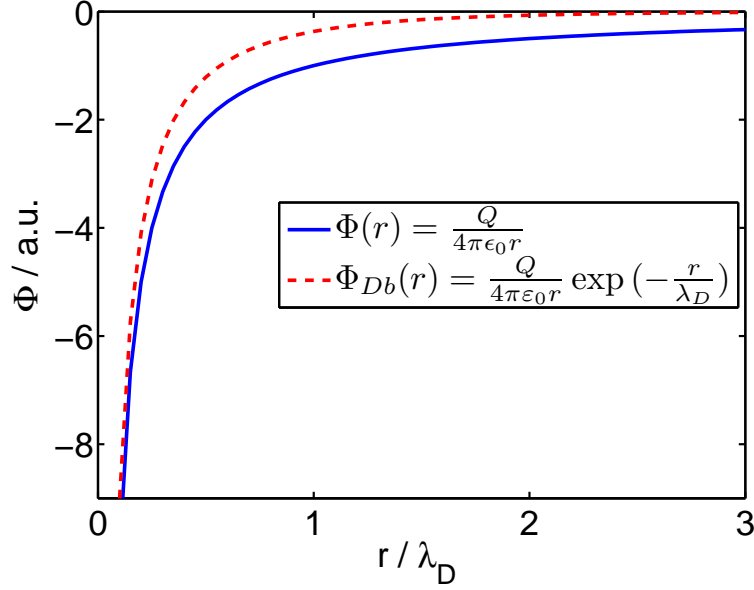


Figure 3.1: Comparison between Coulomb (blue full line) and Debye-Hückel potential (red dashed line).

variations can exist in plasmas, is called quasi-neutrality. A test charge immersed in a plasma is immediately surrounded by other charges of different polarity. Now, the potential of the probing charge is shielded by the polarized field of plasma particles leading to a diminished range of the electrostatic field of the probe. This process, also known as screening, results in a modified potential

$$\Phi_{Db}(r) = \frac{q}{4\pi\epsilon_0 r} e^{-\frac{r}{\lambda_D}}, \quad (3.1.2)$$

called Debye-Hückel or Yukawa potential. This was first described in the Debye-Hückel theory of electrolytes in 1923 [32].

The characteristic length scale in a collisionless plasma is the Debye length  $\lambda_D$ . This is the distance over which significant charge imbalances can exist. Generally, the shielding effect is caused by both electrons and ions

$$\frac{1}{\lambda_D^2} = \frac{1}{\lambda_{De}^2} + \frac{1}{\lambda_{Di}^2} \quad (3.1.3)$$

with

$$\lambda_{D\{e,i\}} = \sqrt{\frac{\epsilon_0 k_B T_{\{e,i\}}}{n_{\{e,i\}} e^2}}. \quad (3.1.4)$$

The smaller value determines the range. This can be either the electron Debye

length  $\lambda_{De}$  or the ion Debye length  $\lambda_{Di}$ . An exception for the existence of electric fields is the sheath, but its width is typically limited to a few electron Debye lengths. Any displacement of charged particles from equilibrium position in a homogeneous plasma gives rise to an electric field, resulting in a restoring force on the dislodged particles. In a first approximation this force is proportional to the separation of the charge. Plasma particles are sluggish so that the system behaves like a harmonic oscillator with frequency

$$\omega_{ps} = \sqrt{\frac{n_s q_s^2}{\epsilon_0 m_s}}, \quad (3.1.5)$$

the so called plasma frequency  $\omega_{ps}$  of species  $s$ , where  $s$  can denote any plasma particle. In the following electrons are denoted by the subscript  $e$  and ions by  $i$ . The electron thermal velocity

$$v_{th,e} = \lambda_{De} \cdot \omega_{pe} = \sqrt{\frac{k_B T_e}{m_e}}. \quad (3.1.6)$$

is given in terms of the electron plasma frequency and Debye length. The dynamical behaviour of plasma particles in the rf discharge, as we will see in section 4.1, will be restricted to its plasma frequency. Ions will react much slower than electrons due to their inertia.

### 3.1.1 Capacitively coupled radio frequency discharges (CCRF)

Capacitively coupled radio frequency (CCRF) discharges are common for the generation of low temperature plasmas, both in industry and research. They are widely used for surface treatments such as plasma etching in semiconductor manufacturing [33]. It was found, that micrometre-sized particles grow within reaction chambers from substrate materials [2, 5] influencing the manufacturing of microchips. Further, rf powered complex plasmas have been used for the deposition of thin films on surfaces [3, 4].

A typical CCRF discharge consists of two parallel electrodes in vacuum (see Fig. 3.2). One electrode is driven at high frequency voltage, usually at 13.56 MHz. The vacuum vessel is fueled with a working gas, which gets ionized by electrons. These get accelerated in the rf electric field producing a weakly-ionized plasma.

Although the experimental setup is relatively simple, the physical description of such rf plasmas is challenging due to the large range in dynamics and non-

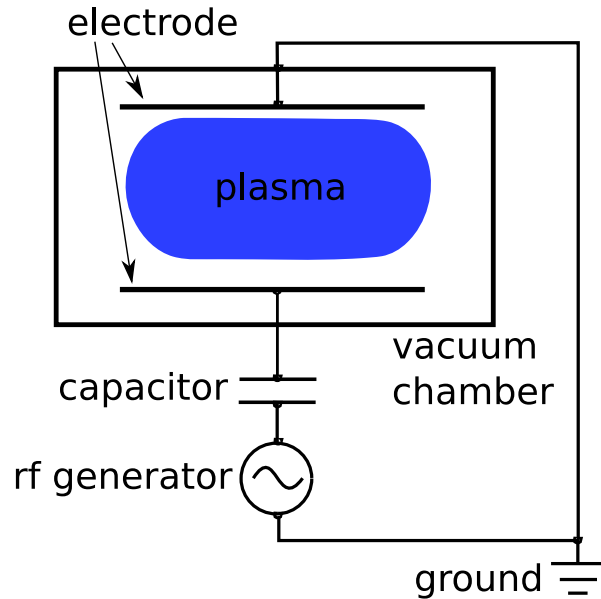


Figure 3.2: Scheme of a CCRF discharge with parallel plate electrodes.

Maxwellian characteristics of the distribution functions. Since a complete analytical understanding is still missing, a numerical treatment is necessary, but not less demanding.

In typical low temperature laboratory plasmas, parameters like plasma potential are spatially varying because of interactions with walls. The rf voltage adds supplementary temporal fluctuations. Mean free paths for Coulomb collisions in such plasmas usually are much larger than the size of the discharge, so that both electrons and ions are non-Maxwellian. Thus, a fluid description is not applicable for such systems.

In order to resolve the distribution function accurately a kinetic approach is needed. A molecular dynamics (MD) simulation with every interaction taken into account for such a large number of particles (up to  $10^{10}$ ) is too costly. The calculation time scales with the number of particles squared ( $\mathcal{O}(N_p^2)$ ). Although the shielding in plasmas is very effective (c.f. Debye-Hückel potential in Fig. 3.1), long-range interactions are considered. The Particle-in-Cell (PIC) method is able to resolve such systems kinetically in a feasible time. For the study of such plasmas this work uses a PIC code with Monte Carlo collision (MCC), developed by K. Matyash [29, 30]. The method and its applicability will be discussed in detail in the next section.

## 3.1.2 PIC-MCC Modelling

### 3.1.2.1 Super-particle approach

The number of particles in a plasma is extremely large and exceeds by far the maximum possible number of particles, which can be treated computationally. In the PIC scheme one gets a computational speed-up by the introduction of pseudo-particles. One simulated particle is equivalent to many physical particles, therefore it is called super-particle. The equations of motion for one particle

$$\underline{v}_i = \frac{d\underline{x}_i}{dt}, \quad m \frac{d\underline{v}_i}{dt} = \underline{F}(\underline{x}_i, \underline{v}_i), \quad (3.1.7)$$

is in general determined by the Lorentz force  $F_L \propto q$ . Since the charge to mass ratio  $\frac{q}{m}$  is fixed, a so-called super-particle with the same ratio, follows the same trajectory as an individual plasma particle. One can prove that the plasma model simulated by super-particles resembles the real plasma fully [34, 35]. Owing to statistical averaging to obtain smooth distribution functions or moments, a certain density of super-particles is needed.

### 3.1.2.2 PIC cycle

The algorithm of one PIC cycle (see Fig. 3.11) is determined by the interplay between super-particles and field quantities. Processes in such a model are computed self-consistently within the following way.

- i) Each particle  $i$  has a certain continuous representation of position  $x_i$  and velocity  $v_i$ . Subsequently, there is a weighting scheme that assigns these positions to densities  $n_{jkl}$ , field representations on a three-dimensional mesh. Here,  $i, j, k$  denote the x-,y- and z-direction of the mesh. The code to which this work refers is based on a Cloud-in-Cell (CIC) weighting scheme. Each point-like particle is smeared out over a width of a cell size  $\Delta x$ . The particle density is then linearly weighted to the nearest grid points. This procedure causes less noise than nearest-grid-point (NGP) weighting scheme [34, 36, 37]. Nevertheless, these "clouds" can move through each other, lacking the proper near-field electrostatic repulsion. Generally, the weighting reduces the resolution in the potential and force fields. Only field variations with wavelengths longer than the distance between mesh points are accurately represented.
- ii) In the next step the Poisson equation is solved on the mesh, yielding the electrostatic potential and consequently the electric field at the grid points.

- iii) Subsequently, forces are mapped back from the grid points to the particles with respect to their actual positions. This mapping should have the same weighing scheme in order to conserve the total momentum of the system.
- iv) Finally, the particles' positions and velocities are updated according to the equations of motion, applying these forces. This part is also known as the particle pusher or mover.

Afterwards, the cycle is repeated and the particles are moved self-consistently. Surfaces are usually a sink for charges in a plasma. Electrons are captured at the surface of conducting walls, whereas ions recombine. The code models two electrodes, one is grounded and the second is powered by a harmonic rf voltage. Particles exceeding the virtual material borders are removed from the calculation. The other directions have periodic boundary conditions, i.e. particles are reinjected on the other side of the simulation with proper position and velocity [34].

Numerical calculations are based on the discretization of analytical formulae. For simplicity we present the algorithm for the 1D Poisson equation

$$\nabla^2 \Phi = -\frac{\rho}{\varepsilon_0}, \quad (3.1.8)$$

which leads with the grid potential  $\Phi_i = \Phi(i \cdot \Delta x)$  and density  $\rho_i = \rho(i \cdot \Delta x)$  to the finite difference approximation

$$\frac{\Phi_{i+1} - 2\Phi_i + \Phi_{i-1}}{\Delta x^2} = -\frac{\rho_i}{\varepsilon_0}. \quad (3.1.9)$$

To analyse the stability of a finite difference scheme one can locally linearise the equations with the wave ansatz

$$f(x, t) = Ae^{i(kx - \omega t)} \quad (3.1.10)$$

and then look at the growth of linear modes. This is known as the von-Neumann-stability analysis. For a stable algorithm the amplitude  $A$  is required to be less than or equal to 1 ( $|A|^2 \leq 1$ ). For many schemes, including the leapfrog method, this results in the *Courant-Friedrichs-Levy* stability criterion [36, 37]

$$\frac{|v|\Delta t}{\Delta x} \leq 1. \quad (3.1.11)$$

This means that the velocity  $\frac{\Delta x}{\Delta t}$  at which information propagates within the numerical algorithm must be faster than the speed  $v$  of the solution [38]. Not only the amplitude is of importance, but numerical errors shift the phase in the linear wave ansatz. For many steps the phase errors accumulate leading to stronger restrictions for the time steps.

Electrons are the fastest, so that their time step is the smallest. Since ions are heavy, their motion takes place on a much larger time scale. The code considers that fact by means of different time steps.

In the simulation the Boris scheme is used for particle advancing in time [36, 39]. It is a special leap-frog scheme for magnetized plasmas, which is fast and stable. It is second-order accurate, requires only one field evaluation per time step, and has good energy conservation properties.

In order to be numerically stable, the PIC approach has some prerequisites to be fulfilled. These are stated here in summary:

- to resolve the plasma frequency the time step is restricted,  $\omega_p \Delta t \leq 0.2$ ,
- to unravel the smallest scale,  $\Delta x < \lambda_D$ ,
- for statistical properties, number of particles per cell  $\gtrsim 10$
- to resolve the gyro-motion in magnetized plasmas,  $\omega_c \Delta t < 0.35$ .

The gyrofrequency of circular motion in magnetic fields is denoted by  $\omega_c$ . The discretization of volume and time should be chosen as large as possible to reduce the workload for the needed accuracy, but the characteristic wavelength in plasmas, the Debye length  $\lambda_D$ , restricts this. For a suitable reproduction of fast oscillations the averaging length  $\Delta x$  should be less than the Debye length. Further, the number of super-particles should be sufficient to achieve small statistical fluctuations of the moments of distribution functions [34].

The code itself uses many numerical and computational performance tweaks. One of the most important improvements in speed results from the use of dimensionless variables. A detailed derivation of the dimensionless variables can be found in the appendix A.1.

One has to be careful, that the scheme does not introduce self-forces. Not only the accuracy and stability of each separate building block of the PIC cycle is essential, particularly, the interplay between the elements of the PIC cycle. Further details about weighting schemes, the particle pusher and their interplay see [34] or the monograph [37].

### 3.1.2.3 Poisson solver

The code of *Matyash et al.* [29, 31, 35, 40] used in this thesis solves the Poisson equation over the whole domain via the algebraic SuperLU solver. SuperLU is a general purpose library for the solution of large, sparse, (non-)symmetric matrices. The library routines perform a decomposition in lower and upper (LU) triangular matrices. The decomposition is computed with numerical pivoting, equilibration, iterative refinements and reordering due to sparsity and stability (see [41] for further details about the algorithm).

The one-dimensional difference scheme in equation (3.1.9) forms a linear algebraic system of the form  $\underline{\underline{A}} \cdot \underline{\Phi} = -\frac{\Delta x^2}{\varepsilon_0} \underline{\rho}$ , where the matrix  $\underline{\underline{A}}$  consists of the coefficients of the difference scheme and vector  $\underline{\Phi}$  and  $\underline{\rho}$  is the chain of the discrete  $\Phi$ 's and  $\rho$ 's, respectively. Matrix  $\underline{\underline{A}}$  is then given by the algebraic system

$$\begin{pmatrix} -2 & 1 & 0 & 0 & \cdots & 0 & 1 \\ 1 & -2 & 1 & 0 & \cdots & 0 & 0 \\ 0 & 1 & -2 & 1 & \cdots & & 0 \\ \vdots & & \ddots & \ddots & \ddots & & \\ 0 & & & & & & 1 \\ 1 & 0 & \cdots & & 0 & 1 & -2 \end{pmatrix} \cdot \begin{pmatrix} \Phi_1 \\ \Phi_2 \\ \vdots \\ \Phi_{N_g-1} \\ \Phi_{N_g} \end{pmatrix} = \frac{(\Delta x)^2}{\varepsilon_0} \begin{pmatrix} \rho_1 \\ \rho_2 \\ \vdots \\ \rho_{N_g-1} \\ \rho_{N_g} \end{pmatrix}. \quad (3.1.12)$$

In equation 3.1.12 the ones in  $\underline{\underline{A}}$  in the bottom left and top right corner indicate periodic boundary conditions.

The generalization to higher dimensions is easily possible. The matrix  $\underline{\underline{A}}$  resembles this in sidebands below and above the tridiagonal band  $\{1, -2, 1\}$ . Because the left hand side of the Poisson equation depends only on geometry, resulting in a constant matrix  $\underline{\underline{A}}$ , the numerical inversion of the matrix has to be done once. In order to yield the potential one only has to calculate the backsolve

$$\Phi = \underline{\underline{A}}^{-1} \underline{\underline{A}} \cdot \underline{\Phi} = \frac{(\Delta x)^2}{\varepsilon_0} \underline{\underline{A}}^{-1} \underline{\rho}. \quad (3.1.13)$$

The introduction of the grid electric field reduces the numerical workload of the force calculation drastically. Let  $N_g$  be the number of grid points in 1D. The time for solving with PIC scales  $\mathcal{O}(N_g \ln N_g + N_p)$ . Since  $N_g$  is usually much lower than  $N_p$  further performance is gained.

### 3.1.2.4 Influence of collisions - Monte Carlo Collision (MCC) model

Up to now we considered an idealized plasma without collisions. However, collisional effects are very important in low temperature plasmas. An estimate of collisional effects is given by the comparison of characteristic lengths such as the mean free paths of the charge carriers  $\lambda$  with the system length  $L$ . In general, collisions change the shape of the energy distribution function, which might significantly alter the physics involved.

In a weakly-ionized plasma densities of neutrals by far exceed densities of the charged constituents. Thus, the neutral species in the simulation can be considered as a background with fixed density and temperature. Only the dynamics of electrons and ions is followed.

A self-sustained model of low temperature plasmas needs a proper handling of ionization and excitation collisions, because the maintenance of the plasma is based on relevant atomic processes. Supplementary Monte Carlo collision (MCC) routines between plasma particles have been added by K. Matyash [30] following a similar approach to Vahedi et al. [42, 43]. This includes ionization, excitation, recombination, dissociation and charge exchange collisions between different particle species (c.f. A.2).

Particles within a cell are ordered to pairs and are collided randomly according to the individual probability

$$p_\alpha = 1 - \exp(-un_\beta\sigma(E)\Delta t_{coll}). \quad (3.1.14)$$

This is the probability for the pseudo-particle  $\alpha$  to collide with relative velocity  $u$  to the target  $\beta$ . Further, the density  $n_\beta$  for the target and the specific cross-section  $\sigma(E)$  of the collision should be known. The average time between collisions is denoted by  $\Delta t_{coll}$ . The essence of Monte Carlo methods is now to compare such probabilities with random numbers. If a uniformly distributed random number  $R$  between  $0 \leq R \leq 1$  is smaller than the probability of particle  $\alpha$  to collide, the collision is performed. In this model only the velocities are changed depending on the type of the collision. A detailed explanation of the collisions involved can be found in [30].

Coulomb collisions cannot be neglected in many cases of low temperature plasmas as well. They result in the population of the high energy tails of the electron energy distribution function, which directly influences the atomic physics processes with large threshold energies, for instance, ionization and excitation.

As mentioned before, the spatial resolution in PIC is restricted to the grid size

$\Delta x < \lambda_D$ . Close-range interactions between charged particles inside one cell are underestimated. Therefore, additional elastic Coulomb collisions are needed in order to resolve collisions with impact parameter  $b$  smaller than the Debye shielding length  $b < \lambda_D$  without refining the mesh.

For this purpose a binary collision model has been added conforming to Takizuka and Abe [44]. Particles within the same cell are randomly ordered to pairs and then collided. Again, only velocities are changed. Six variables exist for such a collision in three-dimensional space between two particles. Conservation constraints leave two parameters to be free: the scattering angle and azimuth angle. These are chosen from certain angle distributions by a Monte Carlo technique. Now, the essence of a collision consists in a rotation of the relative velocity of the particles by these angles, which explicitly conserves energy and momentum. At last, the velocities are updated according to the change of relative velocity. This represents just a scattering by a small angle. By doing so, a series of consecutive weak binary collisions can result in a large angle deflection.

### 3.1.3 Characteristics of the argon background plasma

The background plasma is calculated by the PIC-MCC model mentioned above. The motion is resolved in three dimensions in space and velocity (3D3V) self-consistently. Argon is modelled as the working gas. Initially, particles are randomly distributed over the calculation domain. Each electron's velocity is assigned such, that the initial energy distribution is Maxwellian with a temperature of  $2.5 \text{ eV}$ . Further, the ratio of  $T_e/T_i$  is set to 100. The neutral gas temperature is fixed to  $300 \text{ K}$  at a pressure of  $50 \text{ Pa}$ . These have to be set for the Monte Carlo collision routines although PIC itself is scale invariant.

Given the parameters as above, the calculation results in a bulk electron plasma frequency  $\omega_{pe} = 1.8 \text{ GHz}$  and a bulk electron Debye length  $\lambda_{De} = 372 \mu\text{m}$ . Now, the spatial and temporal dimensions of the discharge are adjusted, since  $\Delta t = 0.2(\omega_{pe})^{-1} = 1.12 \cdot 10^{-10} \text{ s}$  and  $\Delta x = 0.5\lambda_{De}$  for the stability of the simulation.

The three-dimensional computational domain is split into  $8 \times 128 \times 8$  PIC cells in x-,y- and z-direction, respectively. This corresponds to a discharge of volume  $0.15 \text{ cm} \times 2.4 \text{ cm} \times 0.15 \text{ cm}$ . Furthermore, the whole computational domain is split in axial direction into eight pieces each calculated by a separate CPU core. The code uses MPI (Message Passing Interface) for the distribution. The domain is limited in y-direction by ideally particle absorbing electrodes. The lower electrode at  $y = 0 (0 \text{ cm})$  is driven by a sinusoidal voltage of  $f_{rf} = 13.56 \text{ MHz}$  with  $50 \text{ V}$  amplitude. The upper electrode at  $y = 129 (2.4 \text{ cm})$  is grounded. If particles cross those boundaries they are absorbed and taken out of the compu-

tation. In x- and z-direction the domain is periodic, i.e. if for instance a particle exceeds the boundary in x-direction at 8 (0.15 cm) it is reinjected with proper momentum and position near  $x = 0$  (0 cm).

The results shown on the following pages are average values over 6000 rf cycles to guarantee good statistics. This is of special importance for the distribution functions. Fast fluctuations such as statistical noise are smoothed out.

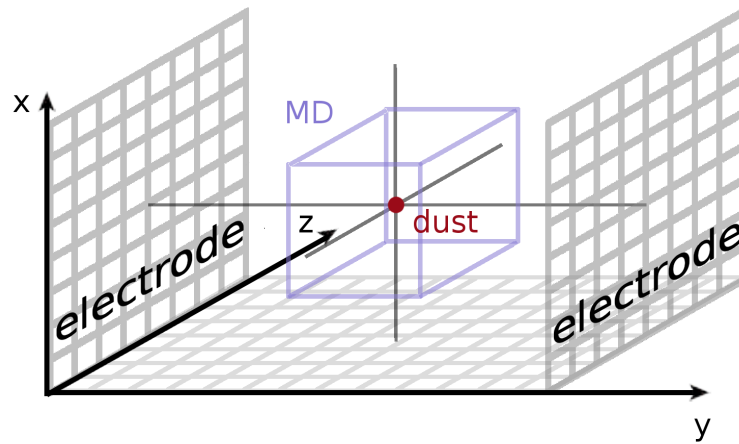


Figure 3.3: Sketch of the three-dimensional computational PIC grid. Also indicated is the MD region around the dust.

After a transient phase the simulation reaches a dynamic equilibrium. The plasma is sustained by the applied rf discharge. Fast electrons ionize neutrals, thus compensating for the losses at the electrodes. This simulation delivers a complete three-dimensional picture of the discharge. But due to the symmetry in boundary conditions used the discharge itself is just one-dimensional along the axial dimension. After averaging, any spatial variation in x- and z-direction is smoothed out. Therefore, the plots of the discharge properties show only the dependence in y-direction, perpendicular to the electrodes.

For the description of a plasma the methods of statistical mechanics provide a useful description. Suppose, there are on average  $f(\underline{x}, \underline{v}) d^3\underline{x} d^3\underline{v}$  particles at each position  $\underline{x}$  with velocity  $\underline{v}$  in a volume element  $d^3\underline{x} d^3\underline{v}$  of phase space. Then,  $f$  is a so-called distribution function.

The ensemble-averaged moments of the velocity distribution function

$$\underline{m}^k = \int f(\underline{v})(\underline{v})^k d^3\underline{v} \quad (3.1.15)$$

have important physical meanings. Particle density, mean velocity and temperature correspond to the zeroth, first and second moment of the distribution function, respectively. If the distribution function is known, then in principle the complete dynamical description is given.

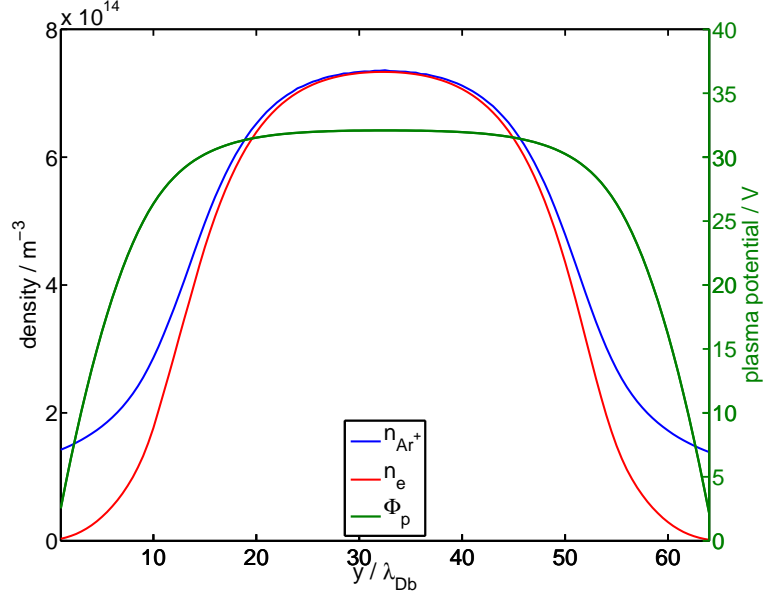


Figure 3.4: Time-averaged densities of electrons and ions plus the plasma potential.

In Fig. 3.4 the time-averaged plasma potential, electron and ion densities are shown. The electron density decreases faster than the ion density towards the electrodes. The maximum plasma density is about  $7.2 \cdot 10^{14} \text{ m}^{-3}$ , which corresponds to a weakly-ionized plasma with ionization degree  $\kappa \approx 10^{-5}$ . The bulk plasma satisfies quasi-neutrality leading to a flat potential profile, whereas the potential drops towards the wall, because of the charge imbalance. The sheath width is approximately about 15 Debye lengths.

In the temperature plots we refer to the temperature as the second moment of the velocity distribution function

$$T = \frac{m}{2} (\langle v^2 \rangle - \langle v \rangle^2) \quad (3.1.16)$$

not as the average energy at thermal equilibrium as stated in thermodynamics. This is equal to the variance of the velocity of the particles.

Towards the walls the temperature decreases see Fig. 3.5. The strong electric field leads to a conversion from thermal to potential energy. Very close to the electrodes no evaluation of the electron energy or temperature is possible due to electron depletion.

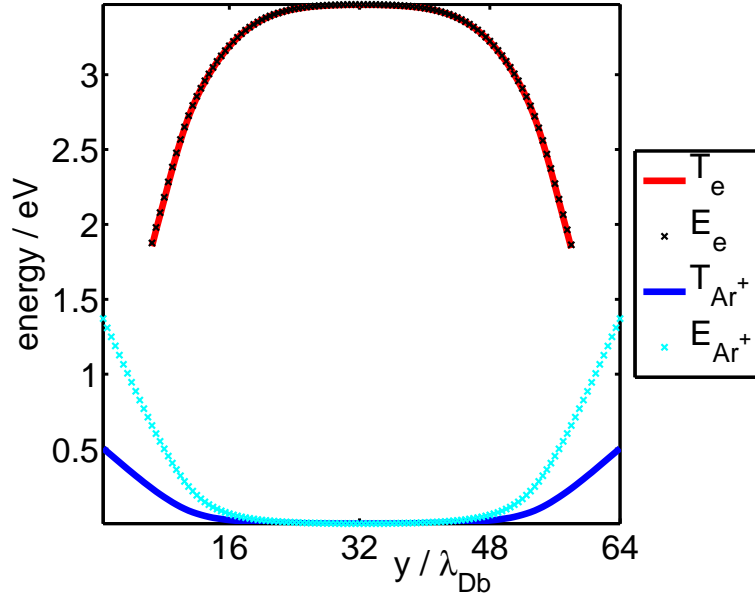


Figure 3.5: Averaged total and thermal energy for electrons and ions. Acceleration in the sheath increases the total energy of the ions so much that their energy is scaled by the factor 1/100.

Table 3.1 lists the resulting plasma discharge characteristics and various length scales after the simulation converged.

neutral density $n_n$	$1.2 \cdot 10^{22} \text{ m}^{-3}$
maximum plasma density $n_e \approx n_i$	$7.2 \cdot 10^{14} \text{ m}^{-3}$
maximum electron temperature $T_e$	$3.5 \text{ eV}$
electron Debye length $\lambda_{De}$	$655 \text{ } \mu\text{m}$
system length $L$ along discharge	$2.4 \text{ cm}$
mfp of electron-neutral collisions $\lambda_{e-n}$	$830 \text{ } \mu\text{m}$
mfp of inelastic collision $\lambda_{inel}$	$2.6 \text{ mm}$
mfp of charge exchange collisions $\lambda_{Ar^+-Ar}$	$83 \text{ } \mu\text{m}$

Table 3.1: Discharge characteristics and various length scales of the simulated CCRF.

The influence of collisions can be seen in the velocity distribution as well. Especially, the electron-neutral collisions, having the shortest mean free path  $\lambda_{e-n} \sim \frac{1}{\sigma_{e-n} \cdot n_n} \sim 830 \mu m$ , alter the distribution function of the electrons. The length of the discharge,  $L = 2.4 \text{ cm}$ , is much larger than the mean free path of the electrons. Therefore, the electron velocity distribution function (EVDF) in figure 3.6 shows a non-Maxwellian rather Druyvesteyn-like behaviour, which results in a diminished number of high-energy electrons indicating Ohmic heating. Electrons are repelled by expanding electric fields in the sheaths, thereby, getting accelerated between successive elastic collisions with neutrals. This has also been found in previous calculations [29, 30, 35, 45]. Similar distribution functions have been experimentally found in CCRF discharges by Godyak [46]. The mean free path for inelastic electron-neutral collisions  $\lambda_{inel} \sim \frac{1}{\sigma_{inel} \cdot n_n} \sim 2.6 \text{ mm}$  is about the same order as the elastic electron-neutral collisions. In figure 3.6 we can see that electrons cool down slightly towards the centre of the discharge. This rate is sufficient to ionize enough plasma particles to sustain the discharge. Because of this inelastic collision do play an important role in low temperature laboratory plasmas.

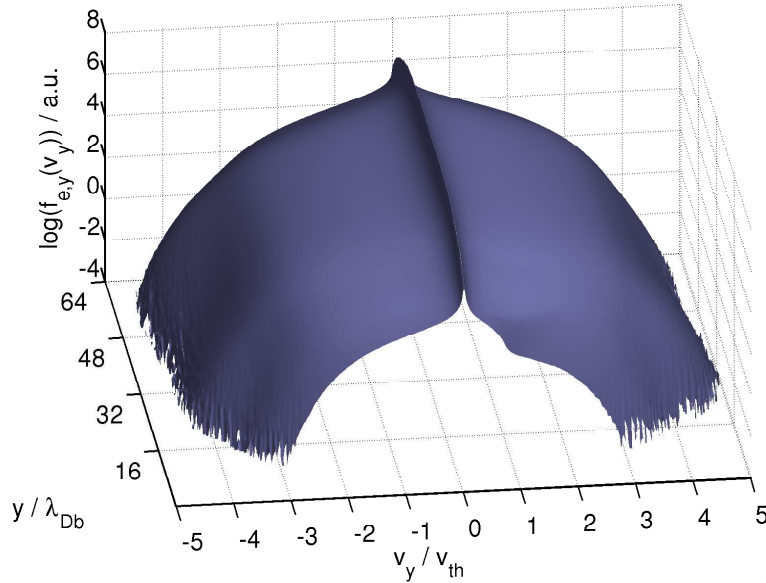


Figure 3.6: Averaged distribution function of the axial component of the electron velocity (EVDF). The distribution is Druyvesteyn-like indicating Ohmic heating.

Ions have a different velocity distributions. Their mobility is smaller compared to electrons, because of their higher mass. As a consequence ions experience only a time-averaged electric field. As seen in figure 3.5 the ions are cold in the

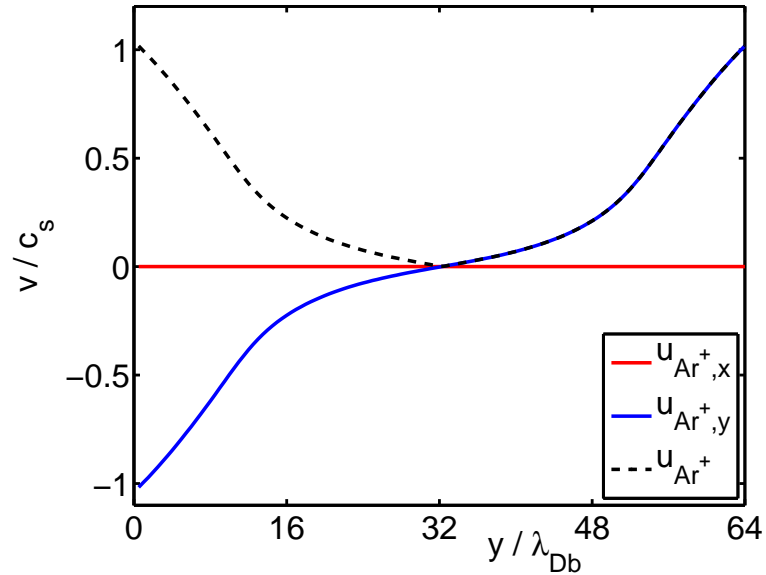


Figure 3.7: Time-averaged ion velocity distribution function.

middle of the discharge. Their thermal energy is close to the thermal energy of the neutral background gas, specifically around  $300\text{ K}$ . But within the sheaths ions get quickly accelerated by the mean rf electric field towards the material walls to balance fluxes, also seen in figure 3.7. Some ions surpass sonic speed, even reaching Mach 5 at the wall (see Fig. 3.8).

This rf plasma background calculated with the PIC-MCC model is the starting point for introducing dust particles into the simulation. Those highly charged particles are responsible for the peculiarities of complex plasmas requiring microscopic models resolving both the plasma and the dust. The orbital motion close to the dust is resolved in this work by introducing into the PIC model a MD region close to the dust, accounting for the close-range effects of the dust to the plasma.

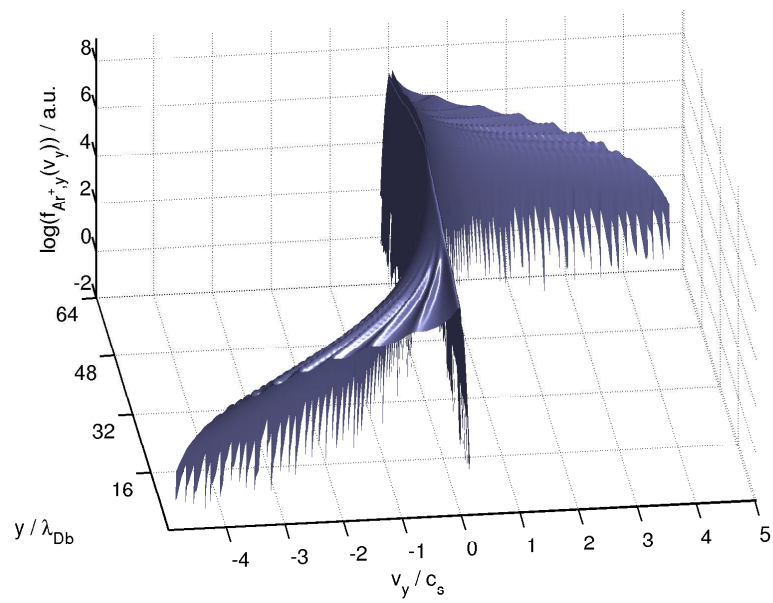


Figure 3.8: Averaged distribution function of the axial component of the ion velocity (IVDF).

## 3.2 Charging processes and surface effects of dust in CCRF plasmas

The prevailing mechanism of dust particle charging in low temperature laboratory plasmas is the absorption of ions and electrons. In such an environment a dust grain acts like a floating probe. Due to the higher electron mobility the grain gains a negative charge [47, 48]. As a result, a typical micrometre-sized particle gathers several thousand elementary charges. This results in a negative floating potential, which attracts ions and repels electrons (see Fig. 3.9). Especially in astrophysical environments, surface effects also alter the particle charge significantly.

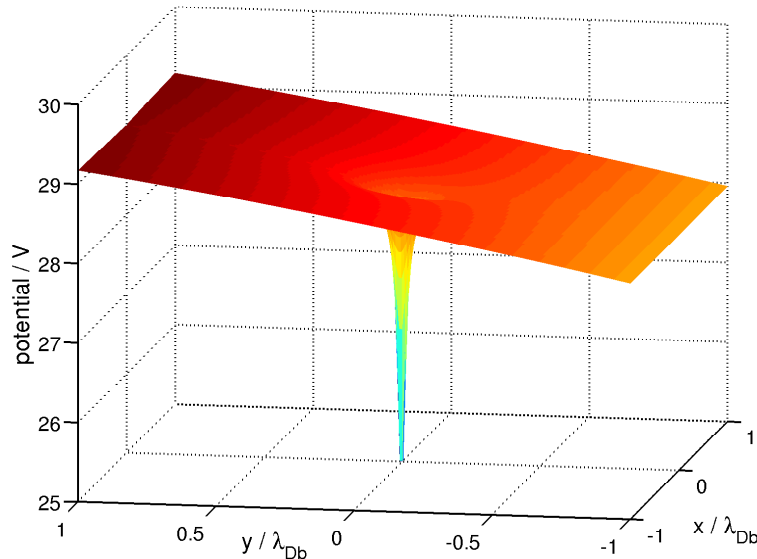


Figure 3.9: Averaged two-dimensional potential of the MD region.

The theory about dust charging originated from the study of the currents for Langmuir probes [48], but because of the similarities it is also applicable in complex plasmas. This first approach, called Orbital Motion Limit (OML), was already developed in 1926 by Mott-Smith and Langmuir. Although the probe problem has long been known, it is still not fully understood including all peculiarities such as non-Maxwellian distributions in a non-neutral, collisional plasma sheath surrounding. The inherent complexity and the large number of parameters, e.g. collisionality, ratios of ion to electron temperatures or the dust radius

to Debye length make the problem very difficult.

### 3.2.1 Orbital Motion Limit (OML)

A well spread approach for the problem described above is the Orbital Motion Limit (OML) [48], which gives generally reasonable estimates of the charge  $Q_{dust}$  and the floating potential  $\Phi_{fl}$  of the dust.

Suppose electrons and ions move collisionless from infinity towards the dust and are then subjected to the electrostatic interaction with the dust grain.

Usually, the dust is charged negatively and has a negative floating potential  $\Phi_{fl}$  with respect to the plasma potential  $\Phi_p$ . Consequently, electrons are repelled and ions are attracted.

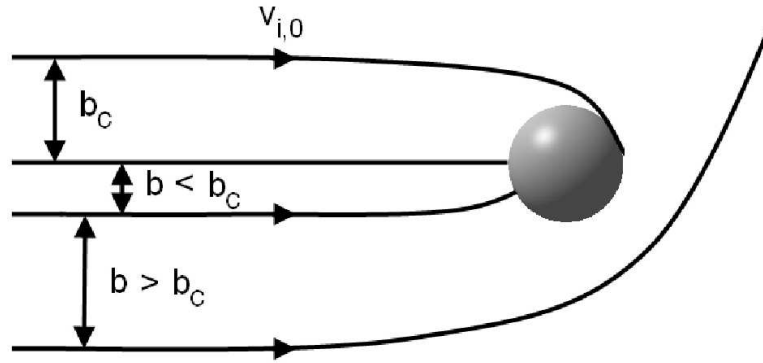


Figure 3.10: Sketch of the ion trajectories for various impact parameters  $b$ . Particles with critical impact parameter  $b_c$  will hit the dust surface with grazing incident.

Examples of ion trajectories are shown in figure 3.10. The critical impact parameter is  $b_c$ , where ions will graze the dust particle's surface. Ions with impact parameter  $b > b_c$  may be deflected, but only for  $b \leq b_c$  particles are absorbed. Due to the electrostatic potential the cross sections for ions and electrons are modified  $\sigma_c(v_i) = \pi b_c^2$  with respect to the hard sphere cross-section. The radius of the dust is in the following denoted by  $R_{dust}$ . From angular momentum

$$\underline{L} = \underline{r} \times \underline{p} \Rightarrow m_i b_c v_{i,0} = m_i R_{dust} v_i \quad (3.2.1)$$

and energy conservation of a particle with critical impact parameter moving from

$-\infty$  to the dust

$$\frac{m_i}{2}v_{i,0}^2 = \frac{m_i}{2}v_i^2 + e\Phi_{fl} \quad (3.2.2)$$

follows

$$b_c^2 = R_{dust}^2 \left( 1 - \frac{2e\Phi_{fl}}{m_i v_{i,0}^2} \right). \quad (3.2.3)$$

An additional assumption of OML theory is a Maxwellian distribution  $f(v_i)$  of the velocities. The ion contribution to the charging current is then obtained by integrating over the Maxwellian distribution

$$I_i = j(v_i)\sigma_c(v_i) = e \int_0^\infty f(v_i)v_i\sigma_c(v_i)dv_i \quad (3.2.4)$$

resulting in

$$I_i = \pi R_{dust}^2 \left( 1 - \frac{e\Phi_{fl}}{kT_i} \right) n_i e \sqrt{\frac{8kT_i}{\pi m_i}}. \quad (3.2.5)$$

In other words, the ion current consists of the ion current density  $j_i = en_i v_{i,th}$  at ion thermal velocity  $v_{i,th} = \sqrt{\frac{8kT_i}{\pi m_i}}$  with an increased cross section of  $\pi R_{dust}^2 \left( 1 - \frac{e\Phi_{fl}}{kT_i} \right)$ . Similarly, the calculation for the electrons gives

$$I_e = -\pi R_{dust}^2 \exp\left(\frac{e\Phi_{fl}}{kT_e}\right) n_e e \sqrt{\frac{8kT_e}{\pi m_e}}. \quad (3.2.6)$$

In equilibrium both currents balance  $I_i = I_e$ , leading to an expression for calculating the floating potential  $\Phi_{fl}$

$$1 - \frac{e\Phi_{fl}}{kT_i} = \exp\left(\frac{e\Phi_{fl}}{kT_e}\right) \frac{n_e}{n_i} \sqrt{\frac{T_e m_i}{T_i m_e}}. \quad (3.2.7)$$

The ratio of the bulk temperatures in our PIC-MCC model is  $T_e/T_i \approx 13.2$ . Assuming a quasi-neutral environment  $n_e \approx n_i$  plus the afore mentioned assumptions one can find an approximate solution of equation (3.2.7), giving an estimate for the floating potential  $\Phi_{fl} = -3.14 kT_e/e$ . According to Whipple [49] an isolated dust particle with radius  $a$  smaller than the Debye length  $R_{dust} \ll \lambda_D$ , as it is in the following simulation, can be idealized as a spherical capacitor. The dust charge  $Q_{dust} = C\Phi_{fl}$  depends linearly on the floating potential. The slope is called the capacitance

$$C = 4\pi\epsilon_0 R_{dust} \left( 1 + \frac{R_{dust}}{\lambda_D} \right) \stackrel{R_{dust} \ll \lambda_D}{\approx} 4\pi\epsilon_0 R_{dust}. \quad (3.2.8)$$

### Charging time

The time scale for the charging  $\tau$  of a dust charge can be deduced in OML theory [50] from eq. (3.2.5)

$$\frac{dQ_{dust}}{dt} = I_i = \pi R_{dust}^2 \left( 1 - \frac{e\Phi_{fl}}{kT_i} \right) n_i e v_{th,i}. \quad (3.2.9)$$

Although the electrons are more mobile  $\tau_e \ll \tau_i$ , the governing time scale for charging is determined by the ions  $\tau_i$  due to the ambipolarity of fluxes. This problem results in an inhomogeneous differential equation similar to the RC circuit problem, if the particle potential is replaced by

$$\frac{dQ_{dust}}{dt} = \pi R_{dust}^2 \left( 1 - \frac{eQ}{4\pi\epsilon_0 R_{dust} kT_i} \right) n_i e v_{th,i}, \quad (3.2.10)$$

which has the following solution

$$Q_{dust}(t) = Q_0 \exp^{-t/\tau_i} + 4\pi\epsilon_0 R_{dust} \frac{kT_i}{e} \quad (3.2.11)$$

with the charging time

$$\tau_i = 4\pi\epsilon_0 R_{dust} k \frac{kT_i}{e} (\pi R_{dust}^2 e n_i v_{th,i})^{-1}. \quad (3.2.12)$$

$\tau_0$  can be considered as the time scale of the RC element  $\tau = RC$ . The capacitance is given by eq. (3.2.8), whereas the resistance is supplied by Ohm's law  $R = U/(\pi R_{dust}^2 j_i)$  with the inherent particle potential  $U = k_B T_i/e$ . With an ion density  $n_i = 10^{15} \text{ m}^{-3}$ , the charging time is of the order of  $\tau_i = 4.6 \mu\text{s}$ . It has been shown that at low-pressures and low plasma densities the finite charging time can excite oscillations as the particle moves within the sheath [51].

OML is just one approach to describe the particle charging. Generally, the effect of collisions is to diminish the currents to the surface of the object, since particles diffuse to the surface rather than reaching by free flight. But for low-collisionality regimes the so-called trapped ion effect might even lead to an enhanced capturing of ions [52–54] for probes and dust grains. In astrophysical environments electron emission caused by the photoeffect or by impinging energetic particles additionally alters the net fluxes to the grain [55].

Another interesting approach is a charging model based on quantum mechanical considerations [56]. In this model the electrons are bound in polarization states in front of the grain's surface, while the ions behave classically as a screening charge. The authors claim that ions initially bind far away from the surface. Only inelastic processes caused by the plasma yield in transitions to lower bound states.

Therefore, the charge of the dust only depends on the balance of the incident electron flux with the electron desorption flux at an effective surface.

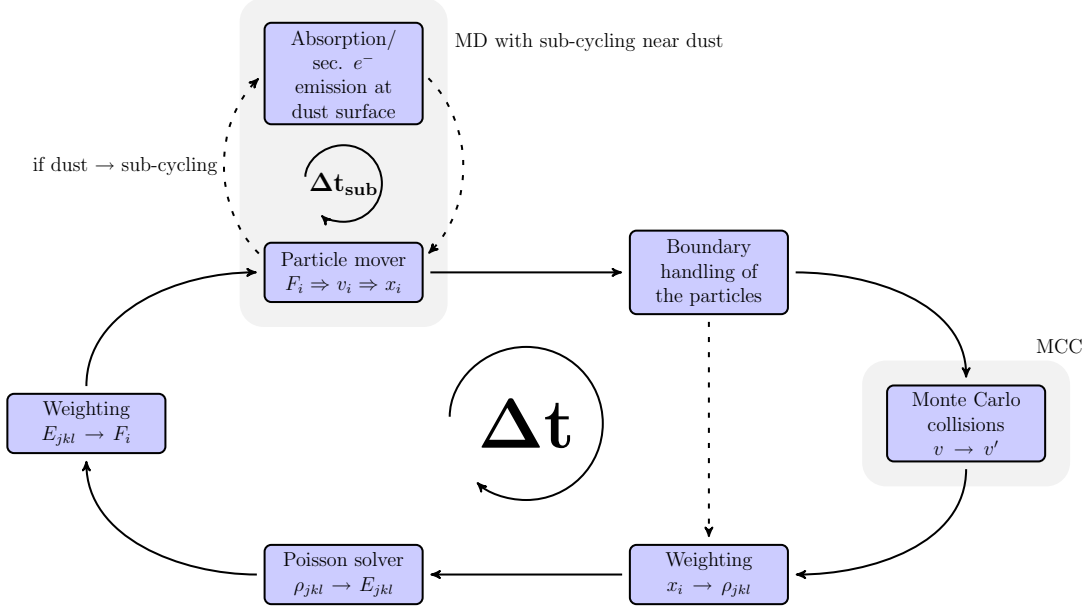
### 3.2.2 P<sup>3</sup>M MCC model

The spatial resolution in PIC schemes is restricted by the grid size  $\Delta x$ , which itself is bound by the Debye length  $\lambda_D$  for the simulation of plasmas. Particles are smeared out over the grid size as charged clouds. As stated before, the interaction between these clouds lacks the proper Coulomb repulsion at small distances. If particles approach, they are even able to move through each other. In laboratory low temperature plasmas the Debye length results in a grid size corresponding to several hundreds of microns. Contrary to that, the diameter of dust grains is smaller, usually about several microns. Therefore, the conventional PIC scheme fails to resolve short-range interactions between dust and plasma particles.

A dust particle immersed in a plasma changes the particle behaviour in its vicinity. In order to unravel close encounters of particles with the dust properly and to calculate the system in a feasible time the particle-particle particle-mesh P<sup>3</sup>M model of *Matyash et al.* [35] combines a MD and a PIC simulation. When electrons and ions approach the dust closer than a certain distance (of the order of the Debye length), the code changes the force calculation. Within the MD region PIC is still used to calculate the plasma background, but an additional MD force calculation between dust and plasma particles resolves close-range distances. Special care is taken in the simulation of the interaction force between dust and plasma particles, since the dust charge already contributes to the electric field  $E_{grid}$  in the PIC part. This contribution  $E_{grid,dust}$  is replaced by a direct particle-particle scheme using exact Coulomb electric field  $E_{Coulomb}$ . The resulting electrostatic field is thus calculated:  $E = E_{grid} - E_{grid,dust} + E_{Coulomb}$ . By accounting for finite-size effects this method allows to follow particle trajectories in the vicinity of the dust particle. The charging of dust particles due to the absorption of electrons and ions is resolved self-consistently.

A better time resolution is provided by a sub-cycling scheme. The electron and ion time-step is diminished by a certain factor in order to resolve fast motions on the smaller scale. Particles which exceed the dust grain radius are assumed to be absorbed and removed from the calculation, whereas the dust charge is updated after each MD time step.

This allows us to resolve the charging due to absorption of electrons and ions self-consistently [40]. In summary, the idea of the P<sup>3</sup>M MCC model is to include


 Figure 3.11: Scheme of the whole P<sup>3</sup>M MCC cycle

a MD region to the afore mentioned PIC-MCC model in order to resolve the finite-size effects of dust grains (see figure 3.11).

### 3.2.3 Charging of dust particles

The model described before allows a microscopic and self-consistent description of the dust charging. It has been validated in magnetized plasmas [31], where it has shown good agreement with OML predictions.

Here, a particle with  $5 \mu\text{m}$  radius is modelled. The position of this dust particle is fixed at  $4 \times 24 \times 4$  in internal coordinates of the simulation. This corresponds to the equilibrium position under similar plasma conditions obtained in [57].

In a transient phase the particle charges up according to the incident fluxes on the dust grain's surface. The calculation shows a charging time of about  $5 \mu\text{s}$ , which is in good agreement with the predicted  $4.6 \mu\text{s}$  by OML. Essentially, this is much faster than the dynamics of dust grains in low temperature plasmas. For this reason the charging should normally hardly affect the dust dynamics. If a dust particle is put into the plasma, it will instantaneously adapt its charge to the local plasma surrounding. Once levitating, when the electrostatic force compensates the gravitational force, the motion of dust particles is rather limited. Therefore it should not be a drawback of the model to fix the particle's position.

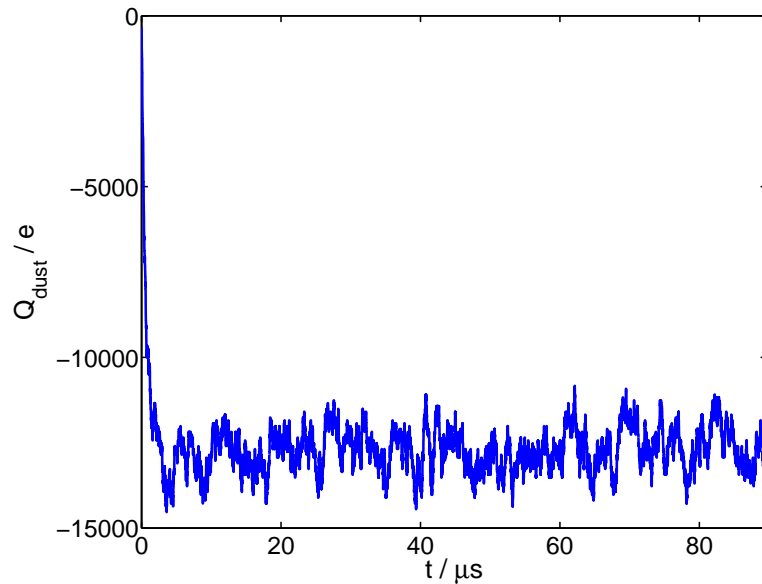


Figure 3.12: Temporal dependence of the dust charge for a particle with radius  $R_{dust} = 5 \mu\text{m}$ .

The finite charging time can have influences on dynamics as stated by Nunomura et al. [51]. They attributed the finite charging time of particles to the excitation of spontaneous oscillations. With a delay due to the finite time, the charge varies according to the local plasma conditions as the particle moves.

The dust particle in the simulation has an equilibrium charge of 12000 to 13000 elementary charges. Only the influx of electrons and ions determined the charge. After the equilibration process of the simulation the electron temperature is about  $3.5 \text{ eV}$ . OML theory estimates with equation (3.2.7) a floating potential  $\Phi_{fl} = -11 \text{ eV}$  and with equation (3.2.8) a resulting dust charge  $Q_{dust} = -38000 e$ . Compared to OML the dust is much more positive, also reflected in the floating potential of  $\Phi_{fl} \approx -3.1 \text{ eV}$  as seen in figure 3.9. The main reason for the differences is that the dust is placed in the sheath, whereas the theory assumes a bulk plasma.

The dust charge is determined by the influx of charges. Shown in figure 3.13 is the flux of electrons and ions. The speed is used for the calculation of the flux. In the sheath the ion flux  $\Gamma_i = n_i v_i$  is constant, since the drop in density compensates the increasing velocity. Continuity is a consequence of the absence of sources and sinks like ionization and recombination.

Due to the higher electron velocity and comparable densities electron fluxes exceed ion fluxes by a factor of 1000 at dust position. This is smaller than the ratio

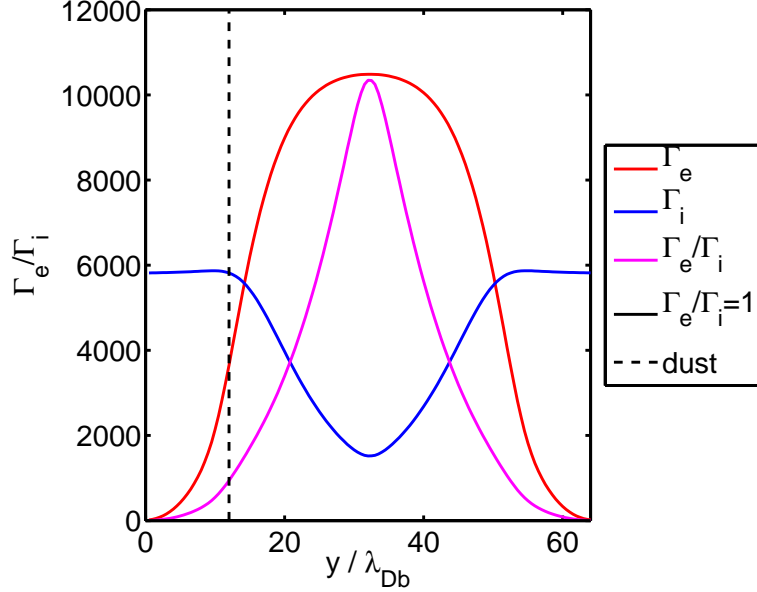


Figure 3.13: Flux densities  $\Gamma_{\{e,i\}}$  and their ratio. The flux densities are scaled to fit the scale of the flux ratio.

of the fluxes in the bulk. This ratio decreases towards the electrodes symmetrically. The less the influx of electrons the less potential is needed to balance ion and electron fluxes. Dust particles would exhibit smaller charges if moved closer to that wall.

Another possible explanation for the diminished magnitude of the charge potential might be caused by collisional effects in the vicinity of the dust, which are neglected in OML theory [54]. It has been shown theoretically and experimentally that rare collisions increase the ion flux to the dust particle [52, 53]. At higher collisionalities this effect might be reversed, when collisions happen so frequently that the mobility of the ions is restricted.

Most theories about the fluxes towards the charges deal with continuous variables. But in reality and in the particle simulation (super-particle formalism of PIC) the fluxes resemble a sequence of discrete absorption events by the grain's surface. The time interval and sequence between consecutive events can be described as a stationary Markovian process. Therefore, the dust charge fluctuates around an average value  $Q_{dust}$ . These fluctuations can affect dust coagulation and cause instabilities [58]. In complex plasmas these fluctuations are always present, which makes the properties of complex plasmas different to "ordinary" multicomponent plasma, but also stresses the importance of a proper under-

standing of the fluctuations.

Matsoukas and similarly Khrapak obtained an expression for the amplitude of the charge fluctuation [54, 59, 60]. They deduced the amplitude of the fluctuation from the ratio of thermal energy to electrostatic potential at dust radius. They would predict a variance of 80 elementary charges  $e$  under these plasma conditions.

Cui and Goree simulated the charge fluctuations based on OML theory. Similarly, the fluctuations are  $\Delta Q_{rms} \approx 0.5\sqrt{Q_{dust}} \approx 60$  as in the statistics of the counting independent events. Their outcome seems to contradict to the results presented here, where the charge fluctuates with an amplitude up to 1000  $e$ . This an order more than the prior authors claim. But accounting for the super-particle method, where one super-particle in the simulation corresponds to 84 real particles results in an enhancement of a factor 9 of the fluctuations. Additionally, estimates assumed a stationary environment, but this is not the case as will be discussed in detail in the next chapter. The non-stationarity of the rf will increase fluctuations. Therefore, the estimate give the right order of magnitude of the charge fluctuations.

### 3.2.4 Emission effects on the charging

Usually, the balance between electron and ion fluxes is the process determining the total charge of a dust particle in low temperature plasmas. But especially in astrophysical plasmas the charge of the dust changes due to photo-, thermionic and secondary electron emissions, which might even lead to a positive charge.

#### 3.2.4.1 Secondary electron emission

If an incident or often called primary particle impinges the surface of a dust grain, there are several ways of surface interaction [61] depending on the energy of the primary particle. The energy distribution of the reflected electrons shows two peaks (compare 3.2.4.1). One appears at low energies and the other one close to the energy of the incident electrons.

Firstly, the primary electron can be reflected elastically, resulting in the latter peak in the energy distribution. This is the most probable interaction, if energies are low, so this interaction may take place at the walls of low temperature plasmas. With increasing energy the primary particle might interact with more atoms at the surface and is then released (or releases many electrons), yielding the so-called rediffused electrons, which gives the background level in the energy

distribution. Finally, the incident particle can interact in a more complicated way, if the energy is sufficient to allow an interaction more deeply in the wall, releasing the "true" secondary electrons.

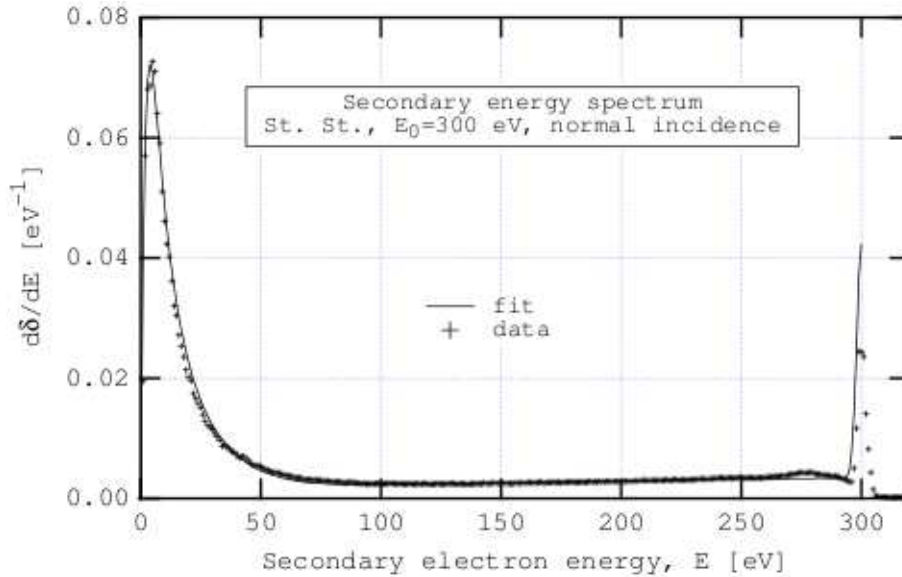


Figure 3.14: Example of Furman's model for secondary electron emission. It shows a measured, representative secondary electron emission yield (for copper) and its fit according to the model. This figure is taken from [61].

This picture of secondary electron emission is supported by the measured energy spectrum for various materials.

A routine for secondary electron emission from the dust is included in the simulation model. The low energy of impinging electrons from the plasma surrounding is modelled as elastic scattering. If a particle hits the surface in the calculation, particles are reflected with a certain, variable probability.

### 3.2.4.2 Photoemission

If a photon hits the surface of the dust, it might release an electron with energy  $h\nu - W$ , depending on the work function  $W$  of the material.

### 3.2.4.3 Thermionic emission

An electron occupies energy levels according to the Fermi-Dirac distribution in solids. Emission occurs, if the dust grain is heated. Then, electrons in the high-

energy tail of the Fermi distribution are able to surpass the work function. In general, the thermionic emission density  $j$  is described by the Richardson equation

$$j \propto T^2 \exp\left(\frac{e\Phi}{k_B T}\right) \quad (3.2.13)$$

and mainly depends on the temperature  $T$  of the dust.

### 3.2.5 Simulation of secondary electron emission

Until now, dust particles have been considered as floating probes, which balance ion and electron fluxes according to the plasma surrounding. In this section the influence of secondary electron emission on the surface of dust particles is accounted for. As we will see the dust potential, charge and fluxes adapt similar to as applying an additional electron current from the dust to the plasma. Still, the dust grain behaves like a probe, but the equilibrium charge is changed.

In the simulation an electron impinging the dust surface is ideally reflected with a preassigned probability. Also, the energy ratio before to after the collision event can be set.

Although the "probe" problem of a spherical object has long been known, the problem occurred already in the work of Mott-Smith and Langmuir [48] in 1926, it is still not fully understood [62].

Figure 3.15 shows the results of the charging of several dust particles with different probabilities  $p$  for secondary electron emission. The higher the probability for emission the less is the charge at equilibrium. Due to emission less plasma particles are captured, if they hit the surface. Instead, particles are reinjected and can be lost for the charging of the dust. In this way the electron flux to the dust is diminished. It is seen, that the fluctuations decrease with diminishing equilibrium charge as predicted by the theories of Goree and Khrapak.

Hobbs predicted the creation of double layers in case the emission surpasses critical emission coefficients [63]. For argon this would correspond to a critical probability for emission of 0.97. Figure 3.16 shows the dust potential for an emission probability of 0.98. The floating potential is dramatically decreased compared to the non-emitting case, since the net electron flux to the dust is diminished.

The potential profile is already flatening, nevertheless, no double layer occurs. In the theory of Hobbs a planar sheath was assumed. Hobbs calculated the critical value for a dc discharge. The potential gradients are larger in rf discharges. The

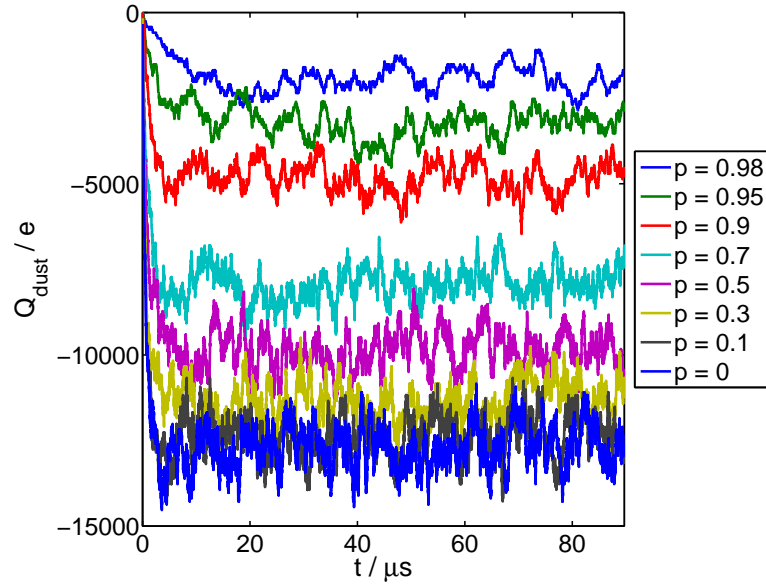


Figure 3.15: Temporal dependence of the charge for several emission probabilities  $p$ . The dust particle has a radius of  $5 \mu\text{m}$ .

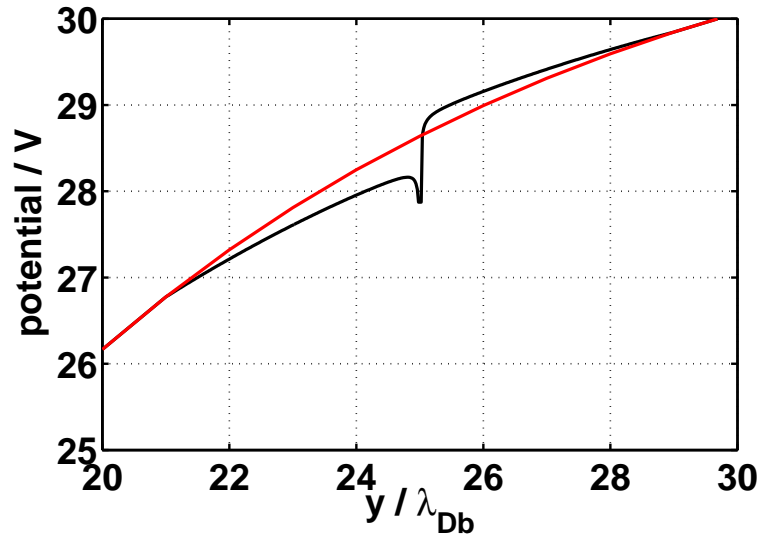


Figure 3.16: Plasma potential close to a dust particle with  $5 \mu\text{m}$  radius for an emission probability of 0.98. Indicated in red is the plain PIC solution, whereas the black line is the result of the  $P^3M$  model.

dynamics in conjunction with the spherical particle shape seem to prevent the building of double layers, at least for emission probabilities lower than one.

Here, it shall be stated, that if the secondary emission is too strong, the charge might be too little for the electrostatic force to compensate gravity. Then, the dust particle just falls through the sheath. In general, these results can be considered as a parametric study of the influence of emission on dust particle charging.

### 3.3 Synopsis

The aim of this chapter was to resolve the charging of dust particles in rf plasmas including the finite-size effects of the dust grain. For this purpose an extension of the Particle-in-Cell method was needed to allow a realistic description of the interaction of dust with plasma. A particle-particle particle-mesh ( $P^3M$ ) model was applied, where in a region close to the dust a molecular dynamics (MD) algorithm is used to calculate the close-range forces between dust and plasma particles. The CCRF plasmas used for dust experiments are operating in an intermediate collisionality regime. The plasma is not diffusion-restricted, but inelastic collision yielded in a Druyvesteyn-like electron energy distribution function.

With the  $P^3M$  model the charging of a single non-emitting dust grain in the sheath of a CCRF discharge was studied. The charging of a single non-emitting dust grain in the sheath of a CCRF discharge was studied. Deviations for the charge and potential predictions from orbital motion limit (OML) theory were observed. The temporal behaviour of the charging, namely charging time and fluctuations, fit the theoretical estimates well. Secondary electron emission from the dust surface was modelled implementing a Monte Carlo algorithm into the  $P^3M$  code. With increasing emission the equilibrium of the total flux is changed: the higher the secondary electron emission yield the lower the average charge. The double sheath predicted by theory for a planar geometry has not been found in front of dust particles for values of the secondary electron emission yield up to one.

# 4 Phase-resolved analysis of dusty CCRF plasmas

This chapter extends the microscopic analysis of dusty CCRF plasmas, resolving full rf dynamics of the discharge. The charging dynamics of a single dust particle is studied on a micro-scale in time. The simulations of CCRF discharges with and without dust can be compared and validated with phase-resolved optical emission spectroscopy (PROES). The effects of the rf dynamics on the charging of the dust will be analysed demonstrating the capability of the model to describe the microscopic dynamics of dust in rf plasmas. Experiments have shown an increased excitation, if dust particles are immersed. As a highlight, the model allows reasoning about the origin of the higher order effect in the difference in excitation.

## 4.1 Phase-resolved characteristics of the CCRF plasma

Charged particles, as electrons and ions, respond to changes in the plasma according to their plasma frequency  $\omega_p$  (see Eq. 3.1.5). The mobility of the ions is thus more restricted than for electrons, since the mass of ions is much larger than the mass of electrons. For the study of complex plasmas CCRF argon plasmas are commonly used, driven with a standard frequency of 13.56 MHz. Typical operation parameters for such a discharge are a density  $n_0 \approx n_e \approx n_i \sim 10^9 \text{ cm}^{-3}$  and electron temperature  $T_e \sim 3 \text{ eV}$ . Under those conditions the following relation holds

$$\omega_{pi} \approx 6.6 \text{ MHz} < \omega_{rf} = 2\pi \cdot 13.56 \text{ MHz} \ll \omega_{pe} \approx 1.78 \text{ GHz}. \quad (4.1.1)$$

The conditions in the sheath can now strongly differ at different phases in the rf cycle. Generally, plasma in contact with walls leads to a build-up of a plasma sheath as discussed already before (see 2.1.1 ). Material walls charge up negatively with respect to the plasma, because of the higher electron mobility. The

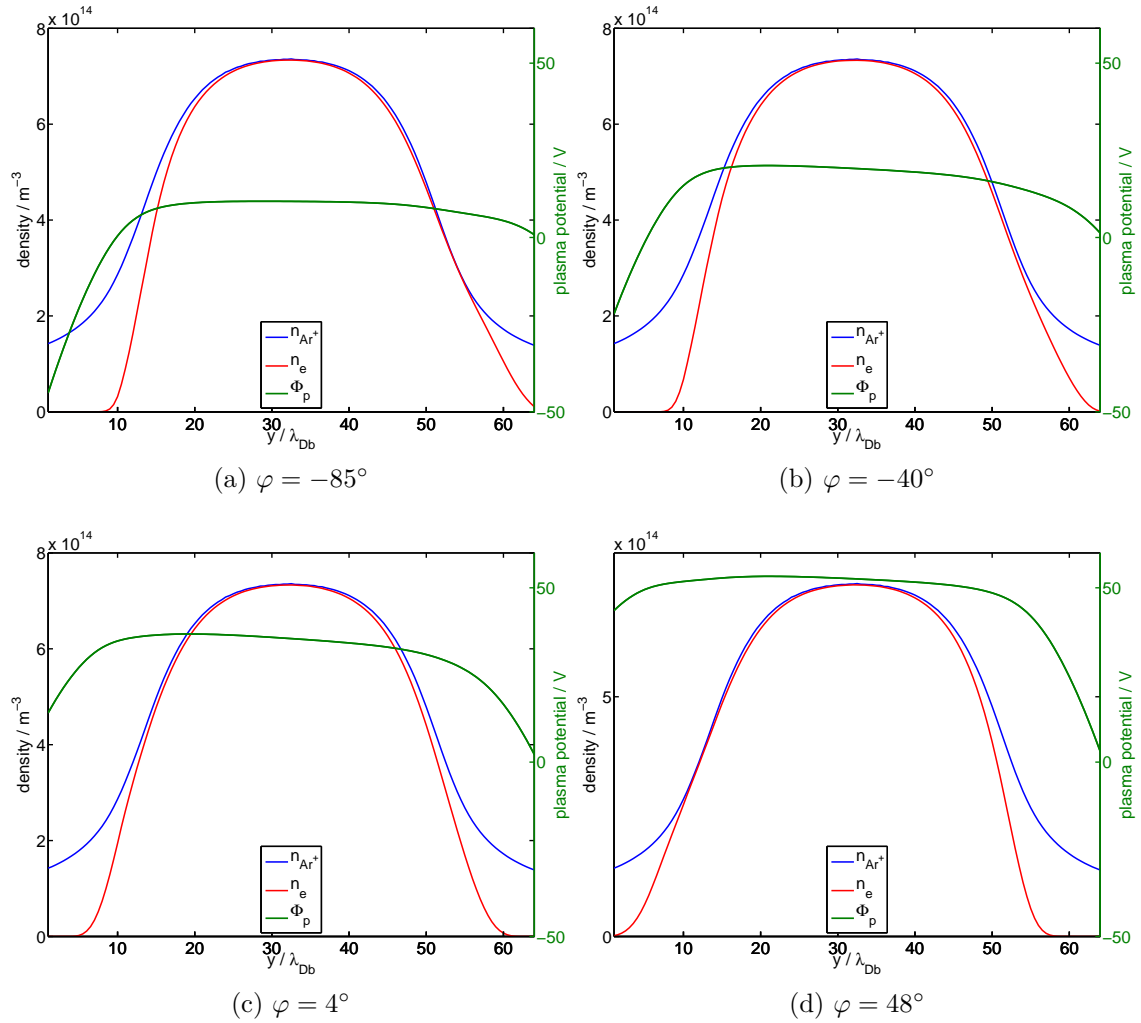


Figure 4.1: Phase resolved time-averaged densities of electrons and ions plus the plasma potential. The phase of the sinusoidal rf voltage is varied from  $\varphi = -85^\circ$  to  $\varphi = 226^\circ$ .

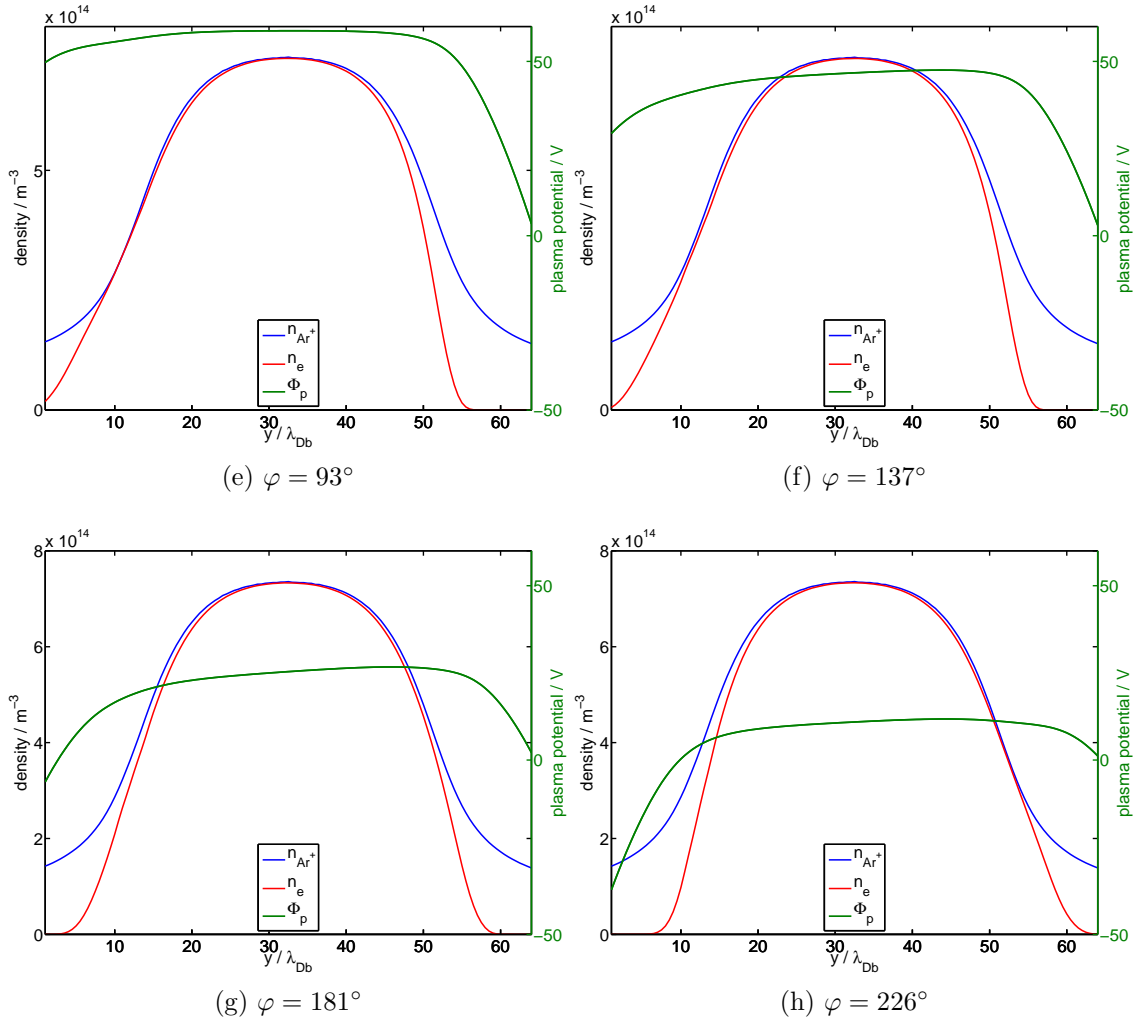


Figure 4.1: (continued)

electrons are repelled from the electrodes by strong electric fields.

Ions are too sluggish to follow the rf dynamics, because of their relatively large mass. They only experience a time averaged electric field of the rf sheath, which results in an acceleration towards the walls in order to balance the electron currents. Hence, the ion density is not modulated in time (see Fig. 4.1). The density of the ions decreases to the electrodes as in the dc sheath with finite density at the walls.

In contrast to the ions, electrons are able to follow the complete dynamics of the applied voltages according to  $\omega_{rf} \ll \omega_{pe}$ . Usually the drop in the potential of the sheaths near the electrodes shields electrons from the walls for most of the period of the rf (see Fig. 4.1). At maximum voltage electrons are able to reach the driven electrode (see Fig. 4.1e). At this moment the potential drop is diminished so far that electrons overcome the barrier. This guarantees the balance of electron and ion currents towards the walls. Like water surfing at the beach the electrons flood the sheath for a part of the rf cycle. It is even possible that the rf sheath becomes quasi-neutral, but not in the case considered here.

The dynamics of the electrons has direct influence on the plasma potential. The driving electrode lifts and lowers the potential within the cycle. The ground electrode sets the basis level of the potential. The inner region of the plasma is always positively charged resulting in a positive plasma potential. Electrons at all times are able to follow the rf completely, thus, no sheath reversal is observed, in contrast to e.g. hydrogen discharges [64, 65].

The upper, grounded electrode reacts symmetrically but phase-shifted to the driven electrode. If electrons are pushed away from the driven electrode the sheath collapses at the upper one and vice versa. The entity of electrons is sloshing in the plasma from one electrode to the other. Thus, the dynamics of both sheaths are shifted in time by half the period of the rf cycle. This is seen in the electron distribution functions (see Fig. 4.2).

The expanding sheath leads to an increase of high energy electrons (see Fig. 4.2). Electrons are pushed away by the growing plasma potential. At intermediate pressures (a few tens of Pa) the randomization by collisions is very effective. Therefore, positive and negative axial speeds are increased at the same time. The oscillating sheath edge pushes few electrons back and forth, accelerating them like surfers on a wave. Thereafter, these electrons distribute their energy in successive elastic collisions with neutrals. This mechanism is called Ohmic heating, because of the nature of this randomization process.

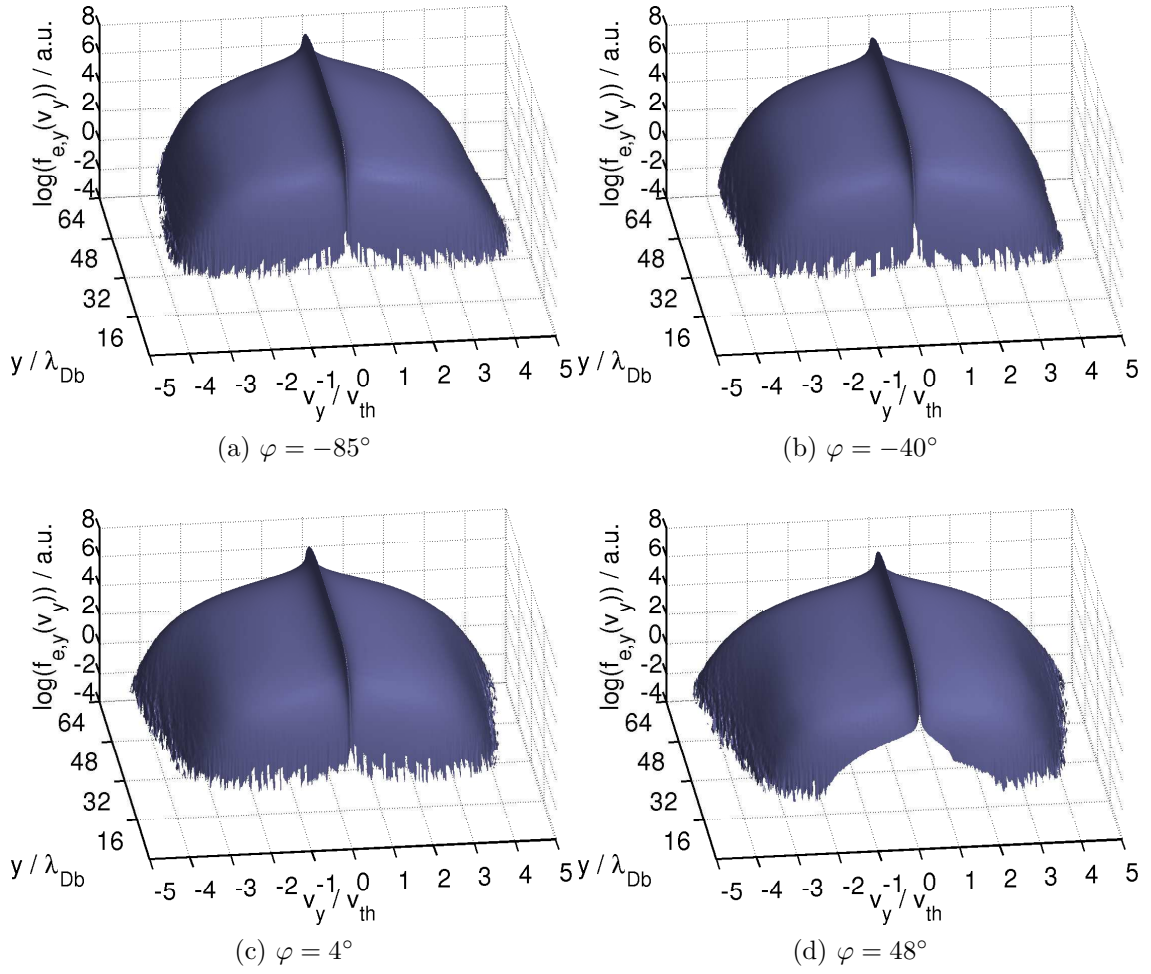


Figure 4.2: Phase resolved time-averaged distribution function of the axial component of the electron velocity (EVDF). The phases of the sinusoidal rf voltage are given.

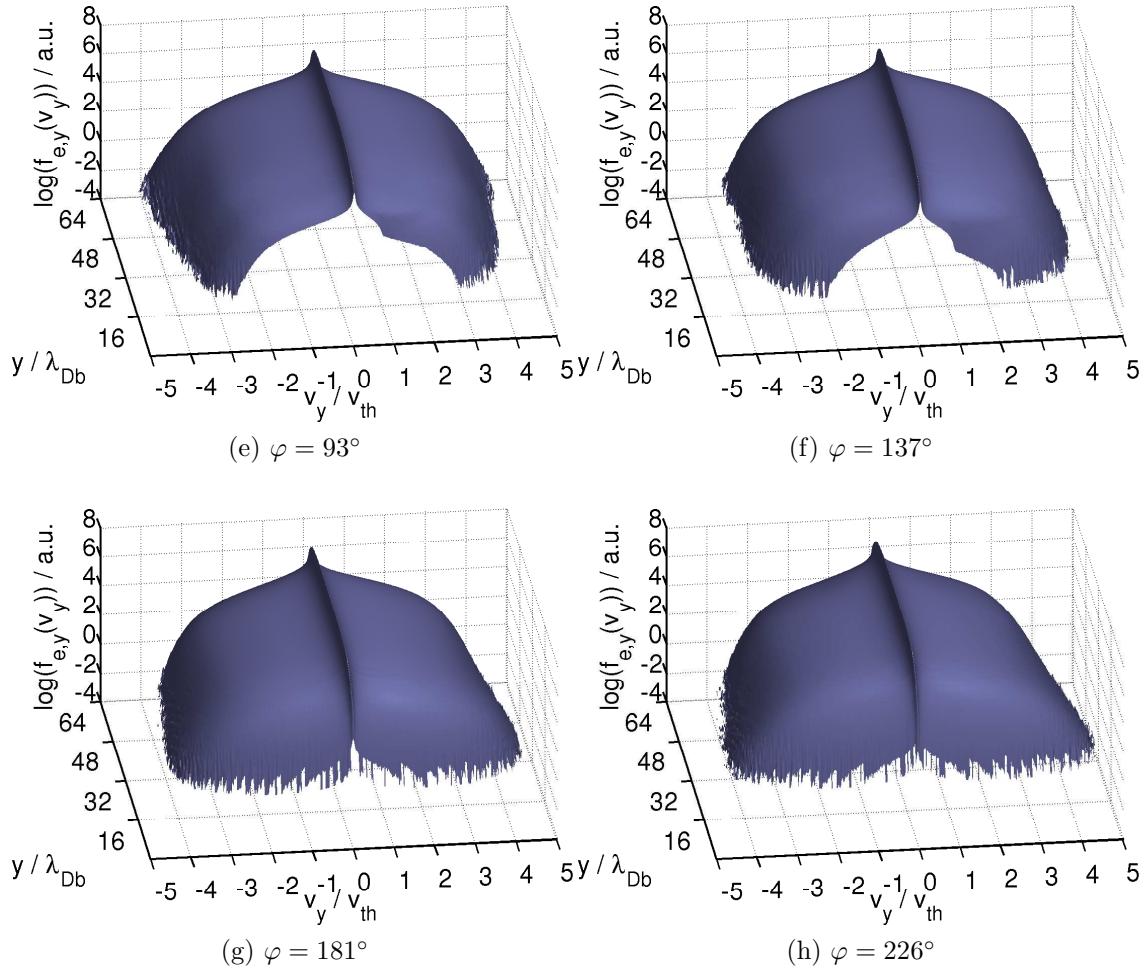


Figure 4.2: (continued)

### 4.1.1 Principle of the phase-resolved optical emission spectroscopy (PROES)

Atoms can be excited by collisions or radiation from a low energetic level like the ground states to higher energy bound states. In most cases, only a single-valence electron is excited. Most bound states can emit a photon and return to lower energy levels. Plasma itself emits a broad spectrum of spectral lines depending on the discharge and the kind of species used as the working gas.

It seems likely to deduce properties of the plasma from observation of radiation. One of the advantages of detecting the optical emission is that it is non-invasive. This even allows a direct measurement in the plasma sheath, where other diagnostic techniques have problems not to perturb the plasma.

Provided collisional excitation models exist, one gains information about the population density of excited states. This enables conclusions about particle densities and their energy distribution.

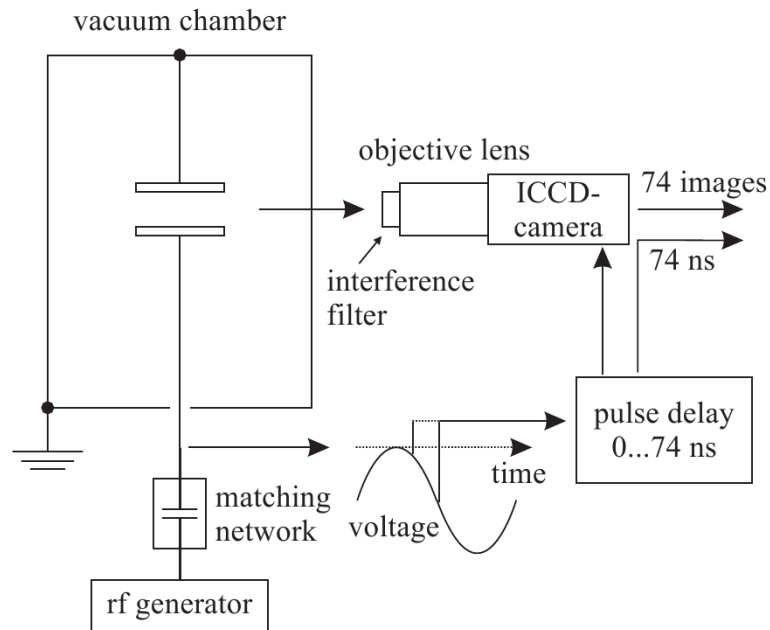


Figure 4.3: Scheme of the experimental set-up for PROES, taken from [66].

The principle of the phase-resolved optical emission spectroscopy (PROES) is the following: optical emission of the plasma is detected along the axial direction of the rf discharge with a fast, gateable intensified charge-coupled device (ICCD) camera. The gate of the ICCD-camera is triggered at a fixed phase of the rf. At

this phase the emission is recorded over many cycles. Then, the trigger point is shifted to different phases of the rf, which yields in a full spatio- and temporally-resolved measurement of the emission. By putting filters in front of the lens it is possible to measure the emission of separate lines. Figure 4.4 displays the result of such a measurement for an argon spectral line at  $750\text{ nm}$ .

If the detailed atomic transitions are known, it is possible to deduce the excitation rates of the spectroscopic transitions of the constituents of the plasma from the measured emission.

### 4.1.2 Excitation rates

In order to distinguish underlying excitation mechanisms the excitation rates  $X(z, t)$  need to be known in advance. The excitation can be calculated from the emission intensity  $I(t, z)$  by the following relation

$$X(z, t) \propto I(t, z) + \tau \frac{dI(t, z)}{dt}. \quad (4.1.2)$$

Here, the state of argon atoms is deduced from the emission. The finite lifetime  $\tau$  of the excited states has a broadening effect on the emission, compare Fig. 4.4a with 4.4b, yet, both plots show a pronounced peak structure modulated by the rf.

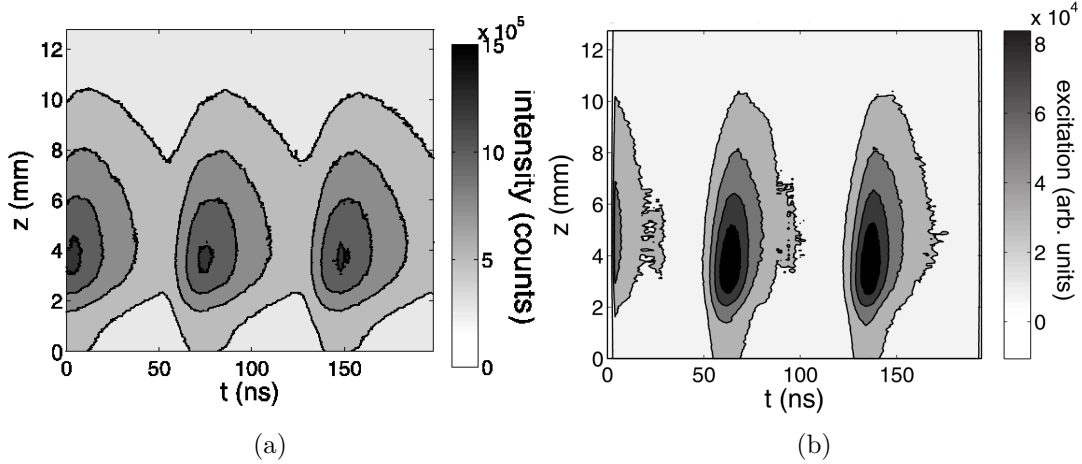


Figure 4.4: Averaged spatio-temporally resolved emission (Fig. 4.4a) and the corresponding excitation (Fig. 4.4b) of the  $750\text{ nm}$  spectral line in a rf argon discharge, taken from [57].

The dynamics of a CCRF argon discharge have been studied with PROES [57] at discharge parameters: 20 W rf power, pressure of 30 Pa and 200 V rf amplitude. The spatio-temporally resolved excitation rates have been calculated for several argon lines. The ground state of argon has an electron configuration of  $1s^2 2s^2 2p^6 3s^2 3p^6$ . The first lowest excited levels arise from the  $3p^5 4s$  configuration. In Paschen's notation they are labelled as the  $1s_2$  to  $1s_5$  levels. Next excited states arise in the p level, called  $2p_1$  to  $2p_{10}$ . Here, only some transitions between those states are of interest and stated in table 4.1.

wavelength / nm	transition	lifetime $\tau$ / ns	filter / nm
750.4	$2p_1 \rightarrow 1s_2$	22.5	$750 \pm 5$
840.8	$2p_3 \rightarrow 1s_2$	44.8	$840 \pm 5$
842.5	$2p_8 \rightarrow 1s_4$	46.5	$840 \pm 5$

Table 4.1: Investigated emissions in neutral argon (Ar I) with transitions, lifetimes and applied wavelength filters

The filters have an uncertainty of  $\pm 5$  nm. Due to this finite bandwidth the emission of line 840.8 nm and of line 842.5 nm is recorded simultaneously and cannot be distinguished, but this is not a drawback of the method. In a previous measurement by K. Dittmann [66] the spatio-temporal excitation patterns of several argon lines have shown a very similar structure. Therefore, it is reasonable to assume that both lines 840.8 nm and 842.5 nm have matching patterns of excitation. In the following, the transition  $2p_3 \rightarrow 1s_2$  corresponding to the line excitation of 840.8 nm will be discussed in detail.

### 4.1.3 Simulation of the spatio-temporally resolved excitation of argon

First, let us consider how the PIC-MCC model can simulate such spatio-temporally resolved excitations. The three-dimensional simulation already provides the spatial and time-resolved electron velocity distribution function. If the excitation cross-sections are known, one can calculate from the energetic state of the electrons the excitation rate  $R$  by the following equation

$$R = n_{Ar} \int_0^{5v_{th,e}} \sigma(E) f_e(v) v_{rel} 4\pi v^2 dv, \quad (4.1.3)$$

where  $n_{Ar}$  is the neutral density and assumed to be fixed. Because the electrons are much more mobile, the relative velocity  $v_{rel}$  between argon neutrals and electrons can be approximated by the electron velocity  $v_{rel} \approx v$ . It is assumed, that excitation of the  $2p_3$  argon state appears from ground state. A direct electron impact excitation cross-section  $\sigma(E)$  can be found in [67, 68], which crucially depends on the energy of the electrons. Although the mean temperature of the electrons is  $3.5 eV$ , highly energetic electrons are able to excite neutral argon atoms from ground state by inelastic collisions. This transition has a threshold energy  $E_{exc}$  of  $14 eV$  [68]. Another possibility for the population of the  $2p_3$  argon state is by excitation of higher excited levels and then cascading into it. In the following simulation only the direct excitation from ground state is considered for simplicity.

Metastable states play an important role as intermediate steps to excitation and ionization levels in CCRF plasmas. Only a few electron volts are necessary for excitation into higher energy levels or for ionization. For instance, the  $4s$  level ( $J = 0$ )  $1s_3$  and ( $J = 2$ )  $1s_5$  states are both metastable with energies of about  $11.6 eV$ . The  $4p$  levels have energies of about  $13.5 eV$  and the ionization energy of argon is  $15.8 eV$ . Therefore, excitation or ionization out of meta-stable states requires only  $2$  to  $4 eV$ . Although density of the metastable species might be low, the large density of electrons in the low energy range ( $2 - 4 eV$ ) and the larger cross-sections for excitation from metastable states, may contribute significantly to the overall excitation [69].

For the population of the states  $2p_8$  and  $2p_3$ , which have both a total angular momentum  $J = 2$ , only the metastable state  $1s_5$  with  $J = 2$  allows a transition by dipole excitation. The other metastable state  $1s_3$  has an angular momentum of  $J = 0$  and therefore breaks the transition rules  $\Delta J = 0, \pm 1, J = 0 \nrightarrow J = 0$ . The authors in [70] state that the ratio of metastable states  $1s_5$  and  $1s_3$  to the ground state is constant. Further, the energy threshold for meta-stables is low, of the order of the electron temperature. This means that the excitation according to this transition in a well thermalized plasma is unlikely to be modulated by the rf frequency in the plasma bulk. The resulting intensity of excitation of this process will possibly deliver a constant background in the centre of the discharge (see Fig. 4.5). This mechanism is questionable to produce such peak structures observed in figure 4.4. It is therefore reasonable to consider the excitation from the ground state in the following.

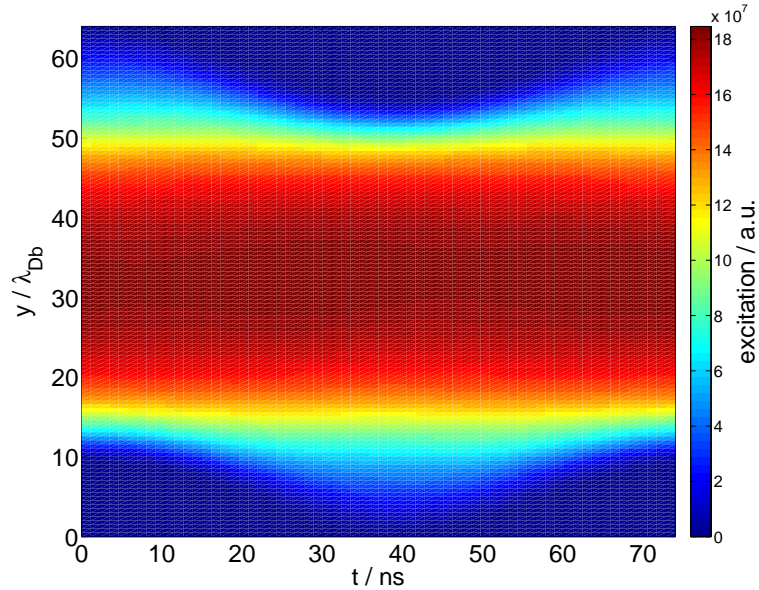


Figure 4.5: Simulated averaged spatio-temporally resolved excitation from metastable state  $1s_5$  to  $2p_3$  of argon.

#### 4.1.4 Comparison of measured and calculated time-resolved excitation rates

To interpret the mechanisms of excitation, the excitation patterns deduced from experiments will be presented along with the simulated excitation. In this way the simulation can provide further insight into the microscopic processes in such plasmas. For comparison the simulation was carried out with the same setting for the simulation of the argon plasma at a pressure of  $50 Pa$  with  $50 V$  amplitude of the sinusoidal voltage.

Both figures 4.6 have a clear dependence on the rf cycle. The excitation in the experiment has its maximum excitation  $4 mm$  above the electrode at the beginning of the expanding sheath. The peak structure is repeated every rf period of  $74 ns$ . Below the excitation pattern, the corresponding phase of the rf is indicated. Contrarily, two sheaths are displayed in the simulation leading to two peaks per cycle. The mirroring effect of the other electrode yields in a second peak congruent with the first one. The shape and spatial position of the calculated emission fit the experiment remarkably well. Only the maximum of the excitation appears later in the expanding phase of the rf sheath. The higher pressure in the simulation and the lower rf voltage may explain this. Electrons

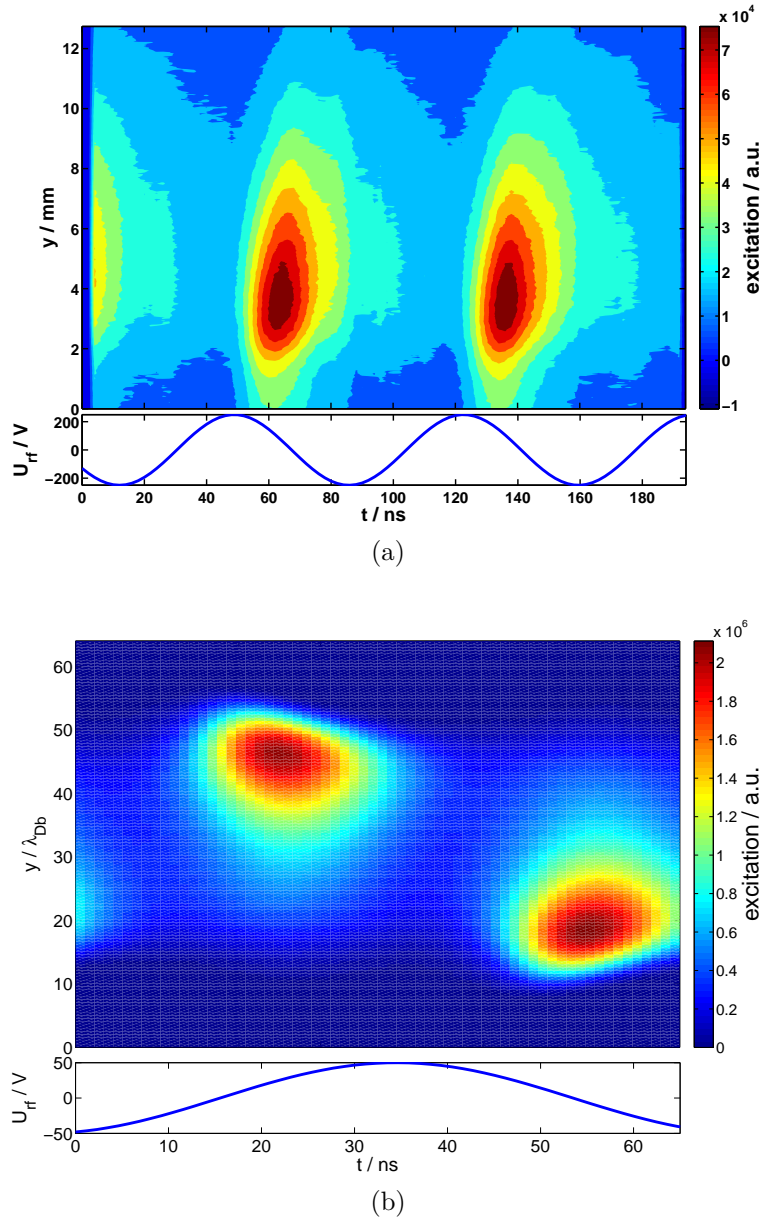


Figure 4.6: Averaged spatio-temporally resolved excitation of the  $840.8\text{ nm}$  spectral line of argon. Figure 4.6a shows the excitation deduced from the measured emission of [57]. The measurements were performed in a rf argon discharge at  $13.56\text{ MHz}$  with  $20\text{ W}$  rf power, an amplitude of  $250\text{ V}$  and a gas pressure of  $30\text{ Pa}$ . In figure 4.6b the simulated averaged spatio-temporally resolved excitation from ground state to  $2p_3$  of argon is shown.

are accelerated less and collisions are more frequent. Hence, it takes longer for the electrons to gain energy, so that the peak in excitation occurs later. The initial phase seen in figure 4.6b is used in all other subsequent simulations, if not stated otherwise.

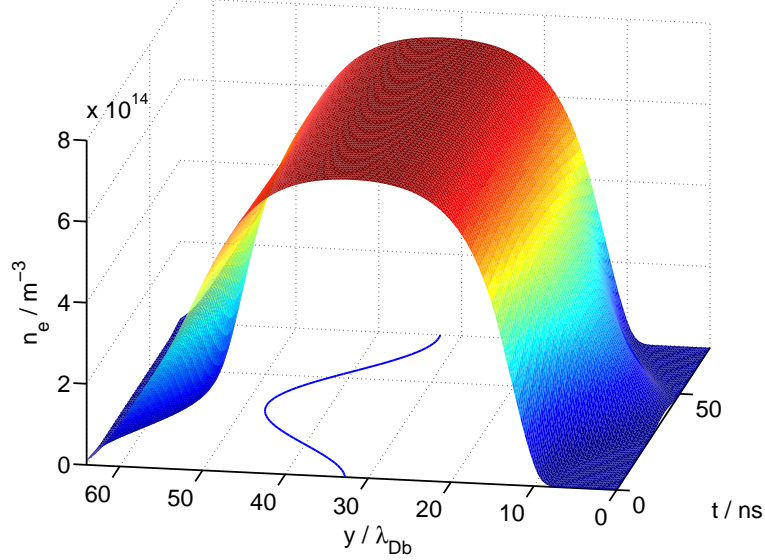


Figure 4.7: Averaged spatio-temporal electron density distribution computed by the  $P^3M$  model. The electrons can respond to the quickly varying electric field. For a short time-interval electrons overcome the sheath barrier.

Different excitation structures were attributed to various underlying excitation mechanisms. Various structures with different excitation mechanism have been observed experimentally [66]. Here, only one excitation structure occurs during the sheath expansion. Electrons are accelerated by the growing sheath towards the plasma bulk. Some electrons gain so much energy that they could excite argon neutrals by electron impact. This is the structure seen in the experiment of Melzer [57] as well as in the corresponding simulation. Since the mean free path  $\lambda_{e-n} \sim 830 \mu m$  for such process is smaller than than the system length  $L = 2.4 cm$ , which restricts the excitation pattern close to the sheath. The additional energy from the sheath modulation can be seen in the rf-resolved temperature of the electrons. The spatial and temporal pattern of the thermal energy in figure 4.8 matches with the excitation in figure 4.6b. Density fluctuations do not contribute to the pattern. The density in the centre of the plasma is steady (see Fig. 4.7).

The simulation matches the results of the experiment very well. Spatial and temporal behaviour of the excitation indicate that the structure is caused by

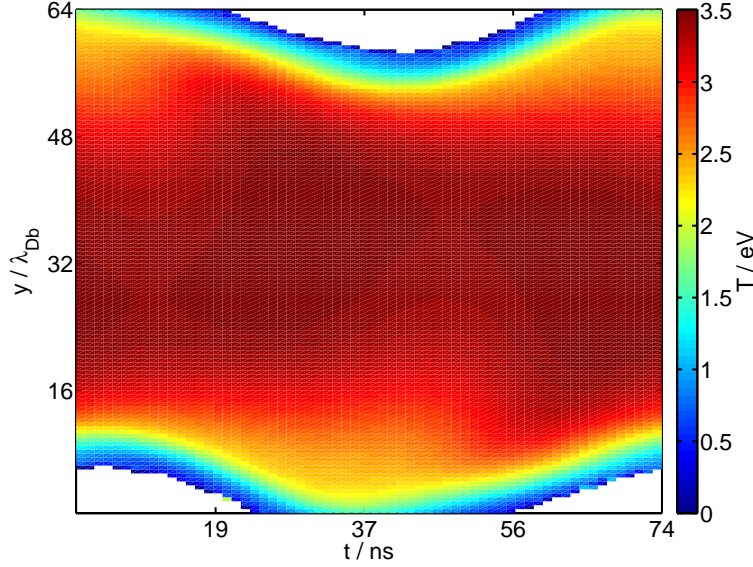


Figure 4.8: Averaged spatio-temporally resolved electron temperature.

electrons accelerated in the expanding sheath. Now, we will investigate discharge dynamics with a dust particle immersed in the plasma and its influence on charging rf resolved.

## 4.2 Time-resolved effects of dust particles in CCRF plasmas

In this section, the temporal behaviour of the charging of a dust particle in the rf cycle is resolved. Although the computation has been distributed on 8 cores at 2.4 GHz of a Linux cluster, the total computing time was about five days. For statistical reasons and restrictions on the computing time, the spatial and temporal averages of physical quantities are now taken from 6000 rf cycles, which corresponds to a total averaging time  $T_{aver} = 442.5 \mu s$ . The time for a single electron step on the PIC scale  $\Delta t = 0.2(\omega_{pe})^{-1} = 1.12 \cdot 10^{-10} s$  is much smaller. The  $P^3M$  method slows down the computation of the plasma relative to plain PIC modelling. The enhanced spatial resolution as well as the sub-cycling within the MD volume increase the workload. In total 3,936,000 complete PIC cycles with MD sub-cycling have been computed. Only carrying out this calculation lasted nearly three days.

### 4.2.1 Fluctuations of the charge during the rf cycle

It was possible to resolve the dynamics of the currents to the dust during the rf cycle. One would expect that with the sloshing electrons the particle charge might vary within one rf cycle. Because of the enormous random fluctuations, seen in section 3.2.3, the behaviour was investigated by the averaged phase-resolved values.

In the simulation the dust particle is pinned to a fixed location. This is generally a reasonable assumption. The thermal velocity scales with the inverse of the square of the mass. Since the dust mass is orders of magnitude larger than the mass of the ions, typically  $10^{10} - 10^{16}$ , the motion is heavily damped. The maximal speed is of order millimetres per second, so that the motion of dust occurs on much larger time scales. For the charging processes in the plasma the motion of the dust grain is negligible.

The influence of two different plasma conditions are shown in figure 4.9. The middle plot shows the fluxes to the dust according to the plasma environment described in the previous sections. For the bottom plot the discharge parameters are same, but the collisionality is artificially diminished. The ratio of the net change to the dust charge  $\Delta Q/Q_{dust}$  is at maximum  $4 \cdot 10^{-4}$ . Here, the particle charge is of the order of  $10^4$ , i.e. the deviation is just a few elementary charges on average. As seen in Fig. 4.9 the fluxes and thus the change in the charge over the rf cycle is nearly negligible. Due to their huge inertia the ion fluxes are constant during the whole cycle, whereas the electrons are modulated by the rf. This is valid for both plasma environments. The bottom plot has a decreased collisionality. Therefore, the average sheath width is larger. As a result, the dust particle is, although at the same spot, deeper in the sheath and the electron flux varies more strongly. The electron fluxes have two noticeable maxima. In the expansion phase the sheath is completely depleted and thus no electron flux to the dust is observed. With decreasing sheath the electrons enter the sheath, which corresponds to the first peak in the electron flux. Later, when the sheath is already building up a next wave of electrons charges the dust. The directed flow of electrons is represented in the microscopic charging dynamics. Due to the potential build-up electrons gain energy to overcome the dust potential on average.

For this artificial surrounding the gravitational force might not be compensated by the electric field. It has been found that dust particles are captured by parabolic potentials [71]. If the particle deviates from equilibrium position the total force consisting of electric and gravitational force will usually restore equilibrium. The equilibrium position corresponds to the second case, reflecting plasma conditions of the experiment [57]. With these settings the dust particle is at all times surrounded by electrons (see Fig. 4.9). In general the fluxes are

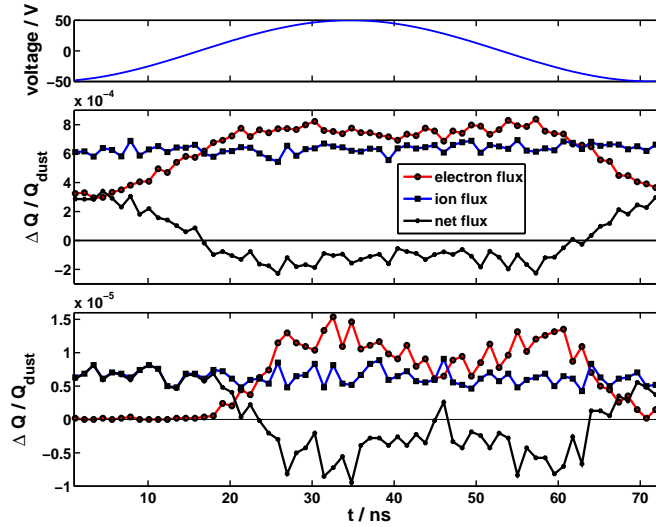


Figure 4.9: Simulated temporal resolved fluxes to a dust particle at a fixed position (averaged over 6000 rf cycles) for different plasma conditions. The plot at the top displays the rf phase. The middle plot shows the fluxes to the dust according to the plasma environment described in the previous sections. For the bottom plot the discharge parameters are the same, but the collisionality is artificially diminished.

increased to the former state. Electrons are still modulated, but the peak structure is strongly reduced.

The total charge oscillates with a very small amplitude with rf frequency. From OML theory T. Nitter derived already such a behaviour of the charging [72]. That also means that the average floating potential is nearly constant within the rf cycle. The exact shape of the plasma and dust potential deviation during the rf period can be neglected. Instead, the random variations from the mean charge dominate by far the behaviour. The discreteness of the particles is more important to the charge and consequently to the potential than the rf modulation itself. Nevertheless, the effect of discontinuity is overrated by the super-particle approximation in the  $P^3M$  model presented.

## 4.2.2 Influence of the dust on the CCRF plasma

Melzer et al. were able to resolve the spatial and temporal behaviour of the excitation in CCRF discharges with and without dust [57] by PROES. Figure 4.10 shows the resulting excitation patterns of the discharge with as well as without dust and their difference. In essence, Melzer et al. witnessed for several

argon lines, that the intensity of each argon line is larger, if small dust particles are added to the discharge.

To elucidate the origin of the increase in excitation corresponding simulations with dust particles have been performed. With and without dust, in figure 4.11 two maxima in the excitation are observable. The symmetry in the excitation implies that each peak is caused by one of the sheaths, separately. The lower maxima results from the sheath expansion including the dust particle, whereas the sheath at the grounded electrode has no dust particle. Figure 4.11c shows explicitly the influence of the dust. While the excitation at the sheath edge belonging to the lower sheath with the dust grain is enhanced, there is no mirrored structure in the difference in figure 4.11c. The differences in excitation are thus clearly attributed to the dust influence.

The strength of the difference in the simulation is about a factor of ten smaller than in the experiment. This might be due to the fact, that in the experiment emission of many dust particles in an optical thin plasma was recorded, yielding a larger excitation.

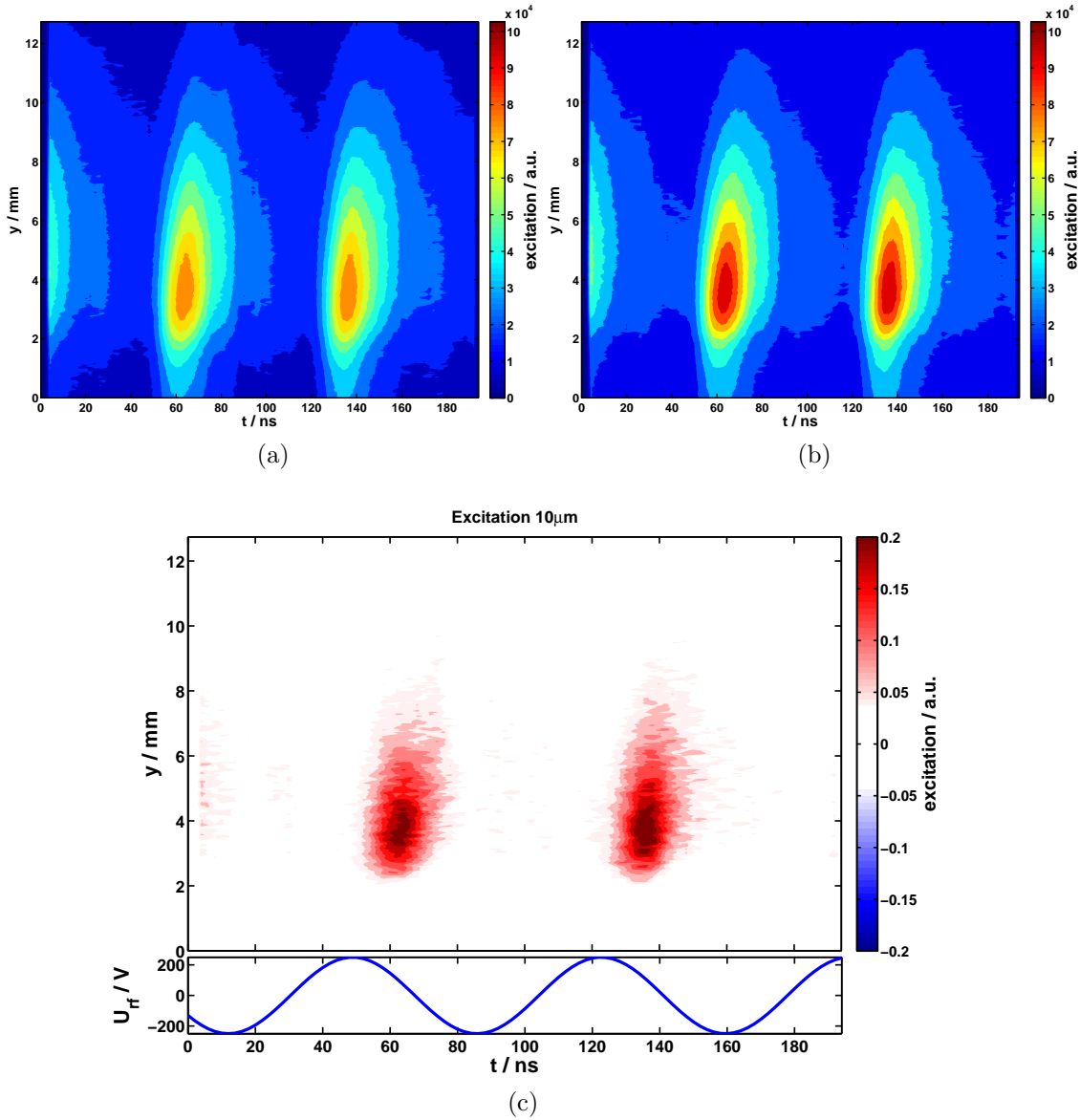


Figure 4.10: Spatio-temporally resolved excitation determined from experimental data of the  $840.8\text{ nm}$  spectral line of argon [57]. From top to bottom at first the reference excitation without dust (a), then the excitation with dust (b) and finally the difference in excitation (c) is shown. The difference is calculated by subtracting from the pattern with dust the excitation without dust and normalizing to the reference. The measurements were performed in a rf argon discharge at  $13.56\text{ MHz}$ , at  $20\text{ W}$  rf power with an amplitude of  $250\text{ V}$  and a gas pressure of  $30\text{ Pa}$ . The dust position is approximately at a height of  $2\text{ mm}$ .

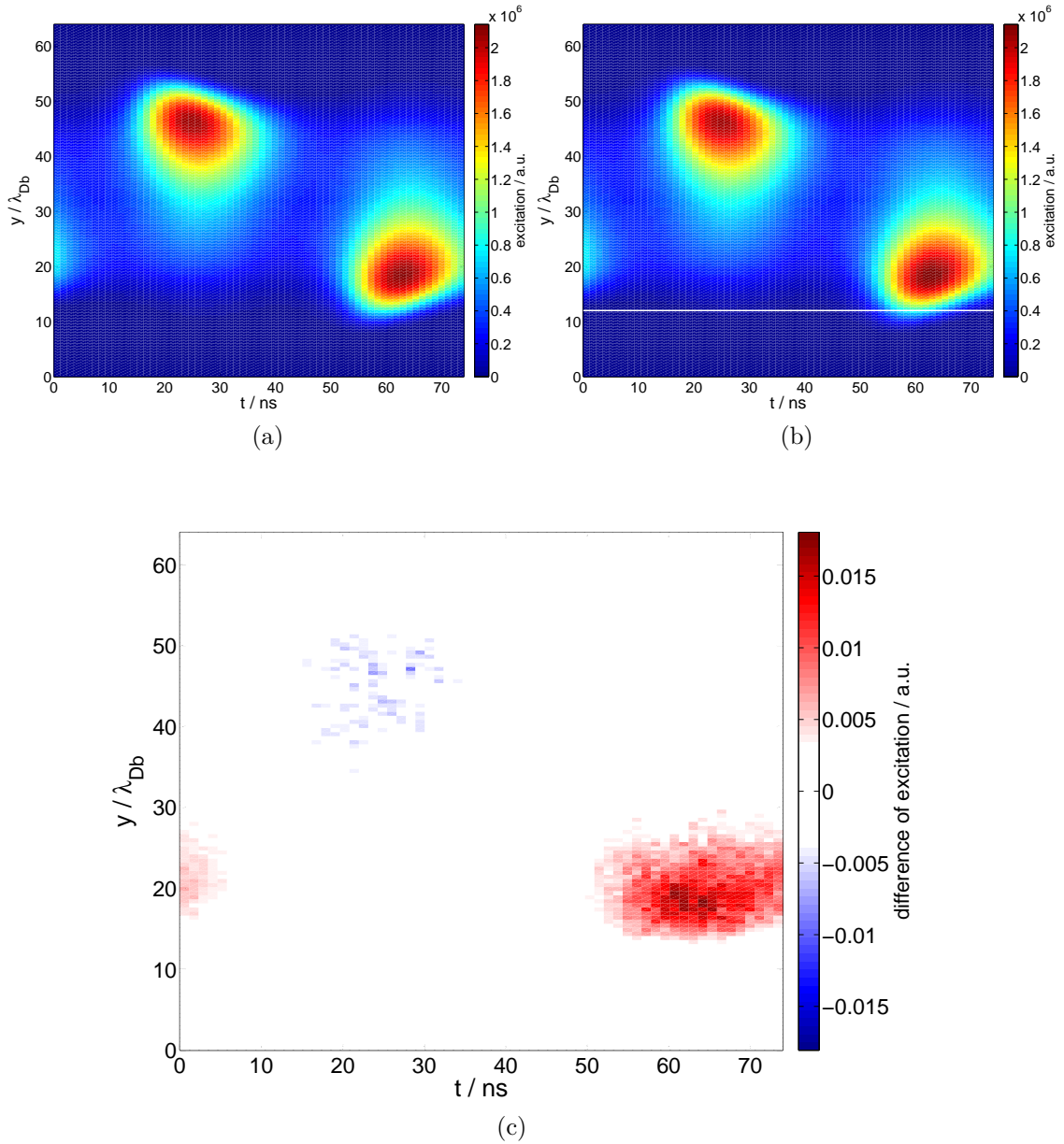


Figure 4.11: Averaged spatio-temporally resolved excitation of the 840.8 nm spectral line of argon from the simulation. From top to bottom the figure displays the reference excitation without dust (a), then the excitation with dust (b) and finally the difference in excitation (c). The difference is calculated by subtracting from the pattern with dust the excitation without dust and normalizing to the reference. The simulation was carried out at the afore mentioned parameters:  $p = 50 \text{ Pa}$ ,  $U_{rf} = 50 \text{ V}$ . The white line in 4.11b indicates the position of the dust grain.

The axial extension of the excitation difference suggests a supplementary production of high energy electrons in the sheath. The figures 4.12 and 4.13 present the density and temperature differences, respectively. The plots show patterns discriminated by certain minimal particle energies. Only particles with a higher energy than energy threshold are accounted for the total density. The excitation pattern is more reflected in the density, if the minimal threshold energy is higher. The differences in density in figure 4.12e for minimal energies of  $15.5\text{ eV}$  are in very good agreement with the excitation pattern. This is a temperature effect and thus can be seen in the temperature as well. Due to the noise in the temperature difference, especially at the border of the defined temperature region, the colour range has been cropped.

Seen in figure 4.14 is the integral density difference of electrons depending on their kinetic energy. The difference between the density with dust and without dust is normalized to the maximal density without dust as a reference. Generally, the effect of the dust on the density in this area is little  $\sim 10^{-3}$  relative to the overall density. However, during the rf the density of particles up to  $4\text{ eV}$  and from  $8\text{ eV}$  to  $12\text{ eV}$  is generally elevated. An expected effect happens in between. During the collapsing phase of the sheath (see Fig. 4.14a to 4.14c) when the dust particle is flooded by electrons the density of particles of about  $5\text{ eV}$  is diminished. Electrons with such energies overcome the potential of the dust particle ( $3.1\text{ eV}$ ) and are captured. The dust particle acts like a filter for the random motion with such energies. This is why the density for such energies is decreased in the bulk. Simultaneously, during the expansion phase the density of electrons with energies above  $8\text{ eV}$  is enhanced. On average this modulation in the densities seems to cancel out, since no difference in excitation via the metastable channel is seen in the computed excitation difference (see Fig. 4.15).

Except a small rf variation the excitation pattern in the bulk is nearly constant. This might support the structure of the difference in excitation, but does not seem to be the main reason. Apparent is the decrease of excitation around the dust particle position due to the depletion of electrons, but this structure is not observed in such manner in the experiment. Particles with energies about  $2$  to  $4\text{ eV}$  have an increased relative density, which is the energy already sufficient for excitation by metastables. Those particles are more frequent anyway, so that they determine this excitation channel. Again, this supports the idea that the modulation in excitation between a discharge with and without dust is generated by high energetic electrons.

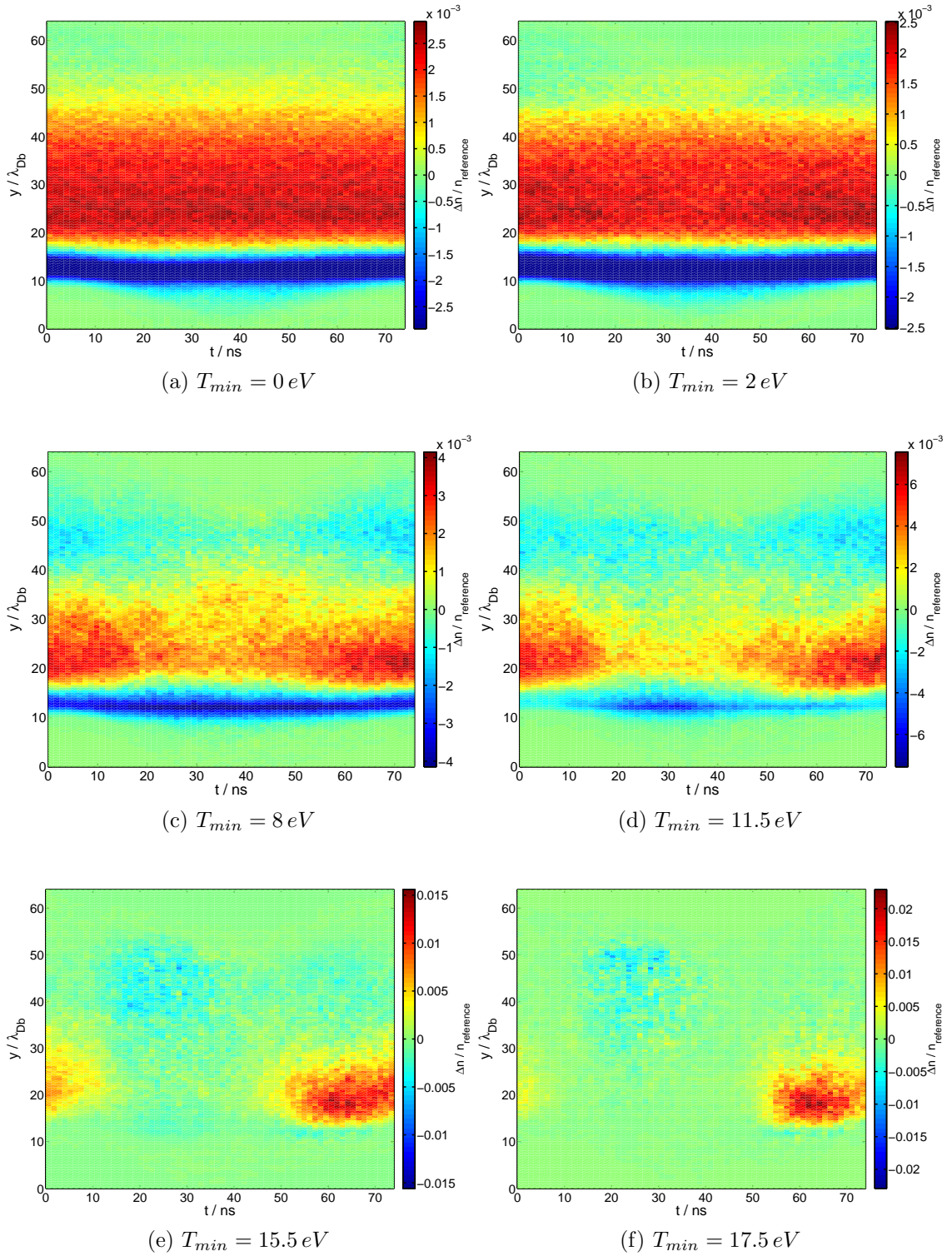


Figure 4.12: Phase resolved time-averaged difference in electron density. Only particles with a higher energy than the indicated energy threshold are accounted for the density.

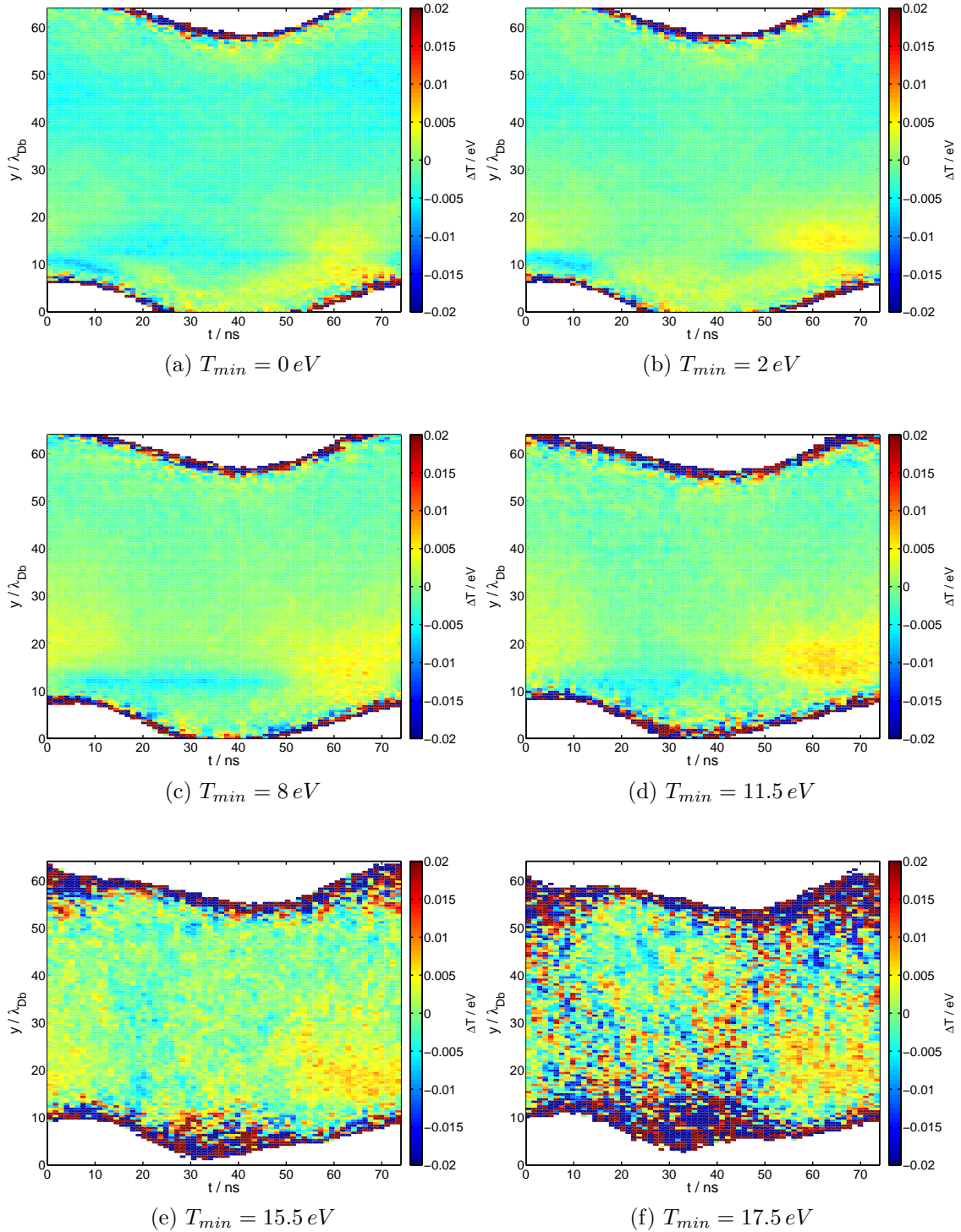


Figure 4.13: Phase resolved time-averaged difference in electron temperature. Only particles with a higher energy than the indicated energy threshold are accounted for the density.

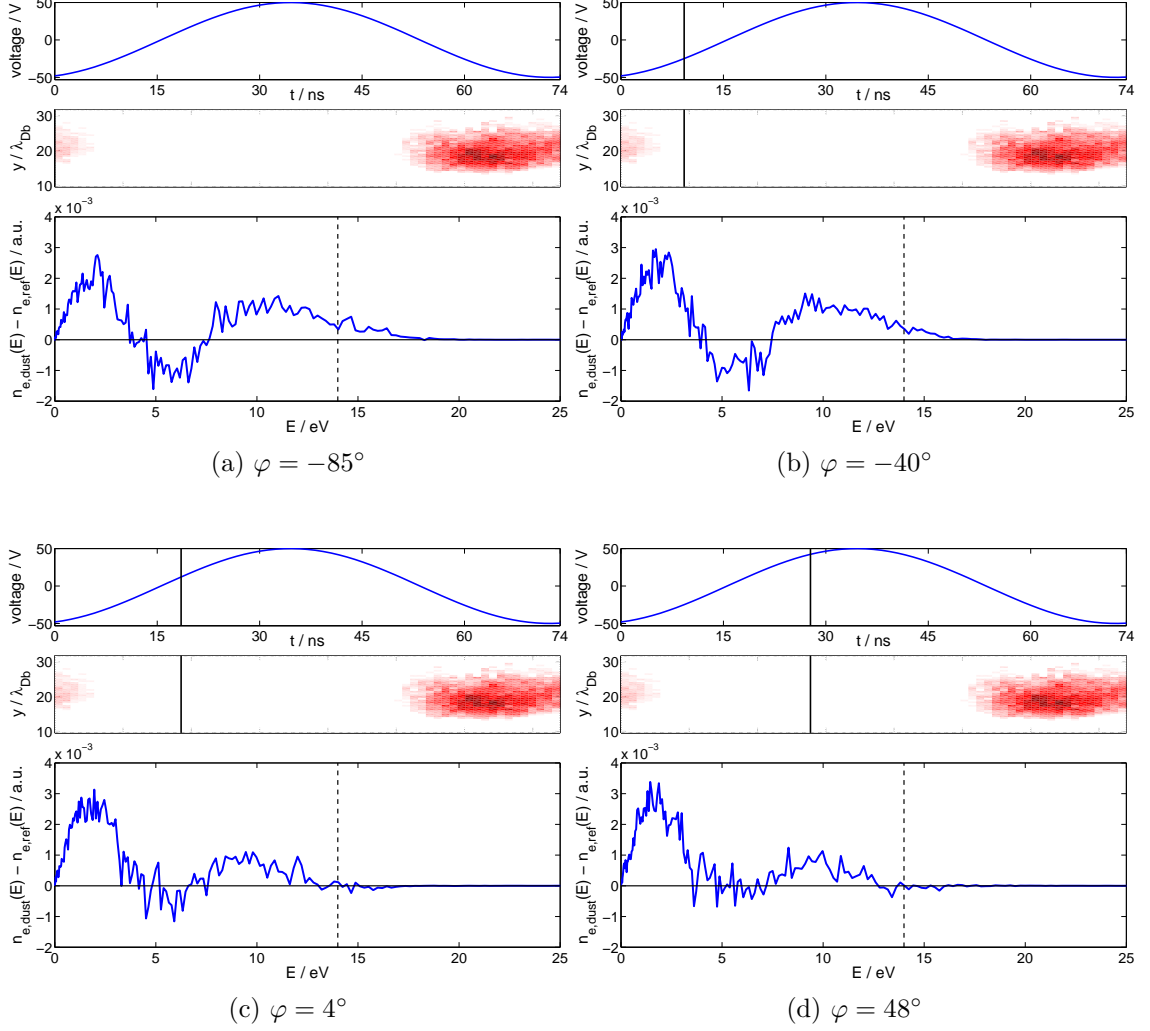


Figure 4.14: Difference in the phase resolved time-averaged normalized electron density between the discharge with and without dust plotted against the total kinetic energy. The top plot shows the phase and the middle plot the difference in excitation. The black vertical line in these plots indicates the phase of the rf cycle. At the bottom the density difference is plotted against the energy of the particles. For convenience, the density is taken over the whole axial extent of the difference in excitation. Indicated by the dashed vertical line is the energy threshold for excitation from ground state. The phase of the sinusoidal rf voltage is varied from  $\varphi = -85^\circ$  to  $\varphi = 226^\circ$ .

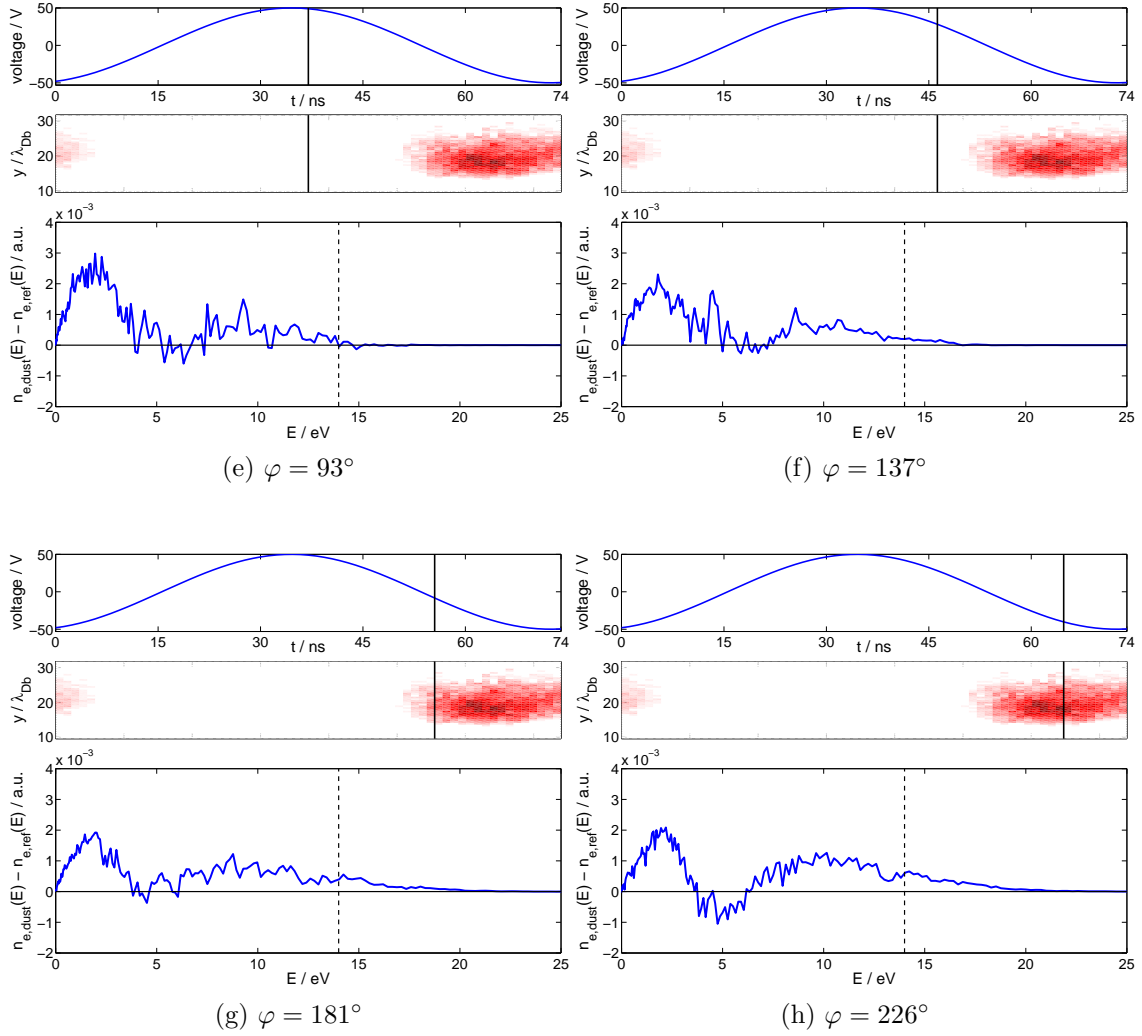


Figure 4.14: (continued)

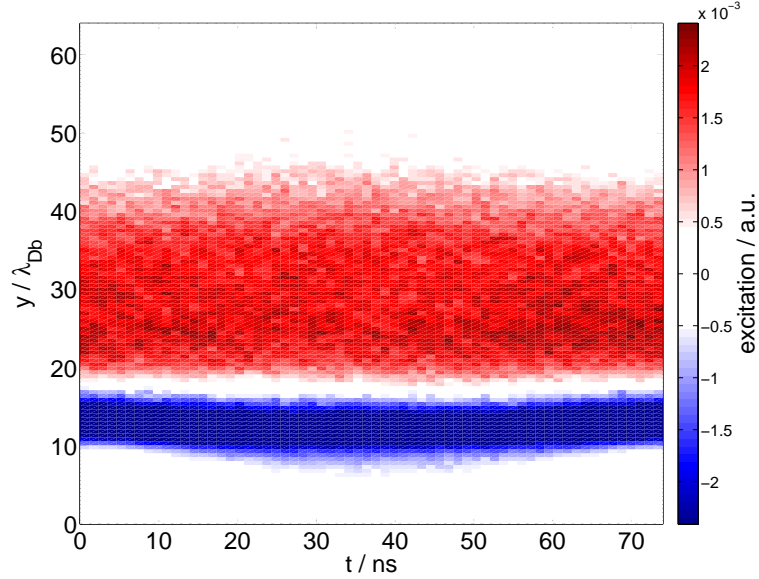


Figure 4.15: Difference of the simulated averaged spatio-temporally resolved excitation for the case with and without dust from metastable state  $1s_5$  to  $2p_3$  of argon.

During the expansion phase the density of electrons with energies above  $8 eV$  is enhanced, if a dust particle is immersed. At the dashed line, which indicates the threshold energy for the excitation from ground state to the excited state  $2p_3$ , the graph shows an increase of particles with high kinetic energies, when the difference in excitation occurs. This increased number relates directly to higher excitation. Not only the transition from ground state to the  $2p_3$  argon state is then responsible for the population of that state, but higher levels as well. More highly energetic states appear this way, which might cascade down to  $2p_3$  level. By this means, the excitation with dust is enhanced, when the sheath is expanding. Fig. 4.16 shows the influence of two different plasma conditions. At the top, the plot shows the phase of the rf. The middle plot shows the difference in excitation with the plasma environment described in the previous sections. For the bottom plot the discharge parameters are same, but the collisionality is artificially decreased. The pattern with collisions correctly taken into account appears a little bit closer to the dust location in space and slightly earlier in time compared to the artificial case. Electron-neutral collisions have the shortest mean free path of about  $10 cm$ , but are neglected in the second case. The lack of collisionality increases the motion of electrons and thus the average sheath width. For the same location the dust particle is deeper in the sheath for the artificial case. Less electrons are available for the difference in excitation. This is why the structure in the difference of excitation appears farther to the dust as

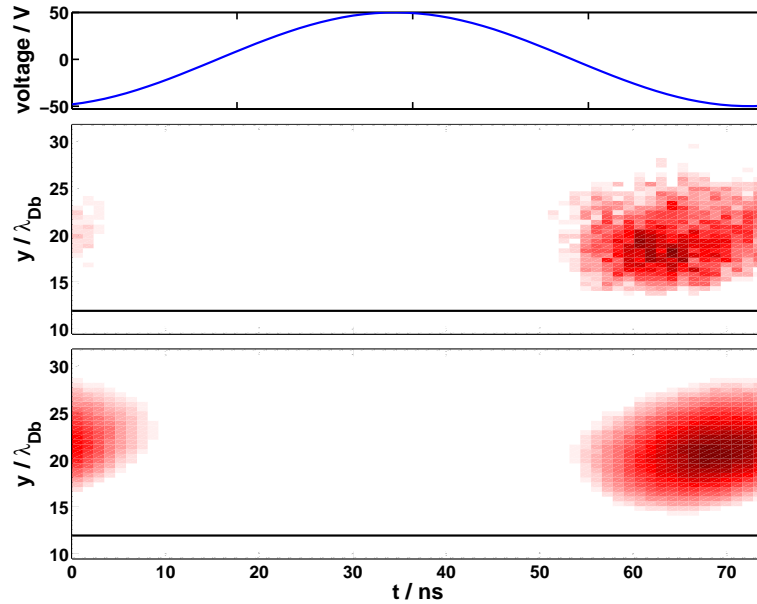


Figure 4.16: Simulation of the differences of the spatio-temporal excitation patterns for two individual cases.

well as later in time. The plasma potential needs to be larger for the on average slightly more distant electrons.

The influence of the dust leads to an increase in highly energetic electrons in the sheath expansion phase of the rf. To some extent the electrons fleeing from the growing plasma potential must be held back by the potential well formed between electrode and dust grain. As the sheath electric field is getting stronger, electrons are released. This way, few electrons should populate higher energies and therefore result in the difference of the excitation.

The  $P^3M$  model has shown remarkable agreement with experimental data. Moreover, it delivers the diagnostic techniques to access the underlying basic physics on a micro scale in time and volume. This way, it was possible to find a likely explanation for the mechanism of the difference in excitation, if dust particles are immersed in CCRF plasmas.

### 4.3 Synopsis

The full rf dynamics of a dusty CCRF discharge has been resolved. The effects of particle charging and the change in the plasma dynamics within the rf are accessible with  $P^3M$  model. While ions are too sluggish to follow the rf modulated electric fields, electrons can react to the rf dynamics. Usually, electrons are repelled from the sheath. Only for a small time interval electrons flood the sheath and balance the fluxes to the walls. But this modulation of the electron flow has shown very little variation on the dust charge during the rf cycle. Dust and correspondingly floating potential of the dust are on average nearly constant within the rf. Random fluctuations are by far more important.

With the phase-resolved optical emission spectroscopy the spatio-temporal dynamical behaviour of plasmas can be measured. The excitation patterns of the simulation resemble the results obtained in the experiments. This excitation pattern can be attributed to electrons accelerated in the expanding sheath. The effects of a dust particle on the plasma excitation and particle charging was resolved dynamically. The simulation has shown a modulation of the dust charge during the rf cycle negligible compared to its overall charge. That determines the floating potential of the dust as well. While the rf rises and lowers the plasma potential corresponding to the driven electrode the depth of the dust potential is constant with respect to the plasma.

Experiments have shown that if a small dust particle is immersed in the plasma the excitation rate is increased. This higher order effect has been reproduced with the  $P^3M$  simulation as well. The excitation patterns with and without dust show notable differences. The simulation suggest that this is caused by high energy electrons, which excite from ground state instead of intermediate metastable states. A possible explanation might be the potential well between electrode and dust grain. The dust potential holds back electrons, when the sheath is expanding. Electrons can then be released at higher voltages, so that the acceleration is enhanced. As a result, electrons are populated at higher energies. The variation of excitation by metastables seems to be suppressed by the dust itself.



## 5 Conclusions

In this work dust particles immersed in plasmas have been studied. Transport processes in plasmas depend on the charge of dust particles and on their structure formation. Dust particles usually acquire a large negative charge, so that electrostatic repulsion plays an important role in the formation of dust structures. To understand the charging of dust in detail this thesis deals with the simulation of the microscopic interaction of dust with plasma particles.

In order to study the formation of dust structures for spherical and non-spherical particles a particle-particle method was developed and validated with spherical particles forming Coulomb balls. A viscosity term was added in order to achieve equilibrium configurations. To analyze the potential energy surface starting from these configurations random displacements of the particles were done. From these random configurations the configurations with minimal energies were restarted with the particle-particle model. The simulations for non-spherical particles (barbells) have shown multiple stable minima of the potential energy surface, whereas spherical particles were characterized by a single minimum. This more complex structure for non-spherical particles is still simpler than structures in biological systems, where a huge number of local minima in the potential energy surface as well as helical structures exist. This is explained by the fact that in the systems studied in this work only repulsive forces between particles have been considered. However, biological systems are characterized by both attractive and repulsive forces allowing also helical structures, not observed for dust.

To resolve the charging of dust particles in capacitively coupled radio frequency (CCRF) plasmas including finite-size effects of dust grains an extension of the Particle-in-Cell method was needed to allow a realistic description of the interaction of dust with plasma. A particle-particle particle-mesh ( $P^3M$ ) model was applied, where in a region close to the dust a molecular dynamics (MD) algorithm is used to calculate the close-range forces between dust and plasma particles. The CCRF plasmas used for dust experiments are operating in an intermediate collisionality regime. Inelastic collisions yielded in a Druyvesteyn-like electron energy distribution function. The charging of a single non-emitting dust grain in the sheath of a CCRF discharge was studied. Deviations for the charge and floating potential predictions from orbital motion limit (OML) theory were observed. The temporal behaviour of the charging, namely charging time and

fluctuations, are within theoretical expectations. Secondary electron emission from the dust surface was modelled by implementing a Monte Carlo algorithm into the  $P^3M$  code. With increasing emission the equilibrium of the total flux is changed: the higher the secondary electron emission yield the lower the average charge. The double sheath predicted by theory for a planar geometry has not been found in front of dust particles for values of the secondary electron emission yield up to one.

The full rf dynamics of a dusty CCRF discharge has been resolved. The effects of particle charging and the change in the plasma dynamics within the rf are accessible with the  $P^3M$  model. While ions are too sluggish to follow the rf modulated electric fields, electrons can react to the rf dynamics. Usually, electrons are repelled from the sheath. Only for a small time interval electrons flood the sheath and balance the fluxes to the walls. But this modulation of the electron flow has shown very little variation on the dust charge during the rf cycle. Dust and correspondingly floating potential of the dust are on average nearly constant within the rf cycle. Random fluctuations are by far more important.

With the phase-resolved optical emission spectroscopy the spatio-temporal dynamical behaviour of plasmas can be measured. The excitation patterns of the simulation resemble the results obtained in the experiments. These excitation pattern can be attributed to electrons accelerated in the expanding sheath. The effects of a dust particle on the plasma excitation and particle charging was resolved dynamically. The simulation has shown a modulation of the dust charge during the rf cycle negligible compared to its overall charge. That determines the floating potential of the dust as well. While the rf cycle rises and lowers the plasma potential corresponding to the driven electrode the depth of the dust potential is constant with respect to the plasma.

Experiments have shown that if a small dust particle is immersed in the plasma the excitation rate is increased. This higher order effect has been reproduced with the  $P^3M$  simulation as well. The excitation patterns with and without dust show notable differences. The simulation suggests that this is caused by high energy electrons, which excite from ground state instead of intermediate metastable states. A possible explanation might be the potential well between electrode and dust grain. The dust potential holds back electrons, when the sheath is expanding. Electrons can be released at higher voltages, so that the acceleration is enhanced. As a result, electrons are populated at higher energies. The variation of excitation by metastables seems to be suppressed by the dust itself.

Simulations presented in this work have proven that computational physics has established as a third major research direction mediating between experiment and theory. Comparison of simulations with experiments enables an improved microscopic understanding of the physics in dusty plasmas.

# A Appendix

## A.1 Dimensionless variables

$\Delta x$       mesh width  
 $\Delta t$       time step  
 $N_e, N_i$     number of electrons and ions per PIC cell, respectively  
 $N_0$       initial number of particles per PIC cell

$$\frac{\Delta x}{\lambda_D} \stackrel{!}{=} \widetilde{\Delta x} \stackrel{!}{=} 0.5 \quad \Leftrightarrow \quad \widetilde{x} = \frac{x}{\Delta x}$$

$$\Delta t \cdot \omega_p \stackrel{!}{=} \widetilde{\Delta t} \stackrel{!}{=} 0.2 \quad \Leftrightarrow \quad \widetilde{t} = \frac{t}{\Delta t}$$

$$\widetilde{m}_e \stackrel{!}{=} 1$$

---

$$\begin{aligned} \dot{x} = v & \quad \hat{=} \quad v_t = \frac{x_{t+\Delta t} - x_t}{\Delta t} \\ & \quad \Leftrightarrow \quad \widetilde{v} = \frac{\Delta t}{\Delta x} \frac{\widetilde{x}_{t+\Delta t} - \widetilde{x}_t}{\widetilde{\Delta t}} \end{aligned}$$

$$\Downarrow \quad \Leftrightarrow \quad \widetilde{v} = v / \frac{\Delta x}{\Delta t}$$

$$\widetilde{\dot{x}} = \widetilde{v}$$

---

$$\dot{v} = \frac{q}{m} E \quad \Leftrightarrow \quad \dot{\widetilde{v}} = \dot{v} \frac{(\Delta t)^2}{\Delta x} = \frac{q}{m} \frac{(\Delta t)^2}{\Delta x} E$$

$$\Downarrow \quad \Rightarrow \quad \widetilde{E} = \frac{1}{2} \cdot \frac{q}{m} \frac{(\Delta t)^2}{\Delta x} E$$

$$\dot{\widetilde{v}} \stackrel{!}{=} 2\widetilde{E}$$

---

$$\begin{aligned}
E = -\nabla\Phi &\hat{=} E_i = -\frac{\Phi_{i+1} - \Phi_{i-1}}{2\Delta x} \\
&\Leftrightarrow \Delta\Phi_i = \Phi_{i+1} - \Phi_{i-1} = -2E_i\Delta x \\
&\Rightarrow \tilde{\Phi} = \frac{\Delta t^2}{\Delta x^2} \frac{q}{m} \Phi
\end{aligned}$$


---

$$\begin{aligned}
\nabla^2\Phi = -\frac{\rho}{\epsilon_0} &= -\frac{q}{\epsilon_0}(n_i - n_e) = -\frac{qn_0}{\epsilon_0} \frac{n_i - n_e}{n_0} \\
&\Leftrightarrow \frac{\Phi_{i+1} - 2\Phi_i + \Phi_{i-1}}{\Delta x^2} = -\frac{qn_0}{\epsilon_0} \frac{N_i - N_e}{N_0} \\
&\Leftrightarrow \underbrace{\tilde{\Phi}_{i+1} - 2\tilde{\Phi}_i + \tilde{\Phi}_{i-1}}_{=\widetilde{\Delta\Phi}} = \frac{qn_0}{\epsilon_0} \frac{N_i - N_e}{N_0} \cdot \frac{\Delta t^2 q}{m} \\
&= \underbrace{\frac{q^2 n_0}{m\epsilon_0}}_{=\omega_p^2} \Delta t^2 \frac{N_i - N_e}{N_0} \\
&= \underbrace{\widetilde{\Delta t}^2}_{=\Delta t^2} \cdot \frac{N_i - N_e}{\frac{N_{\lambda Db} \cdot \lambda_D^2 \cdot \Delta x}{\lambda_D^3}} \\
&\Leftrightarrow \widetilde{\Delta\Phi} = \frac{\widetilde{\Delta t}^2 \cdot (N_i - N_e)}{N_{\lambda Db} \cdot \widetilde{\Delta x}} \\
&\Downarrow \Rightarrow \tilde{q} = \frac{\widetilde{\Delta t}^2}{N_{\lambda Db} \cdot \Delta x}
\end{aligned}$$

$$\widetilde{\Delta\Phi} = \tilde{q}(N_i - N_e)$$

## A.2 Table of modelled collisions

Collision	Reference
e-e, e-ion, ion-ion Coulomb	[44]
e-Ar Elastic Collision	[73]
Ar <sup>+</sup> - Ar Elastic Collisions	[73]
Ionization: $e + \text{Ar} \rightarrow \text{Ar}^+ + 2e$	[73]
Charge-exchange: $\text{Ar} + \text{Ar}^+ \rightarrow \text{Ar}^+ + \text{Ar}$	[73]
Excitation: $e + \text{Ar} \rightarrow \text{Ar}^* + e$	[73]

Table A.2: Table of collisions included in the current MCC model and their sources (for the cross-sections), respectively.



# Bibliography

- [1] C. K. GOERTZ. Dusty plasmas in the solar system. *Reviews of Geophysics*, 27 271–292 **1989**
- [2] P. K. SHUKLA and A. A. MAMUN. *Introduction to dusty plasma physics*. Institute of Physics Publishing **2002**
- [3] R. J. BUSS and S. V. BABU. Synthesis of silicon nitride particles in pulsed radio frequency plasmas. In *Dusty plasmas—'95 workshop on generation, transport, and removal of particles in plasmas*, vol. 14, pp. 577–581. AVS **1996**. doi:10.1116/1.580148
- [4] P. R. I CABARROCAS, N. LAYADI, M. KUNST *et al.* Optical and transport properties of amorphous and microcrystalline silicon films prepared by excimer laser assisted rf glow-discharge deposition. *Journal of Vacuum Science and Technology A: Vacuum, Surfaces, and Films*, 16(2) 436–443 **1998**. doi:10.1116/1.581041
- [5] G. S. SELWYN. Particulate contamination control in plasma processing: Building-in reliability for semiconductor fabrication. *International Integrated Reliability Workshop Final Report*, Lake Tahoe, California, USA, pp. 122–129 **1996**
- [6] J. WINTER. Dust: A new challenge in nuclear fusion research? *Physics of Plasmas*, 7 3862–3866 **2000**
- [7] J. WINTER and G. GEBAUER. Dust in magnetic confinement fusion devices and its impact on plasma operation. *Journal of Nuclear Materials*, 266-269 228–233 **1999**. doi:10.1016/S0022-3115(98)00526-1
- [8] J. SHARPE, V. ROHDE, T. A.-U. E. TEAM *et al.* Characterization of dust collected from asdex-upgrade and lhd. *Journal of Nuclear Materials*, 313-316 455–459 **2003**. doi:10.1016/S0022-3115(02)01360-0. *Plasma-Surface Interactions in Controlled Fusion Devices* 15

- [9] M. RUBEL, M. CECCONELLO, J. MALMBERG *et al.* Dust particles in controlled fusion devices: morphology, observations in the plasma and influence on the plasma performance. *Nuclear Fusion*, 41(8) 1087 **2001**
- [10] K. NARIHARA, K. TOI, Y. HAMADA *et al.* Observation of dust particles by a laser scattering method in the jippt-iiu tokamak. *Nuclear Fusion*, 37(8) 1177 **1997**
- [11] W. L. SLATTERY, G. D. DOOLEN and H. E. DEWITT. Improved equation of state for the classical one-component plasma. *Phys Rev A*, 21(6) 2087–2095 **1980**. doi:10.1103/PhysRevA.21.2087
- [12] S. HAMAGUCHI. Strongly coupled yukawa plasmas – models for dusty plasmas and colloidal suspensions. *Plasmas & Ions*, 2(2) 57–68 **1999**. doi:10.1016/S1288-3255(00)87687-X
- [13] A. MELZER, A. HOMANN and A. PIEL. Experimental investigation of the melting transition of the plasma crystal. *Phys Rev E*, 53 2757–2766 **1996**
- [14] O. ARP, D. BLOCK, A. PIEL *et al.* Dust coulomb balls: three-dimensional plasma crystals. *Phys Rev Lett*, 93 165004 **2004**
- [15] O. ARP, D. BLOCK, M. KLINDWORTH *et al.* Confinement of coulomb balls. *Phys Plasmas*, 12 122102 **2005**
- [16] A. PIEL and A. MELZER. Dynamical processes in complex plasmas (review article). *Plasma Phys Control Fusion*, 44 R1–R26 **2002**
- [17] C. ZAFIU. Dynamic balance of forces in dusty (complex) plasmas. PhD submitted to Christian-Albrechts-Universität Kiel **2002**
- [18] D. BOHM. The characteristics of electrical discharges in magnetic fields. ed A Guthrie and RK Wakerling, New York: McGraw-Hill **1949**
- [19] H. IKEZI. Coulomb solid of small particles in plasmas. *Physics of Fluids*, 29(6) 1764–1766 **1986**. doi:10.1063/1.865653
- [20] S. ICHIMARU. Strongly coupled plasmas: high-density classical plasmas and degenerate electron liquids. *Rev Mod Phys*, 54(4) 1017–1059 **1982**. doi:10.1103/RevModPhys.54.1017
- [21] H. THOMAS, G. E. MORFILL, V. DEMMEL *et al.* Plasma crystal: Coulomb crystallization in a dusty plasma. *Phys Rev Lett*, 73 652–655 **1994**

- [22] J. H. CHU and I. LIN. Direct observation of coulomb crystals and liquids in strongly coupled rf dusty plasmas. *Phys Rev Lett*, 72(25) 4009–4012 **1994**. doi:10.1103/PhysRevLett.72.4009
- [23] Y. HAYASHI and K. TACHIBANA. Observation of coulomb-crystal formation from carbon particles grown in a methane plasma. *Japanese Journal of Applied Physics*, 33(Part 2, No. 6A) L804–L806 **1994**. doi:10.1143/JJAP.33.L804
- [24] A. MELZER, T. TROTTENBERG and A. PIEL. Experimental determination of the charge on dust particles forming coulomb lattices. *Physics Letters A*, 191(3-4) 301–308 **1994**. doi:10.1016/0375-9601(94)90144-9
- [25] T. TROTTENBERG, A. MELZER and A. PIEL. Measurement of the electric charge on particulates forming coulomb crystals in the sheath of a radiofrequency plasma. *Plasma Sources Science and Technology*, 4(3) 450 **1995**
- [26] O. ARP, D. BLOCK, M. BONITZ *et al.* 3d coulomb balls: experiment and simulation. *Journal of Physics: Conference Series*, 11(1) 234 **2005**
- [27] A. V. IVLEV, A. G. KHRAPAK, S. A. KHRAPAK *et al.* Rodlike particles in gas discharge plasmas: Theoretical model. *Phys Rev E*, 68(2) 026403 **2003**. doi:10.1103/PhysRevE.68.026403
- [28] S. N. FEJER and D. J. WALES. Helix self-assembly from anisotropic molecules. *Phys Rev Lett*, 99(8) 086106 **2007**. doi:10.1103/PhysRevLett.99.086106
- [29] K. MATYASH and R. SCHNEIDER. Pic-mcc modeling of a capacitive rf discharge. *Contributions to Plasma Physics*, 44(7-8) 589–593 **2004**
- [30] K. MATYASH. Kinetic modeling of multi-component edge plasmas. PhD submitted to Ernst-Moritz-Arndt-Universität Greifswald Available at: <http://wwwippmpgde/~knm> **2003**
- [31] K. MATYASH, R. SCHNEIDER, F. TACCOGNA *et al.* Finite size effect of dust charging in the magnetized edge plasma. *J Nuclear Materials*, 363-365 458–461 **2007**
- [32] P. DEBYE and E. HÜCKEL. The theory of electrolytes. i. lowering of freezing point and related phenomenon. *Physikalische Zeitschrift*, 24 185–206 **1923**
- [33] M. A. LIEBERMAN and A. J. LICHTENBERG. *Principles of Plasma Discharges and Materials Processing*. Wiley-Interscience, 2nd edn. **2005**

- [34] D. TSKHAKAYA, K. MATYASH, R. SCHNEIDER *et al.* The particle in cell method. *Contrib Plasma Phys*, 47(8-9) 563–594 **2007**
- [35] K. MATYASH, R. SCHNEIDER, F. TACCOGNA *et al.* Particle in cell simulation of low temperature laboratory plasmas. *Contrib Plasma Phys*, 47(8-9) 595–634 **2007**
- [36] R. HOCKNEY and J. EASTWOOD. Computer simulation using particles. McGraw-Hill, New York **1981**
- [37] C. K. BIRDSALL and A. B. LANGDON. Plasma physics via computer simulation. McGraw-Hill, New York **1985**
- [38] N. A. GERSHENFELD. The nature of mathematical modelling. Cambridge University Press **1999**
- [39] J. P. BORIS and R. A. SHANNY, eds. Proceedings of the Fourth Conference on Numerical Simulation of Plasmas. Naval Research Laboratory **1971**
- [40] K. MATYASH and R. SCHNEIDER. Finite size effects on charging in dusty plasmas. *J Plasma Phys*, 72(6) 809–812 **2006**
- [41] J. W. DEMMEL, S. C. EISENSTAT, J. R. GILBERT *et al.* A supernodal approach to sparse partial pivoting. *SIAM J Matrix Analysis and Applications*, 20(3) 720–755 **1999**
- [42] V. VAHEDI, G. DIPESO, C. K. BIRDSALL *et al.* Capacitive rf discharges modelled by particle-in-cell monte carlo simulation. i. analysis of numerical techniques. *Plasma Sources Science and Technology*, 2(4) 261 **1993**
- [43] V. VAHEDI and M. SURENDRA. A monte carlo collision model for the particle-in-cell method: applications to argon and oxygen discharges. *Computer Physics Communications*, 87(1-2) 179–198 **1995**
- [44] T. TAKIZUKA and H. ABE. A binary collision model for plasma simulation with a particle code. *J Comp Phys*, 25 205–219 **1977**
- [45] R. IKKURTHI. Kinetic simulations of dusty plasmas. PhD submitted to Ernst-Moritz-Arndt-Universität Greifswald **2009**
- [46] V. GODYAK and R.B.PIEJAK. Abnormally low electron energy and heating-mode transition in a low-pressure argon rf discharge at 13.56 mhz. *Phys Rev Lett*, 65 996–999 **1990**
- [47] J. E. ALLEN. Probe theory: The orbital motion approach. *Physica Scripta*, 45 497–503 **1992**

- [48] H. M. MOTT-SMITH and I. LANGMUIR. The theory of collectors in gaseous discharges. *Phys Rev*, 28(4) 727–763 **1926**. doi:10.1103/PhysRev.28.727
- [49] E. C. WHIPPLE, T. G. NORTHROP and D. MENDIS. The electrostatics of a dusty plasma. *Journal of Geophysical Research*, 90(A8) 7405–7413 **1985**
- [50] A. MELZER. Introduction to colloidal (dusty) plasmas. Lecture Notes at Ernst-Moritz-Arndt-Universität Greifswald **2005**
- [51] S. NUNOMURA, T. MISAWA, N. OHNO *et al.* Instability of dust particles in a coulomb crystal due to delayed charging. *Phys Rev Lett*, 83(10) 1970–1973 **1999**. doi:10.1103/PhysRevLett.83.1970
- [52] M. LAMPE, V. GAVRISHCHAKA, G. GANGULI *et al.* Effect of trapped ions on shielding of a charged spherical object in a plasma. *Phys Rev Lett*, 86(23) 5278–5281 **2001**. doi:10.1103/PhysRevLett.86.5278
- [53] M. LAMPE, R. GOSWAMI, Z. STERNOVSKY *et al.* Trapped ion effect on shielding, current flow, and charging of a small object in a plasma. *Physics of Plasmas*, 10(5) 1500–1513 **2003**. doi:10.1063/1.1562163
- [54] S. A. KHRAPAK, G. E. MORFILL, A. G. KHRAPAK *et al.* Charging properties of a dust grain in collisional plasmas. *Physics of Plasmas*, 13(5) 052114–+ **2006**. doi:10.1063/1.2201538
- [55] E. C. WHIPPLE. Potentials of surfaces in space. *Reports on Progress in Physics*, 44(11) 1197 **1981**
- [56] F. X. BRONOLD, H. FEHSKE, H. KERSTEN *et al.* Surface states and the charge of a dust particle in a plasma. *Phys Rev Lett*, 101(17) 175002 **2008**. doi:10.1103/PhysRevLett.101.175002
- [57] A. MELZER and S. HÜBNER. Dust influence on the atomic emission in dusty argon and helium discharges. unpublished **2010**
- [58] C. CUI and J. GOREE. Fluctuations of the charge on a dust grain in a plasma. *IEEE Trans on Plasma Science*, 22 151–158 **1994**
- [59] T. MATSOUKAS and M. RUSSELL. Particle charging in low-pressure plasmas. *Journal of Applied Physics*, 77(9) 4285–4292 **1995**. doi:10.1063/1.359451
- [60] T. MATSOUKAS, M. RUSSELL and M. SMITH. Stochastic charge fluctuations in dusty plasmas. In *Dusty plasmas—'95 workshop on generation, transport, and removal of particles in plasmas*, vol. 14, pp. 624–630. AVS **1996**. doi:10.1116/1.580156

- [61] M. A. FURMAN and M. T. F. PIVI. Probabilistic model for the simulation of secondary electron emission. *Phys Rev ST Accel Beams*, 5(12) 124404 **2002**. doi:10.1103/PhysRevSTAB.5.124404
- [62] I. H. HUTCHINSON. *Principles of Plasma Diagnostics*. Cambridge University Press **2002**
- [63] G. D. HOBBS and J. A. WESSON. Heat flow through a langmuir sheath in the presence of electron emission. *Plasma Physics*, 9(1) 85 **1967**
- [64] A. H. SATO and M. A. LIEBERMAN. Electron-beam probe measurements of electric fields in rf discharges. *Journal of Applied Physics*, 68(12) 6117–6124 **1990**. doi:10.1063/1.346899
- [65] J. SCHULZE, Z. DONKÓ, B. G. HEIL *et al.* Electric field reversals in the sheath region of capacitively coupled radio frequency discharges at different pressures. *Journal of Physics D: Applied Physics*, 41(10) 105214 **2008**
- [66] K. DITTMANN. Detailed investigations of the sheath dynamics and elementary processes in capacitively coupled rf plasmas. PhD submitted to Ernst-Moritz-Arndt-Universität Greifswald **2009**
- [67] Á. YANGUAS-GIL, J. COTRINO and L. L. ALVES. An update of argon inelastic cross sections for plasma discharges. *Journal of Physics D: Applied Physics*, 38(10) 1588 **2005**
- [68] J. E. CHILTON, J. B. BOFFARD, R. S. SCHAPPE *et al.* Measurement of electron-impact excitation into the  $3p54p$  levels of argon using fourier-transform spectroscopy. *Phys Rev A*, 57(1) 267–277 **1998**. doi:10.1103/PhysRevA.57.267
- [69] C. C. LIN. Measurements of Electron-Impact Excitation Cross Sections out of the Ground and Metastable Levels of Rare Gases with Applications to Low-Temperature Plasmas. *Contributions to Plasma Physics*, 44 405–412 **2004**. doi:10.1002/ctpp.200410059
- [70] J. B. BOFFARD, G. A. PIECH, M. F. GEHRKE *et al.* Measurement of electron-impact excitation cross sections out of metastable levels of argon and comparison with ground-state excitation. *Phys Rev A*, 59(4) 2749–2763 **1999**. doi:10.1103/PhysRevA.59.2749
- [71] E. B. TOMME, D. A. LAW, B. M. ANNARATONE *et al.* Parabolic plasma sheath potentials and their implications for the charge on levitated dust particles. *Phys Rev Lett*, 85(12) 2518–2521 **2000**. doi:10.1103/PhysRevLett.85.2518

- [72] T. NITTER. Levitation of dust in rf and dc glow discharges. *Plasma Sources Science and Technology*, 5(1) 93 **1996**
- [73] A. V. PHELPS. Jila data base. (unpublished) **2008**



# Acknowledgements

I am indebted to all friends and colleagues at the office and elsewhere. Firstly, I would like to thank my advisor, Prof. Dr. Ralf Schneider for his guidance and solid mentoring throughout the duration of this thesis.

I am deeply grateful to Konstantin for letting me experiment on his code and the helpful answers.

The same gratitude belongs to Ramana. At the beginning of my work your patience to my “stupid” questions was recognized.

I want to thank my teammates for their help when I encountered severe and sometimes insane (computer) problems and for the interesting, though often not work related discussions about life, its oddities and everything. Thank you Abha, Gunnar, Robert and Sascha. A big extra thank belongs to Gunnar for the barbell simulation.

Furthermore, I want to thank Prof. André Melzer for the fruitful collaboration and discussions.

The encouragement from my family and friends has been very important to me. I especially thank Liane, Timo, Tobi and Henry for their help and distraction. Last but not least, I am much obliged to my parents for their life-long support and trust.

Ich versichere, dass ich die vorliegende Arbeit selbständig verfasst und keine anderen Hilfsmittel als die angegebenen verwendet habe. Die Stellen, die anderen Werken dem Wortlaut oder dem Sinne nach entnommen sind, habe ich in jedem Falle durch Angaben der Quelle, auch der Sekundärliteratur, als Entlehnung kenntlich gemacht.

Greifswald, den 19.08.2010